
University of Crete

Department of Physics

PhD Thesis

by Georgios Miltiadis Maragkakis

# Polarization-resolved second and third harmonic generation in 2D materials

Supervisor: Dr. Emmanuel Stratakis

Heraklion, Crete

July, 2024


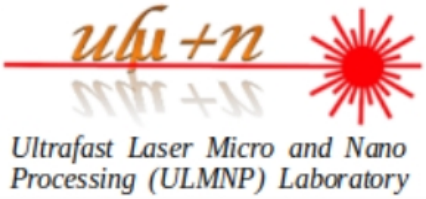

A dissertation presented for the degree of Doctor of Philosophy

Seven-member committee:

Dr. Emmanuel Stratakis
Prof. George Kioseoglou
Assoc. Prof. Konstantinos Makris

Assoc. Prof. Iannis Kominis
Assoc. Prof. George Kopidakis
Assoc. Prof. Liverios Lymperakis
Prof. Nikos Pelekanos

# Abbreviations

2D: two-dimensional

AC: armchair crystallographic direction

AR: anisotropy ratio

CVD: chemical vapor deposition

LPE: liquid phase exfoliation

MXs: group IV monochalcogenides, also known as group IV-VI metal monochalcogenides, with M = Sn, Ge and X = S, Se

P-SHG: polarization-resolved second harmonic generation

P-THG: polarization-resolved third harmonic generation

SHG: second harmonic generation

SnS: tin(II) sulfide

THG: third harmonic generation

TMDs: transition metal dichalcogenides, such as $MoS_2$, $WS_2$, $MoSe_2$ and $WSe_2$

ZZ: zigzag crystallographic direction

# Table of contents

# Abstract

Two-dimensional (2D) materials have been established as new class of materials with characteristics that make them a highly attractive scientific field, for both fundamental and technological studies. Furthermore, nonlinear optical imaging has been demonstrated as a powerful tool for characterizing 2D materials.

In this PhD thesis, second and third harmonic generation (SHG, THG) produced by 2D materials, when they interact with laser field, are explored. By employing laser-scanning using galvanometric mirrors, spatially resolved SHG or THG intensities, forming images, are recorded, while rotating the linear polarization of the excitation laser field, performing polarization-resolved SHG or THG (P-SHG, P-THG) microscopy imaging. The experimental data are then fitted with equations based on suitable nonlinear optics models. The demonstrated methods are all-optical, large-area, minimally-invasive and rapid.

In the first work (Chapter 2), P-SHG imaging in an atomically thin $WS_2$ crystal is performed, which belongs to the transition metal dichalcogenides (TMDs). Information on the crystallographic direction distribution is revealed, and the superiority of a P-SHG analysis over intensity-only SHG measurements is experimentally demonstrated.

In the second work (Chapter 3), a nonlinear optical imaging technique is presented, based on SHG microscopy and a SHG interference model, to map in a $WS_2/MoS_2$ 2D TMD heterostructure the twist angle, i.e., the relative orientation between the constituent monolayers.

In the third work (Chapter 4), the P-SHG properties of ultrathin tin(II) sulfide (SnS) crystals are investigated. SnS exhibits in-plane anisotropic response, offering an additional degree of freedom in manipulating its properties. The armchair/zigzag crystallographic directions of several 2D SnS crystals belonging in the same field of view are calculated, as well as the relative magnitudes of the tensor components of the second-order nonlinear optical susceptibility.

In the fourth work (Chapter 5), it is shown that the THG signal produced by ultrathin SnS is in-plane anisotropic, with respect to the incident linear polarization of the laser field. The relative

magnitudes of the tensor components of the third-order nonlinear optical susceptibility are determined.

# Περίληψη (Abstract)

Τα δισδιάστατα (2D) υλικά έχουν εδραιωθεί ως μία νέα κατηγορία υλικών με χαρακτηριστικά που τα καθιστούν ένα πολύ ενδιαφέρον επιστημονικό πεδίο, τόσο για θεμελιώδεις όσο και για τεχνολογικές μελέτες. Επιπροσθέτως, η μη γραμμική οπτική απεικόνιση έχει παρουσιαστεί ως ένα ισχυρό εργαλείο για τον χαρακτηρισμό των 2D υλικών.

Στην παρούσα διδακτορική διατριβή, μελετάται η γέννηση δεύτερης και τρίτης αρμονικής (second and third harmonic generation - SHG, THG) που παράγεται από 2D υλικά, όταν αλληλεπιδρούν με το πεδίο λέιζερ. Χρησιμοποιώντας σάρωση λέιζερ μέσω γαλβανομετρικών καθρεπτών, καταγράφονται χωρικά διακριτές εντάσεις SHG ή THG, που σχηματίζουν εικόνες, καθώς περιστρέφεται η γραμμική πόλωση τού πεδίου τού λέιζερ, εκτελώντας απεικόνιση μικροσκοπίας SHG ή THG με εξάρτηση από την πόλωση (polarization-resolved SHG or THG - P-SHG, P-THG). Έπειτα, τα πειραματικά δεδομένα περιγράφονται με εξισώσεις βασισμένες σε κατάλληλα μοντέλα μη γραμμικής οπτικής. Οι μέθοδοι που παρουσιάζονται είναι εξολοκλήρου οπτικές, καλύπτουν μεγάλη περιοχή, είναι ελάχιστα επεμβατικές και γρήγορες.

Στην πρώτη εργασία (Κεφάλαιο 2), γίνεται P-SHG απεικόνιση σε ένα ατομικά λεπτό κρύσταλλο δισουλφιδίου τού βολφραμίου ($WS_2$), ο οποίος ανήκει στα διχαλκογενή μέταλλα μετάπτωσης (transition metal dichalcogenides - TMDs). Εξάγεται πληροφορία για την κατανομή τής κρυσταλλικής διεύθυνσης, και παρουσιάζεται πειραματικά η ανωτερότητα της P-SHG ανάλυσης συγκριτικά με μετρήσεις μόνο έντασης SHG.

Στη δεύτερη εργασία (Κεφάλαιο 3), παρουσιάζεται μία τεχνική μη γραμμικής οπτικής απεικόνισης, βασισμένη σε μικροσκοπία SHG και ένα μοντέλο συμβολής SHG, προκειμένου να χαρτογραφηθεί σε μία 2D TMD ετεροδομή $WS_2$/δισουλφιδίου του μολυβδαινίου ($MoS_2$) η σχετική γωνία (twist angle), δηλαδή η σχετική διεύθυνση μεταξύ των μονοστρωμάτων (monolayers) που συνθέτουν την ετεροδομή.

Στην τρίτη εργασία (Κεφάλαιο 4), μελετώνται οι P-SHG ιδιότητες πολύ λεπτών κρυστάλλων θειούχου κασσίτερου (tin(II) sulfide - SnS). Το SnS χαρακτηρίζεται από “εντός-του-επιπέδου” (in-plane) ανισοτροπική απόκριση, προσφέροντας έναν επιπλέον βαθμό ελευθερίας στην αξιοποίηση των ιδιοτήτων του. Υπολογίζονται οι “armchair”/“zigzag” κρυσταλλογραφικές διευθύνσεις

διάφορων 2D SnS κρυστάλλων που ανήκουν στο ίδιο οπτικό πεδίο, καθώς και τα σχετικά μεγέθη των στοιχείων τού τένσορα τής δεύτερης-τάξης μη γραμμικής οπτικής επιδεκτικότητας.

Στην τέταρτη εργασία (Κεφάλαιο 5), δείχνεται ότι το σήμα THG που παράγεται από πολύ λεπτό SnS είναι in-plane ανισοτροπικό, σε σχέση με την προσπίπτουσα γραμμική πόλωση τού πεδίου τού λέιζερ. Υπολογίζονται τα σχετικά μεγέθη των στοιχείων τού τένσορα τής τρίτης-τάξης μη γραμμικής οπτικής επιδεκτικότητας.

# Ευχαριστίες (Acknowledgments)

Ευχαριστώ τον Δρ. Μανόλη Στρατάκη που επέβλεψε τη διδακτορική διατριβή μου, για την καθοδήγησή του, και που ήταν πάντα διαθέσιμος για ό,τι χρειάστηκα.

Ευχαριστώ τον Δρ. Σωτήρη Ψιλοδημητρακόπουλο, που ουσιαστικά συν-επέβλεψε τη διατριβή μου. Η καθοδήγησή του και η πειραματική διάταξη που είχε αναπτύξει, έπαιξαν σημαντικό ρόλο στα αποτελέσματα που παρουσιάζονται.

Ευχαριστώ τον Δρ. Λεωνίδα Μουχλιάδη, που ουσιαστικά συν-επέβλεψε τη διατριβή μου. Η καθοδήγησή του και το θεωρητικό μοντέλο που είχε αναπτύξει, έπαιξαν σημαντικό ρόλο στα αποτελέσματα που παρουσιάζονται.

Ευχαριστώ τον Καθ. Γιώργο Κιοσέογλου, μέλος της τριμελούς επιτροπής, που συν-επέβλεψε τη διατριβή μου, για την καθοδήγησή του, και που ήταν πάντα διαθέσιμος.

Ευχαριστώ τον Dr. Abdus Salam Sarkar για την εποικοδομητική συνεργασία. Η απόφασή μου να εστιάσω τη μελέτη μου στις μη γραμμικές οπτικές ιδιότητες των δισδιάστατων υλικών που δημιούργησε και χαρακτήρισε, επηρέασε την κατεύθυνση τής διατριβής.

Ευχαριστώ τον Ανδρέα Λεμονή για τη συνεχή τεχνική υποστήριξη στην πειραματική διάταξη.

Ευχαριστώ τον Αναπλ. Καθ. Κωνσταντίνο Μακρή, που δέχθηκε να είναι στην τριμελή επιτροπή.

Ευχαριστώ τα μέλη της επταμελούς επιτροπής, που δέχθηκαν να αξιολογήσουν την διατριβή μου, και συγκεκριμένα, τον Δρ. Μανόλη Στρατάκη, τον Καθ. Γιώργο Κιοσέογλου, τον Αναπλ. Καθ. Κωνσταντίνο Μακρή, τον Αναπλ. Καθ. Ιωάννη Κομίνη, τον Αναπλ. Καθ. Γιώργο Κοπιδάκη, τον Αναπλ. Καθ. Λιβέριο Λυμπεράκη, και τον Καθ. Νίκο Πελεκάνο.

Ευχαριστώ τον Δρ. Γιώργο Κουρμουλάκη και τη Δρ. Ιωάννα Δεμερίδου για την εποικοδομητική συνεργασία, στα πλαίσια τής δημιουργίας και του χαρακτηρισμού δισδιάστατων υλικών, που μας προμήθευαν.

Ευχαριστώ τον Δρ. Διονύση Ξυδιά. Οι πορείες μας στο διδακτορικό ήταν παράλληλες, ενώ μοιραζόμασταν και την ίδια πειραματική διάταξη. Η αλληλοϋποστήριξή μας ήταν πολύτιμη. Η απώλειά του αφήνει ένα κενό που δεν αναπληρώνεται. Κατά μία έννοια, τουλάχιστον, ένας άνθρωπος φεύγει όταν ξεχνιέται.

Ευχαριστώ τη Μαίρη Κεφαλογιάννη για τη συνεισφορά της, ενώ μοιραζόμασταν την ίδια πειραματική διάταξη.

Ευχαριστώ όλα τα νυν και πρώην μέλη τής ερευνητικής ομάδας τού Δρ. Μανόλη Στρατάκη, που γνώρισα, για το όμορφο κλίμα εργασίας.

Ευχαριστώ τον Μιχάλη Μεταξά για τον σχεδιασμό δύο υποψήφιων εξώφυλλων ερευνητικών περιοδικών.

Ευχαριστώ όσους αναπτύσσουν και διατηρούν ελεύθερα προγράμματα, όπως τα Ubuntu, η Python, και το ImageJ, που χρησιμοποίησα κατά τη διάρκεια τής διατριβής.

Σε επικουρικό επίπεδο, ευχαριστώ όλους τους φοιτητές και τους διδάσκοντες με τους οποίους αλληλεπίδρασα, στα μαθήματα Εργαστήρια Laser και Μοντέρνας Οπτικής, και Προχωρημένο Εργαστήριο Φυσικής Ι.

Μιας κι εδώ κλείνει ο κύκλος σπουδών μου στο Τμήμα Φυσικής τού Πανεπιστημίου Κρήτης, ευχαριστώ καθηγητές των οποίων τις διαλέξεις παρακολούθησα.
Ευχαριστώ τον Καθ. Ανδρέα Ζέζα, επιβλέποντα στην προπτυχιακή και μεταπτυχιακή διπλωματική μου, για τον όμορφο τρόπο με τον οποίο με εισήγαγε στην έρευνα.
Ευχαριστώ τον Καθ. Ιωσήφ Παπαδάκη για τη χρήσιμη συμβουλή που μου είχε δώσει, ώστε να προετοιμαστώ για να συνεχίσω στο μεταπτυχιακό πρόγραμμα που είχα επιλέξει.

Σε συνδικαλιστικό επίπεδο, ευχαριστώ τα μέλη του ΣΕΕΕΗ (Σύλλογος Ερευνητών/Ερευνητριών και Εργαζομένων στην Έρευνα Ηρακλείου), που γνώρισα, για τις συλλογικές προσπάθειες για να βελτιώσουμε τις εργασιακές μας συνθήκες.

Σε εθελοντικό επίπεδο, ευχαριστώ τα μέλη τού ΚΕΘΕΑ (Κέντρο Θεραπείας Εξαρτημένων Ατόμων), που γνώρισα, κατά τη διάρκεια τού ενός χρόνου στον οποίο είχα τη χαρά να διδάξω μαθητές Β’ Λυκείου.

Σε προσωπικό επίπεδο, ευχαριστώ την οικογένειά μου για όλα. Ιδιαίτερα τους γονείς μου, Μανόλη και Στέλλα, καθώς και τις αδερφές μου, Εύη και Γιολάντα.

Σε προσωπικό επίπεδο, ευχαριστώ τους φίλους και τις φίλες μου, για την πολύτιμη φιλία τους.

Η χρηματοδότηση τής παρούσας έρευνας, για την οποία και ευχαριστώ, προήλθε από:
- Ανταποδοτικές υποτροφίες, στα πλαίσια ευρωπαϊκών και ελληνικών ερευνητικών προγραμμάτων (Επιστημονικός Υπεύθυνος: Δρ. Μανόλης Στρατάκης, Συν-συγγραφείς: Μέλη της ερευνητικής ομάδας του Δρ. Μανόλη Στρατάκη).
- Το πρόγραμμα ΕΣΠΑ, για την ερευνητική πρόταση με τίτλο: “Έλεγχος της κρυσταλλικής ποιότητας δισδιάστατων υλικών και των ετεροδομών τους μέσω απεικόνισης των μη γραμμικών οπτικών τους ιδιοτήτων” (Επιστημονικός Υπεύθυνος: Καθ. Γιώργος Κιοσέογλου, Συν-συγγραφείς: Δρ. Σωτήρης Ψιλοδημητρακόπουλος, Δρ. Λεωνίδας Μουχλιάδης).
- Προσωπικές υποτροφίες από το ίδρυμα Σταύρος Νιάρχος, μέσω του προγράμματος ARCHERS, και από τον Ανεξάρτητο Διαχειριστή Μεταφοράς Ηλεκτρικής Ενέργειας (ΑΔΜΗΕ) Α.Ε..

Κατά τη διάρκεια αυτού του ταξιδιού απέκτησα δεσμούς με ανθρώπους, εμπειρίες και γνώσεις, που θα θυμάμαι.

Σας ευχαριστώ.

Γιώργος Μίλτος Μαραγκάκης

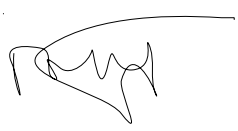

Ηράκλειο Κρήτης
Ιούλιος, 2024

# Publications in peer reviewed journals, related to this thesis

1. Maragkakis GM, Psilodimitrakopoulos S, Mouchliadis L, Paradisanos I, Lemonis A, Kioseoglou G, Stratakis E. **Imaging the crystal orientation of 2D transition metal dichalcogenides using polarization-resolved second-harmonic generation**. Opto-Electronic Advances 2 (11), 190026 (2019)

2. Psilodimitrakopoulos S, Mouchliadis L, Maragkakis GM, Kourmoulakis G, Lemonis A, Kioseoglou G, Stratakis E. **Real-time spatially resolved determination of twist angle in transition metal dichalcogenide heterobilayers**. 2D Materials 8 (1), 015015 (2020)

3. Mouchliadis L, Psilodimitrakopoulos S, Maragkakis GM, Demeridou I, Kourmoulakis G, Lemonis A, Kioseoglou G, Stratakis E. **Probing valley population imbalance in transition metal dichalcogenides via temperature-dependent second harmonic generation imaging**. npj 2D Materials and Applications 5 (1), 1-9 (2021)

4. Psilodimitrakopoulos S, Orekhov A, Mouchliadis L, Jannis D, Maragkakis GM, Kourmoulakis G, Gauquelin N, Kioseoglou G, Verbeeck J, Stratakis E. **Optical versus electron diffraction imaging of twist-angle in 2D transition metal dichalcogenide bilayers** npj 2D Materials and Applications 5 (1), 1-9 (2021)

5. Babonneau D, Camelio S, Abadias G, Christofilos D, Arvanitidis J, Psilodimitrakopoulos S, Maragkakis GM, Stratakis E, Kalfagiannis N, Patsalas P. **Self-Assembled Dichroic Plasmonic Nitride Nanostructures with Broken Centrosymmetry for Second-Harmonic Generation**. ACS Applied Nano Materials 4 (9), 8789-8800 (2021)

6. Maragkakis GM, Psilodimitrakopoulos S, Mouchliadis L, Sarkar AS, Lemonis A, Kioseoglou G, Stratakis E. **Nonlinear Optical Imaging of In-Plane Anisotropy in Two-Dimensional SnS**. Advanced Optical Materials 10 (10), 2102776 (2022) (Selected as inside front cover)

7. Sarkar AS, Konidakis I, Gagaoudakis E, Maragkakis GM, Psilodimitrakopoulos S, Katerinopoulou D, Sygellou L, Deligeorgis G, Binas V, Oikonomou IM, Komninou P, Kiriakidis G, Kioseoglou G, Stratakis E. **Liquid Phase Isolation of SnS Monolayers with Enhanced Optoelectronic Properties**. Advanced Science 2201842 (2022)

8. Kourmoulakis G, Psilodimitrakopoulos S, Maragkakis GM, Mouchliadis L, Michail A, Christodoulides JA, Tripathi M, Dalton AB, Parthenios J, Papagelis K, Stratakis E, Kioseoglou G. **Strain distribution in $WS_2$ monolayers detected through Polarization-resolved Second Harmonic Generation**. Accepted in Scientific Reports

9. Ilin S, Khmelevskaia D, Nikolaeva A, Maragkakis GM, Psilodimitrakopoulos S, Mouchliadis L, Talianov PM, Khubezhov S, Stratakis E, Zelenkov LE, Makarov SV. **Lead-free halide perovskite nanoparticles for up-conversion lasing and efficient second harmonic generation**. Accepted in Advanced Optical Materials

10. Maragkakis GM, Psilodimitrakopoulos S, Mouchliadis L, Sarkar AS, Lemonis A, Kioseoglou G, Stratakis E. **Anisotropic Third Harmonic Generation in Two-Dimensional Tin Sulfide**. Accepted in Advanced Optical Materials

## Conference presentations

1. Maragkakis GM, Psilodimitrakopoulos S, Mouchliadis L, Sarkar AS, Lemonis A, Kioseoglou G, Stratakis E. Second harmonic generation imaging in two-dimensional SnS probes in-plane anisotropy. **Oral presentation**. XXXV Panhellenic Conference on Solid State Physics & Materials Science. Virtual only conference due to pandemic. 09/2021.

2. Maragkakis GM, Psilodimitrakopoulos S, Mouchliadis L, Sarkar AS, Lemonis A, Kioseoglou G, Stratakis E. Nonlinear Optical Imaging of In-Plane Anisotropy in Two-Dimensional SnS. **Poster presentation**. XXXVI Panhellenic Conference on Solid State Physics & Materials Science. Heraklion, Crete. 09/2022.

3. Maragkakis GM, Psilodimitrakopoulos S, Mouchliadis L, Sarkar AS, Lemonis A, Kioseoglou G, Stratakis E. Anisotropic Third Harmonic Generation in Two-Dimensional SnS. **Poster presentation**. 2nd International Conference on Nanotechnologies and Bionanoscience (NanoBio). Heraklion, Crete. 09/2023.

# Structure of this thesis

- In the first chapter, a brief introduction on nonlinear optics in 2D materials is presented. Furthermore, the state of the art literature findings, on the publications presented in Chapters 2-5, are discussed; they are reproduced from the corresponding publications.

- In the second chapter, the following publication is presented:
  Maragkakis GM, Psilodimitrakopoulos S, Mouchliadis L, Paradisanos I, Lemonis A, Kioseoglou G, Stratakis E. **Imaging the crystal orientation of 2D transition metal dichalcogenides using polarization-resolved second-harmonic generation**. Opto-Electron. Adv. 2019, 2, 190026.

- In the third chapter, the following publication is presented:
  S. Psilodimitrakopoulos S, L. Mouchliadis L, G. M. Maragkakis GM, Kourmoulakis G, Lemonis A, Kioseoglou G, Stratakis E, **Real-time spatially resolved determination of twist angle in transition metal dichalcogenide heterobilayers**. 2D Mater. 2021, 8, 015015.

- In the fourth chapter, the following publication is presented:
  Maragkakis GM, Psilodimitrakopoulos S, Mouchliadis L, Sarkar AS, Lemonis A, Kioseoglou G and Stratakis E. **Nonlinear optical imaging of in-plane anisotropy in two-dimensional SnS**. Adv. Optical Mater., 2022, 10: 2270038.

- In the fifth chapter, the following publication is presented:
  Maragkakis GM, Psilodimitrakopoulos S, Mouchliadis L, Sarkar AS, Lemonis A, Kioseoglou G and Stratakis E. **Anisotropic third harmonic generation in two-dimensional tin sulfide**. Accepted in Advanced Optical Materials.
  Given that this work was under revision while this chapter was prepared, there are differences between the version presented here and the published one. The results and conclusions, however, are, of course, the same.

- In the sixth chapter, conclusions on the publications presented in chapters 2-5, are discussed; they are reproduced from the corresponding publications.

The references/bibliography are presented at the end of each section in Chapter 1, and at the end of each chapter in Chapters 2-6.

# Chapter 1 – Introduction & State of the art

## 1.1. Nonlinear optics

If we consider the response of the electrons in a material to the stimulus of the optical frequency electric field of the laser beam, the displacement of the electrons creates an induced polarization, i.e., a dipole moment per unit volume [1, p. 3].

In linear optics, the induced polarization P of a medium depends linearly on the electric field strength E, as [1, p. 2, 2, p. 1]:

$$P = \varepsilon_0 \chi^{(1)} E \quad (1)$$

where $\varepsilon_0$ is the permittivity of free space and $\chi^{(1)}$ is known as the linear susceptibility.

Nonlinear optical phenomena occur when the response of a material system to an applied optical field depends in a nonlinear manner on the strength of the applied optical field [2, p. 1]. In nonlinear optics, the optical response can often be described as a generalization of Eq. 1, by expressing the induced polarization as a power series in the field strength E, as [1, p. 4, 2, p. 2]:

$$P = \varepsilon_0 \left[ \chi^{(1)} E + \chi^{(2)} E^2 + \chi^{(3)} E^3 + ... \right] \quad (2)$$

The quantities $\chi^{(2)}$ and $\chi^{(3)}$ are known as the second- and third-order nonlinear optical susceptibilities, respectively [2, p. 2]. When P and E are treated as vectors, $\chi^{(i)}$ become tensors [2, p. 2].

A time-varying polarization can act as the source of new components of the electromagnetic field [2, p. 3]. For example, the wave equation in nonlinear optical media often has the form [2, p. 3]:

$$\nabla^2 E - \frac{n^2}{c^2} \frac{\partial^2 E}{\partial t^2} = \frac{1}{\varepsilon_0 c^2} \frac{\partial^2 P^{NL}}{\partial t^2} \quad (3)$$

where n is the usual linear refractive index and c is the speed of light in vacuum. We can interpret this expression as an inhomogeneous wave equation in which the polarization $P^{NL}$ associated with the nonlinear response acts as a source term for the electric field [2, p. 3].

## References

[1] G. New, *Introduction to Nonlinear Optics*, Cambridge University Press 2011

[2] R. W. Boyd, *Nonlinear Optics*, Academic Press, Elsevier 2020.

### 1.1.1 SHG & THG

Let us consider that a lightwave of the form [1, p. 668]:

$$E = E_0 \sin(\omega t) \qquad (4)$$

is incident on a nonlinear optical medium. By substituting Eq. 4 into Eq. 2, we obtain the following expression of the resulting electric polarization [1, p. 668]:

$$P = \varepsilon_0 \chi^{(1)} E_0 \sin(\omega t) + \varepsilon_0 \chi^{(2)} E_0^2 \sin^2(\omega t) + \varepsilon_0 \chi^{(3)} E_0^3 \sin^3(\omega t) + \ldots \qquad (5)$$

Then, by using the identities $\sin^2 a = \frac{1}{2}(1 - \cos 2\alpha)$ and $\sin^3 a = \frac{1}{4}(3 sina - \sin 3a)$, we have [1, p. 668]:

$$P = \varepsilon_0 \chi^{(1)} E_0 \sin(\omega t) + \frac{1}{2}\varepsilon_0 \chi^{(2)} E_0^2 (1 - \cos(2\omega t)) + \frac{1}{4}\varepsilon_0 \chi^{(3)} E_0^3 (3\sin(\omega t) - \sin(3\omega t)) + \ldots \qquad (6)$$

The term $\cos(2\omega t)$ in Eq. 6 corresponds to a variation in electric polarization at twice the frequency of the incident wave. The re-radiated light that arises from the driven oscillators also has a component at this same frequency, 2ω, and this process is SHG [1, p. 668], which is illustrated schematically in **Fig. 1.1.**

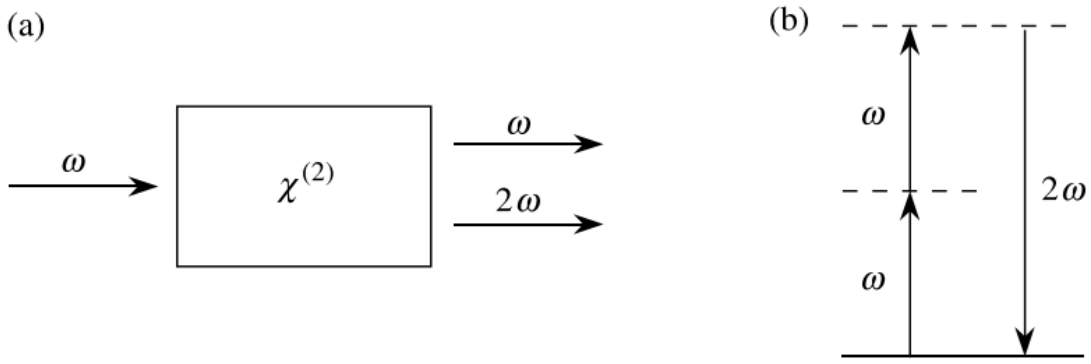


**Figure 1.1. a**) Geometry of SHG. **b**) Energy-level diagram describing SHG. Reproduced from Ref. 2, p. 5.

In this process, two photons of frequency ω are destroyed, and a photon of frequency 2ω is simultaneously created in a single quantum-mechanical process [2, p. 5]. The solid line in the **Fig. 1.1b** represents the atomic ground state, and the dashed lines represent virtual levels [2, p. 5].

SHG was experimentally observed for the first time in 1961, in crystalline quartz, by a team led by the American physicist Peter Franken at the University of Michigan [3].

Now let us introduce the concept of THG. The term $\sin(3\omega t)$ in Eq. 6 describes a response at frequency 3ω that is created by an applied field at frequency ω. This term leads to the process of THG [2, p. 10], which is illustrated in **Fig. 1.2.** According to the photon description of this process (**Fig. 1.2b**), three photons of frequency ω are destroyed and one photon of frequency 3ω is created in this process [2, p. 10].

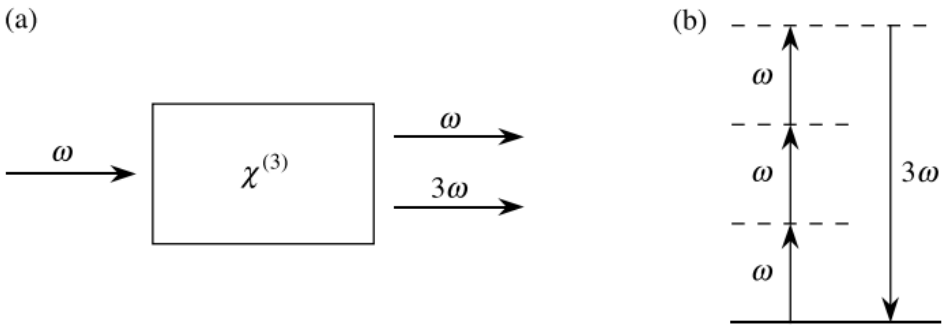


**Figure 1.2. a**) Geometry of THG. **b**) Energy-level diagram describing THG. Reproduced from Ref. 1, p. 10.

Importantly, second-order nonlinear optical interactions, such as SHG, can occur only in non-centrosymmetric crystals, that is, in crystals that do not display inversion symmetry [2, p. 2]. On the other hand, third-order nonlinear optical interactions, such as THG, can occur for both centrosymmetric and non-centrosymmetric media [2, p. 2].

## References

[1] E. Hecht, *Optics*, Pearson Education Limited 2017

[2] R. W. Boyd, *Nonlinear Optics*, Academic Press, Elsevier 2020.

[3] P. A. Franken, A. E. Hill, C. W. Peters, G. Weinreich, *Phys. Rev. Lett.*, **1961**, 7, 118.

## 1.2. Nonlinear optical properties of 2D materials

### 1.2.1 2D materials

Graphene is a single sheet of carbon atoms, with a thickness of 0.34 nm, arranged into a hexagonal structure [1, p. 1]. It was discovered and characterized in 2004, by Andre Konstantin Geim and Konstantin Sergeevich Novoselov, and co-workers, at the University of Manchester, UK [2]. For their work on graphene, the two Soviet-born physicists were awarded the 2010 Nobel Prize in Physics [3].

The successful isolation of graphene, which is a semimetal, was realized by mechanical exfoliation (repeated peeling), also known as the scotch tape technique [2-4]. This achievement motivated the study of numerous others 2D materials, namely atomically-thick, layered materials with weak van der Waals-like coupling between layers [4]. For example, in 2010, it was reported that when the semiconductor TMD $MoS_2$ crystal is thinned to monolayer, a strong photoluminescence emerges, indicating an indirect to direct bandgap transition [5, 6]. Recently, in 2017, the stability of more than 600 potential 2D materials, was predicted [7].

In this dissertation, we have focused our study one two families of 2D materials, namely TMDs, and MXs. Their properties are discussed in the corresponding chapters, namely 1.2.2, 1.5, 1.6, 1.7, 2 and 3 for TMDs, and 1.8, 1.9, 4 and 5 for MXs.

## References

[1] M. Dragoman, D. Dragoman, *2D Nanoelectronics*, Springer 2017.

[2] K. S. Novoselov, A. K. Geim, S. V. Morozov, D. Jiang, Y. Zhang, S. V. Dubonos, I. V. Grigorieva, A. A. Firsov, *Science* **2004**, 306, 666–669.

[3] A. K. Geim, *Rev Mod Phys* **2011**, 83:851–862.

[4] K. S. Novoselov, D. Jiang, F. Schedin, T. J. Booth, V. V. Khotkevich, S. V. Morozov, and A. K. Geim, *Proc. Natl. Acad. Sci. U.S.A.* **2005** 102, 10 451.

[5] A. Splendiani, L. Sun, Y. Zhang, T. Li, J. Kim, C.-Y. Chim, G. Galli, F. Wang, *Nano Lett.* **2010**, 10, 1271.

[6] K. F. Mak, C. Lee, J. Hone, J. Shan, T. F. Heinz, *Phys. Rev. Lett.* **2010**, 105, 136805.

[7] M. Ashton, J. Paul, S. B. Sinnott, R. G. Hennig, *Phys. Rev. Lett.* **2017**, 118, 106101.

### 1.2.2 SHG & THG in 2D materials

Recently, there has been a growing interest in the nonlinear optical properties of 2D materials, given that they provide a platform for both fundamental studies and technological applications. For instance, **Fig. 1.3.** shows the number of published research documents per year, on the field of "second harmonic generation 2D materials", revealing an increasing trend.

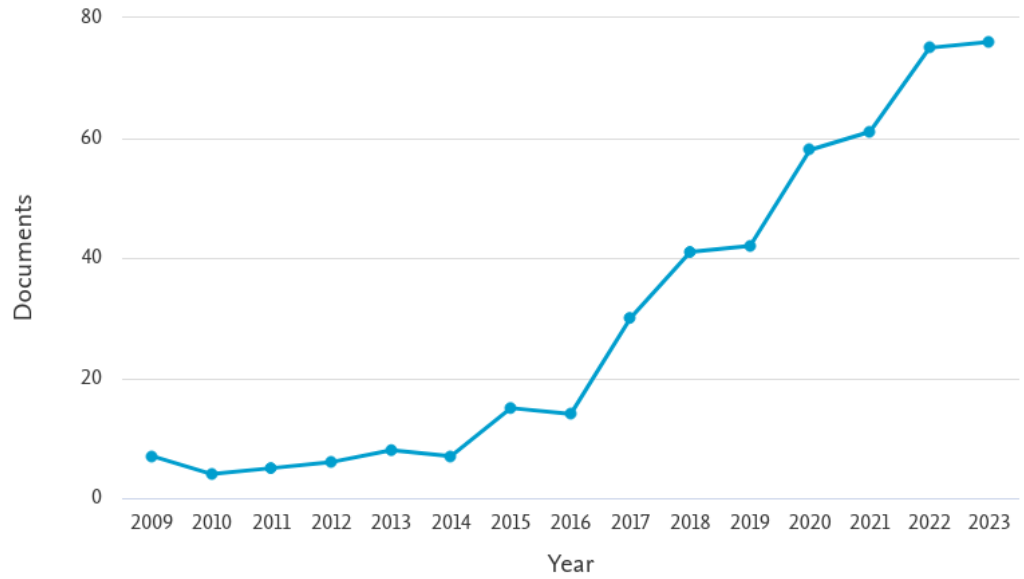


**Figure 1.3.** Number of published research documents per year, on the field of "second harmonic generation 2D materials". Source: Scopus, Elsevier. Search within: Article title, Abstract, Keywords.

Due to the centrosymmetric crystal structure of graphene, the second-order nonlinear optical effects, such as SHG, are, in principle, not allowed in graphene [1]. However, SHG signal has been observed in monolayer graphene by symmetry breaking [1]. 2H-phase TMDs with even number of layers are also centrosymmetric, and do not produce SHG (**Fig. 1.4**) [2]. On the other hand, 3R-phase TMDs, as well as odd-number-layer 2H-phase TMDs have no inversion symmetry (are non-centrosymmetric), allowing SHG, under intense optical pump (**Fig. 1.4**) [2]. SHG was first reported in 2013, in $MoS_2$ [3-5], and $WS_2$ and $WSe_2$ [6] crystals.

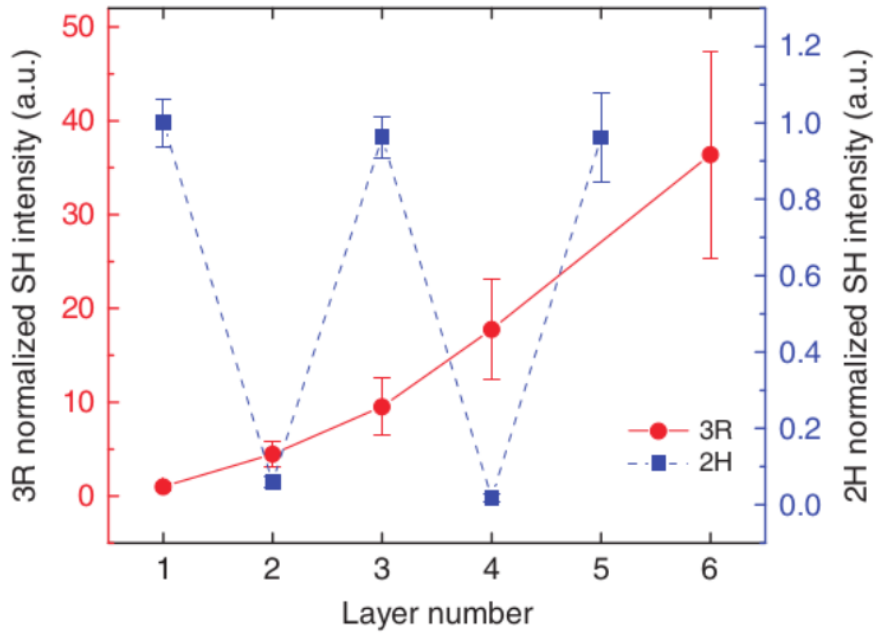


**Figure 1.4.** SHG intensity of 3R- and 2H-$MoS_2$ normalized to the respective single-layer intensity at a SHG/pump energy of 1.81 eV/0.905 eV (685/1370 nm). The dependence of the SH intensity is roughly squared with relation to the layer number in the 3R crystal, while it oscillates with layer number in the 2H crystal. Reproduced from Ref. 2.

Importantly, the intensities of the polarization components of SHG have been found to depend on the crystal orientation. Therefore, SHG can be utilized to probe the crystallographic orientation of 2D materials [1, 3-5, 7].

In addition, nonlinear optical susceptibility is typically obtained by dividing the sheet susceptibility with the thickness of the monolayer, yielding an effective bulk-like nonlinear optical susceptibility [1, 8]. An example for such a calculation for the effective bulk-like second- and third-order susceptibility of TMDs is presented in **Fig. 1.5**. In that work four different TMD flakes are placed in close proximity to each other on a common substrate, allowing their nonlinear optical properties to be probed from a single measurement [8].

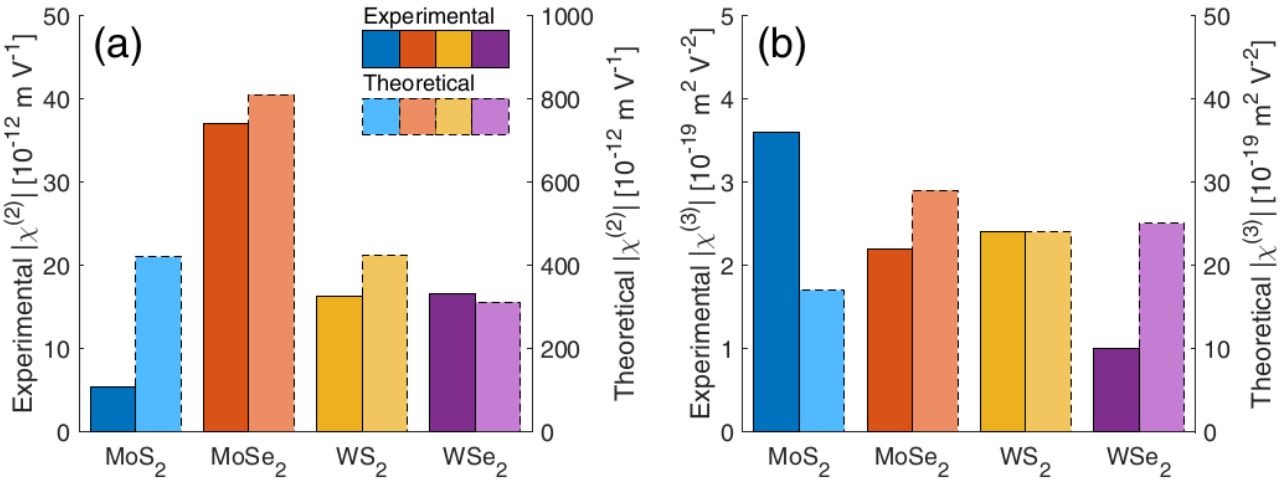


**Figure 1.5.** Comparison of experimental and theoretical effective bulk-like a) $|\chi^{(2)}|$ and b) $|\chi^{(3)}|$ of four TMDs at 1560 nm excitation. Reproduced from Ref. 8.

## References


[1] A. Autere, H. Jussila, Y. Dai, Y. Wang, H. Lipsanen, Z. Sun, *Adv. Mater.* **2018**, 30, 1705963.

[2] M. Zhao, Z. Ye, R. Suzuki, Y. Ye, H. Zhu, J. Xiao, Y. Wang, Y. Iwasa, X. Zhang, *Light Sci. Appl.* **2016**, 5, e16131.

[3] N. Kumar, S. Najmaei, Q. Cui, F. Ceballos, P. M. Ajayan, J. Lou, H. Zhao, *Phys. Rev. B* **2013**, 87, 161403.

[4] L. M. Malard, T. V. Alencar, A. P. M. Barboza, K. F. Mak, A. M. de Paula, *Phys Rev B*, **2013**, 87, 201401.

[5] Y. Li, Y. Rao, K. F. Mak, Y. You, S. Wang, C. R. Dean, T. F. Heinz, *Nano Lett* **2013**, 13, 3329–3333 (2013).

[6] H. Zeng, G.-B. Liu, J. Dai, Y. Yan, B. Zhu, R. He, L. Xie, S. Xu, X. Chen, W. Yao, X. Cui, *Sci. Rep.* **2013**, 3, 1608.

[7] X. Yin, Z. Ye, D. A. Chenet, Y. Ye, K. O'Brien, J. C. Hone, X. Zhang, *Science* **344**, 488–490 (2014)

[8] A. Autere, H. Jussila, A. Marini, J. R. M. Saavedra, Y. Dai, A. Säynätjoki, L. Karvonen, H. Yang, B. Amirsolaimani, R. A. Norwood, N. Peyghambarian, H. Lipsanen, K. Kieu, F. J. G. de Abajo, Z. Sun, *Physical Review B* **2018**, 98, 115426.

## 1.3. Nonlinear optical microscopy imaging

Nonlinear optical effects have been combined with microscopy techniques, in order to acquire spatially resolved SHG or THG intensities, forming images. A typical such methodology is performed by scanning a laser beam over the sample with two galvanometric (galvo) mirrors (raster-scanning), and recording the counts from a photomultiplier tube at each position of the laser beam [1, 2]. Importantly, this methodology has been adopted in all the research works presented in this thesis (Chapters 2-5).

For example, SHG and THG imaging have enabled the rapid visualization of grain boundaries in monolayer $MoS_2$ (**Fig. 1.6**) [1]. Furthermore, P-SHG imaging has been demonstrated to quantify the crystal quality in 2D TMDs (**Fig. 1.7**) [2].

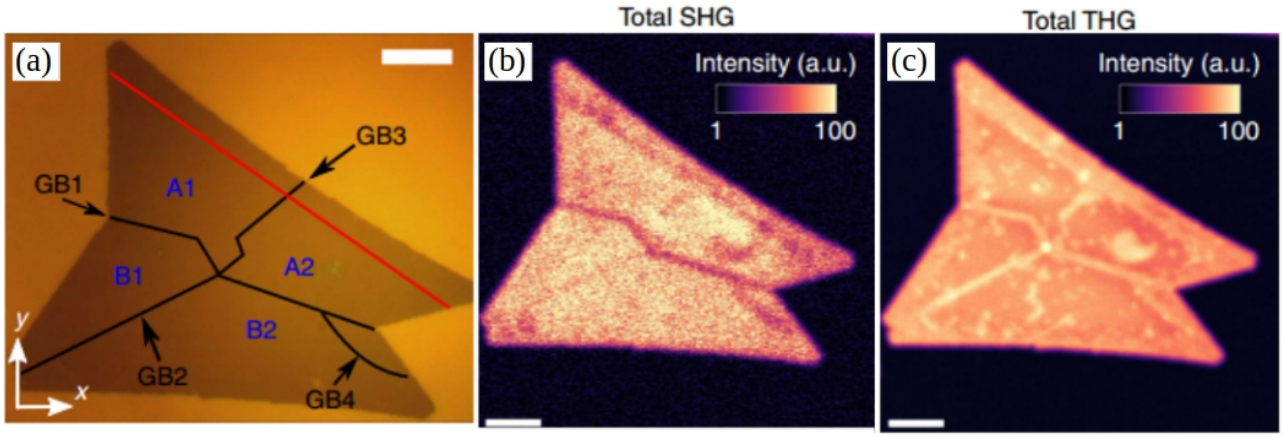


**Figure 1.6.** a) Optical image with marked grains (A1, A2, B1 and B2) and grain boundaries (GB1, GB2, GB3 and GB4). b) Experimental SHG image without analyser c) Experimental THG image without analyser. Scale bars illustrate 10 mm. Reproduced from Ref. 1.

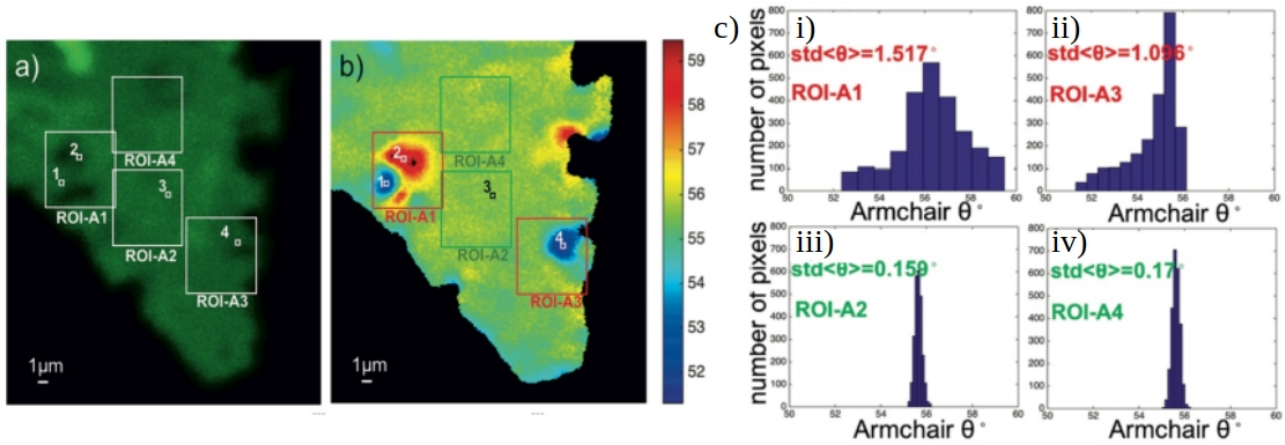

**Figure 1.7.** a) SHG image of monolayer $WS_2$. Four regions of interest are shown. b) Mapping of the armchair crystallographic direction. c) Image histograms showing the distribution of armchair orientations inside the four regions of interest. The crystal quality is reflected in the standard deviation of the mean armchair direction. Small standard deviation values are indicative of good crystal quality. Reproduced from Ref. 2.

## References

[1] L. Karvonen, A. Säynätjoki, M. J Huttunen, A. Autere, B. Amirsolaimani, R. A. Norwood, N. Peyghambarian, H. Lipsanen, G. Eda, K. Kieu, Z. Sun, *Nat. Commun.* **2017**, 8, 15714.
[2] S. Psilodimitrakopoulos, L. Mouchliadis, I. Paradisanos, A. Lemonis, G. Kioseoglou, E. Stratakis, *Light: Sci. Appl.* **2018**, 7, 18005.

## 1.4. Experimental setup

A schematic illustration of the experimental setup we have used in the research works presented in this thesis (Chapters 2-5), is shown in **Fig. 1.8**. This setup was mainly developed by Dr. Sotiris Psilodimitrakopoulos, with the valuable support of Andreas Lemonis, in the facilities of the Ultrafast Laser Micro- and Nano- processing (ULMNP) group, led by Dr. Emmanuel Stratakis, at IESL-FORTH.

Note that in some research works, the experimental setup may exhibit differences in comparison with the illustration of **Fig. 1.8**. For instance, the optical parametric oscillator was installed after the movement of the facilities of the ULMNP group in STEP-C, and after the projects described in Chapters 2 and 3 were completed. Furthermore, in the experimental results presented in Chapters 3 and 5, instead of a polarizer in the detection path, a polarizing beam splitter was used.

The setup is based on a fs laser beam coupled to a microscope. The linear polarization of the excitation beam is rotated by rotating a half-wave retardation plate, which is placed in a motorized rotation stage. A pair of galvanometric (galvo) mirrors allows the laser beam to scan over the stationary sample. We record the counts of the nonlinear optical signals using detectors which are based on photomultiplier tubes, at each position of the laser beam, acquiring spatially resolved SHG or THG signals, forming images. At the microscope turret box, we have the choice of using either a

silver-coated mirror or a short-pass dichroic mirror, both at 45°, depending on whether we detect the nonlinear optical signal in the forward direction (silver-coated mirror), or the backwards or both simultaneously (dichroic mirror). The experimental measurements presented in this thesis were recorded in the forward detection geometry. More details on the experimental setup are discussed within each chapter.

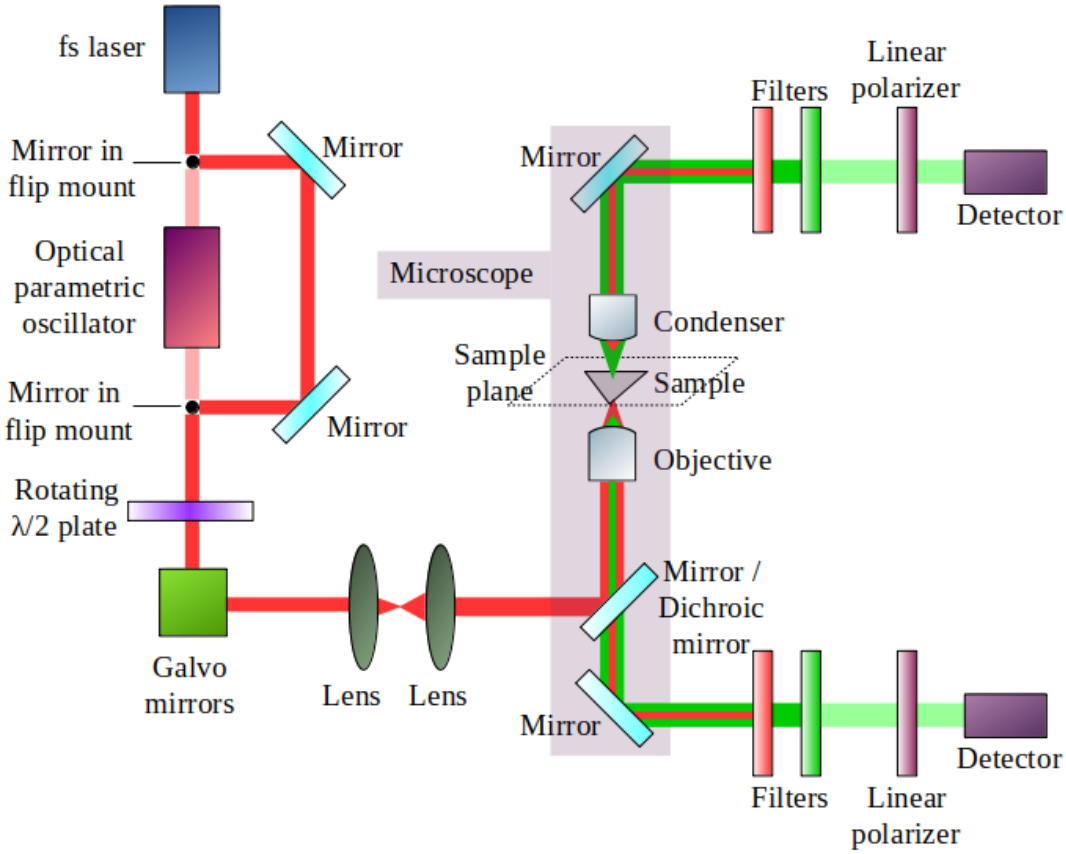


**Figure 1.8.** Schematic illustration of the experimental setup.

## 1.5 P-SHG equation in 2D TMDs

In this thesis, we have explored three nonlinear optical equations, namely P-SHG in TMDs (Chapter 2), P-SHG in MXs (Chapter 4), and P-THG in MXs (Chapter 5). The expressions we have derived relate the SHG or THG intensities with the angle of the linear polarization of the laser field, as well as the crystallographic axis. In addition, in the case of SnS crystals which exhibit anisotropy, the SHG or THG intensities are also related with relative magnitudes of $\chi^{(2)}$ (Chapter 4) and $\chi^{(3)}$ (Chapter 5) tensor components. These equations were derived based on the basic principles of a

methodology that was introduced by Dr. Leonidas Mouchliadis [1]. Each equation is discussed within the corresponding chapter. Here we present a more analytical description for the first case, the P-SHG in TMDs [1, 2], which is also discussed in Chapter 2.2.1.

The nonlinear polarization leading to SHG can be described by the matrix equation [3, p. 39]:

$$\begin{pmatrix} P_x^{2\omega} \\ P_y^{2\omega} \\ P_z^{2\omega} \end{pmatrix} = \varepsilon_0 \chi^{(2)} \begin{pmatrix} E_x^{\omega} E_x^{\omega} \\ E_y^{\omega} E_y^{\omega} \\ E_z^{\omega} E_z^{\omega} \\ 2\,E_y^{\omega} E_z^{\omega} \\ 2\,E_x^{\omega} E_z^{\omega} \\ 2\,E_x^{\omega} E_y^{\omega} \end{pmatrix} \qquad (7)$$

where the $\chi^{(2)}$ tensor is given by [3, p. 39]:

$$\chi^{(2)} = \begin{pmatrix} x_{xxx}^{(2)} & x_{xyy}^{(2)} & x_{xzz}^{(2)} & x_{xyz}^{(2)} & x_{xxz}^{(2)} & x_{xxy}^{(2)} \\ x_{yxx}^{(2)} & x_{yyy}^{(2)} & x_{yzz}^{(2)} & x_{yyz}^{(2)} & x_{yxz}^{(2)} & x_{yxy}^{(2)} \\ x_{zxx}^{(2)} & x_{zyy}^{(2)} & x_{zzz}^{(2)} & x_{zyz}^{(2)} & x_{zxz}^{(2)} & x_{zxy}^{(2)} \end{pmatrix} \qquad (8)$$

The nonzero elements of this tensor depend on the crystal symmetry of the material under study. The crystal structure of monolayer TMDs is schematically shown in **Fig. 1.9a**. Monolayer TMDs belong to hexagonal $D_{3h}$ space group, and $\chi^{(2)}$ has four nonzero elements, which are interrelated [4], namely:

$$\chi_{xxx}^{(2)} = -\chi_{xyy}^{(2)} = -\chi_{yyx}^{(2)} = -\chi_{yxy}^{(2)} \equiv \chi^{(2)} \qquad (9)$$

where x, y, z denote the crystalline coordinates, with x corresponding to the armchair direction, i.e., the mirror symmetry axis, and y corresponding to the zigzag direction [4]. Thus, Eq. 7 becomes:

$$\begin{pmatrix} P_x^{2\omega} \\ P_y^{2\omega} \\ P_z^{2\omega} \end{pmatrix} = \varepsilon_0 \chi_{xxx}^{(2)} \begin{pmatrix} 1 & -1 & 0 & 0 & 0 & 0 \\ 0 & 0 & 0 & 0 & 0 & -1 \\ 0 & 0 & 0 & 0 & 0 & 0 \end{pmatrix} \begin{pmatrix} E_x^{\omega} E_x^{\omega} \\ E_y^{\omega} E_y^{\omega} \\ E_z^{\omega} E_z^{\omega} \\ 2\,E_y^{\omega} E_z^{\omega} \\ 2\,E_x^{\omega} E_z^{\omega} \\ 2\,E_x^{\omega} E_y^{\omega} \end{pmatrix} \Rightarrow \qquad (10)$$

$$\begin{pmatrix} P_x^{2\omega} \\ P_y^{2\omega} \end{pmatrix} = \varepsilon_0 \chi_{xxx}^{(2)} \begin{pmatrix} \left(E_x^{\omega}\right)^2 - \left(E_y^{\omega}\right)^2 \\ -2\,E_x^{\omega} E_y^{\omega} \end{pmatrix} \qquad (11)$$

expressed in crystalline coordinates.

In order to treat this equation, we employ the Jones formalism [5, p. 389, 6, Chapter 11.3]. In this formalism, the polarization state of a polarized light beam is represented by a Jones vector, and the

effect of an optical element, such as a polarizer, is represented by a Jones matrix [5, p. 389, 6, Chapter 11.3].

In the experimental configuration, we consider two coordinate systems: the laboratory X, Y, Z and the crystalline x, y, z, where Z≡z (**Fig. 1.9b**). The x-axis is considered to be parallel to the armchair crystallographic direction, and at angle θ, with respect to X-laboratory axis. The angle θ is constant and unknown. The direction of the linear polarization of the laser field is considered to be at an angle φ, with respect to X-laboratory axis. The angle φ is controlled and rotated by rotating a half-waveplate, performing P-SHG. At the sample plane, the laser excitation beam propagates along Z-laboratory axis, at normal incident on the crystal, and is linearly polarized along the sample plane, i.e., we consider $E_Z^{\omega}=0$.

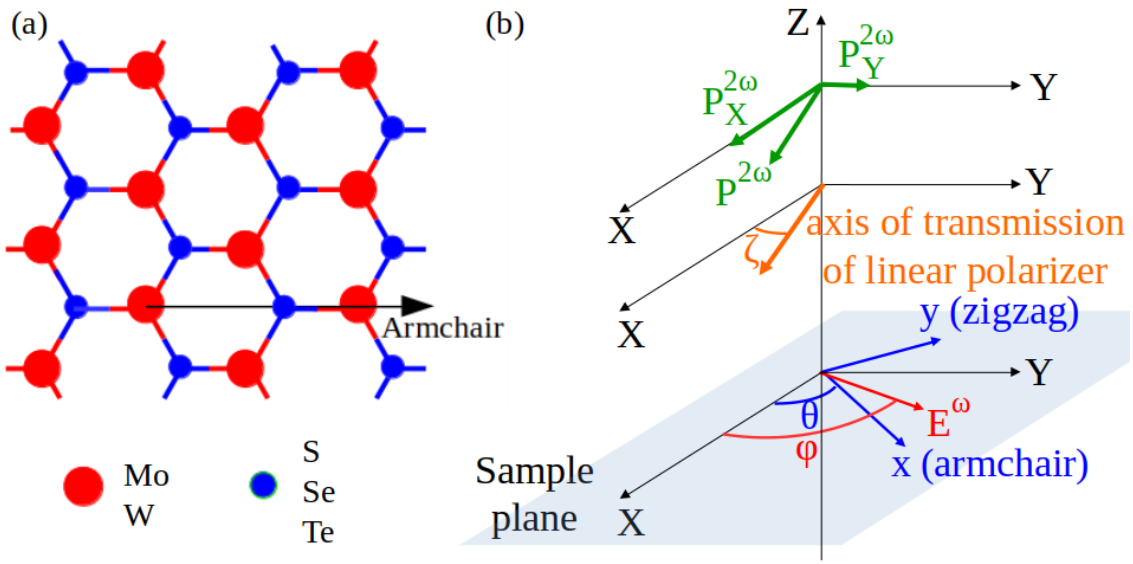


**Fig. 1.9.** a) Schematic illustration of the crystal structure of monolayer TMDs as seen top view. b) Schematic illustration showing the two coordinates systems adopted in our experimental configuration and the definition of angles adopted in our analysis.

The initial polarization state of the laser excitation field past the half-waveplate can be expressed in laboratory coordinates by the Jones vector:

$$E_0=\begin{pmatrix}E_X^{\omega}\\E_Y^{\omega}\end{pmatrix}=\begin{pmatrix}cos\varphi\\sin\varphi\end{pmatrix} \qquad (12)$$

where the amplitude of the electric field is normalized to unity. This vector can be transformed in crystalline coordinates by multiplying with the rotation matrix $\begin{pmatrix}cos\theta & sin\theta\\ -sin\theta & cos\theta\end{pmatrix}$, obtaining:

$$E=\begin{pmatrix}E_x^{\omega}\\E_y^{\omega}\end{pmatrix}=\begin{pmatrix}cos\theta & sin\theta\\-sin\theta & cos\theta\end{pmatrix}E_0=\begin{pmatrix}cos\theta & sin\theta\\-sin\theta & cos\theta\end{pmatrix}\begin{pmatrix}cos\varphi\\sin\varphi\end{pmatrix}\Rightarrow$$

$$E=\begin{pmatrix}E_x^{\omega}\\E_y^{\omega}\end{pmatrix}=\begin{pmatrix}\cos(\varphi-\theta)\\\sin(\varphi-\theta)\end{pmatrix} \qquad (13)$$

By substituting Eq. 13 into Eq. 11, which are both in crystalline coordinates, we obtain:

$$\begin{pmatrix}P_x^{2\omega}\\P_y^{2\omega}\end{pmatrix}=\varepsilon_0\chi_{xxx}^{(2)}\begin{pmatrix}(E_x^{\omega})^2-(E_y^{\omega})^2\\-2E_x^{\omega}E_y^{\omega}\end{pmatrix}\sim\begin{pmatrix}\cos^2(\varphi-\theta)-\sin^2(\varphi-\theta)\\-2\cos(\varphi-\theta)\sin(\varphi-\theta)\end{pmatrix}\sim\begin{pmatrix}\cos(2(\theta-\varphi))\\\sin(2(\theta-\varphi))\end{pmatrix} \qquad (14)$$

This expression is then transformed into laboratory coordinates by multiplying with the rotation matrix $\begin{pmatrix}cos\theta & -sin\theta\\sin\theta & cos\theta\end{pmatrix}$, obtaining:

$$\begin{pmatrix}P_X^{2\omega}\\P_Y^{2\omega}\end{pmatrix}\sim\begin{pmatrix}cos\theta & -sin\theta\\sin\theta & cos\theta\end{pmatrix}\begin{pmatrix}P_x^{2\omega}\\P_y^{2\omega}\end{pmatrix}\sim\begin{pmatrix}cos\theta & -sin\theta\\sin\theta & cos\theta\end{pmatrix}\begin{pmatrix}\cos(2(\theta-\varphi))\\\sin(2(\theta-\varphi))\end{pmatrix}\sim\begin{pmatrix}\cos(\theta+2(\theta-\varphi))\\\sin(\theta+2(\theta-\varphi))\end{pmatrix}\Rightarrow$$

$$\begin{pmatrix}P_X^{2\omega}\\P_Y^{2\omega}\end{pmatrix}\sim\begin{pmatrix}\cos(3\theta-2\varphi)\\\sin(3\theta-2\varphi)\end{pmatrix} \qquad (15)$$

Finally, before the detector, we use a polarizer at angle ζ with respect to X-laboratory axis, which collects a specific polarization component of the SHG field. In order to take into account the effect of the polarizer, we multiply with the Jones matrix of the polarizer [6, Chapter 11.3], and we have:

$$\begin{pmatrix}P_X^{2\omega}\\P_Y^{2\omega}\end{pmatrix}_{Final}\sim\begin{pmatrix}\cos^2\zeta & \cos\zeta\sin\zeta\\\cos\zeta\sin\zeta & \sin^2\zeta\end{pmatrix}\begin{pmatrix}P_X^{2\omega}\\P_Y^{2\omega}\end{pmatrix}\sim\begin{pmatrix}\cos^2\zeta & \cos\zeta\sin\zeta\\\cos\zeta\sin\zeta & \sin^2\zeta\end{pmatrix}\begin{pmatrix}\cos(3\theta-2\varphi)\\\sin(3\theta-2\varphi)\end{pmatrix}\Rightarrow$$

$$\begin{pmatrix}P_X^{2\omega}\\P_Y^{2\omega}\end{pmatrix}_{Final}\sim\begin{pmatrix}\cos\zeta(\cos\zeta\cos(3\theta-2\varphi)+\sin\zeta\sin(3\theta-2\varphi))\\\sin\zeta(\cos\zeta\cos(3\theta-2\varphi)+\sin\zeta\sin(3\theta-2\varphi))\end{pmatrix}\sim\begin{pmatrix}\cos\zeta(\cos(\zeta-3\theta+2\varphi))\\\sin\zeta(\cos(\zeta-3\theta+2\varphi))\end{pmatrix} \qquad (16)$$

Therefore, the SHG intensity can be expressed as:

$$I^{2\omega}\sim\left|(P_X^{2\omega})_{Final}\right|^2+\left|(P_Y^{2\omega})_{Final}\right|^2\Rightarrow \qquad (17)$$

$$I^{2\omega}=A\cos^2(\zeta-3\theta+2\varphi) \qquad (18)$$

where A is a multiplication factor that depends on $\chi_{xxx}^{(2)}$ and the amplitude of the excitation field.

For $\zeta=0^0$, i.e. polarizer paraller to X-laboratory axis, the SHG intensity reads:

$$I_X^{2\omega}=A\cos^2(3\theta-2\varphi) \qquad (19)$$

while for $\zeta=90^0$, i.e. polarizer paraller to Y-laboratory axis, the SHG intensity is given by:

$$I_Y^{2\omega}=A\sin^2(3\theta-2\varphi) \qquad (20)$$

If we plot the SHG intensity given by Eq. 18, in a polar diagram, as function of the angle φ (which describes the direction of the linear polarization of the laser, and which we vary, acquiring P-SHG

measurements), we obtain a four-lobe pattern, which rotates for different values of the armchair direction θ (**Fig. 2.3a**). Therefore, by fitting the experimental P-SHG measurements with Eq. 18, we can calculate the unknown armchair direction.

Interestingly, if the polarizer is not placed in a fixed position, but instead it is rotated always parallel to the direction of the excitation linear polarization (by the same angle, i.e., ζ=φ), Eq. 17 becomes:

$$I^{2\omega} = A\cos^2\left(3\left(\varphi - \theta\right)\right)$$

in accordance with the literature finding [7]. In this case, the P-SHG polar diagram, instead of a four-lobe pattern, exhibits a six-lobe one, which rotates for different values of the armchair direction θ (**Fig. 1.10**) [7].

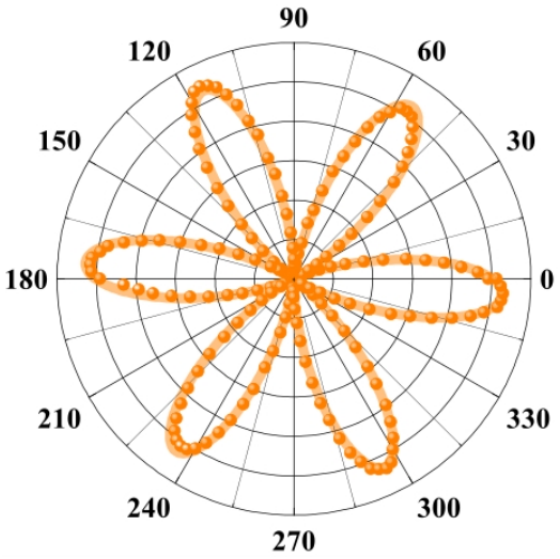


**Fig. 1.10.** a) Polarized SHG in $WSe_2$, where the incident pump linear polarization and a parallel polarizer were rotated simultaneously by the same angle, while recording the spectrum. Reproduced from Ref. 5.

As we shall extensively discuss in Chapter 4, the P-SHG behavior of orthorhombic SnS crystals is different than the P-SHG behavior of TMD crystals. In SnS, the shape itself of the P-SHG polar diagram is found, both theoretically and experimentally, to change for different values of the armchair direction. This behavior is attributed to the in-plane anisotropy of SnS [8].

## References

[1] S. Psilodimitrakopoulos, L. Mouchliadis, I. Paradisanos, A. Lemonis, G. Kioseoglou, E. Stratakis, *Light: Sci. Appl.* **2018**, 7, 18005.

[2] G. M. Maragkakis, S. Psilodimitrakopoulos S, L. Mouchliadis, I. Paradisanos, A. Lemonis, G. Kioseoglou, E. Stratakis, *Opto-Electron Adv* **2019**, 2, 190026.
[3] R. W. Boyd, *Nonlinear Optics*, Academic Press, Elsevier 2020.
[4] L. M. Malard, T. V. Alencar, A. P. M. Barboza, K. F. Mak, A. M. de Paula, *Phys Rev B*, **2013**, 87, 201401.
[5] E. Hecht, *Optics*, Pearson Education Limited 2017.
[6] D. Goldstein and E. Collett, *Polarized Light*, 2nd ed., Marcel Dekker, Inc 2003.
[7] H. G. Rosa, Y. W. Ho, I. Verzhbitskiy, M. J. F. L. Rodrigues, T. Taniguchi, K. Watanabe, G. Eda, V. M. Pereira, J. C. V. Gomes, *Sci Rep* **2018**, 8, 10035.
[8] G. M. Maragkakis, S. Psilodimitrakopoulos, L. Mouchliadis, A. S. Sarkar, A. Lemonis, G. Kioseoglou, E. Stratakis, *Adv. Optical Mater.* **2022**, 10, 2270038.

## 1.6 State of the art - Imaging the crystal orientation of 2D TMDs using P-SHG

2D TMDs are atomically thin crystals of the type $MX_2$, where M is a transition metal atom (Mo, W), and X a chalcogen atom (S, Se, or Te). As part of the family of 2D materials, established by the breakthrough creation of single-layer graphene [1, 2], 2D TMDs share the reduced dimensionality and similar crystal structure. Unlike graphene, however, they are direct bandgap semiconductors, exhibiting a variety of remarkable properties, such as strong photoluminescence [3, 4], optical valley polarization [5-8], high transistor on-off ratio [9], and large exciton binding energies [10, 11]. These exciting characteristics of 2D TMDs offer an ideal field for fundamental studies, as well as numerous possible applications in various research fields [12], including, electronics and optoelectronics [13, 14], energy harvesting [15], valleytronics [16], and biomedicine [17, 18].

The realization of technology and devices based on 2D atomic crystals presupposes the ability to create large-area films of good quality and minimum imperfections, given that defects unavoidably affect the material behavior [19-21]. These polycrystalline films consist of single-crystalline areas of varying orientation, and grain boundaries [22], i.e. the interface regions between crystallites. In such materials, types of defects include the poor domain connectivity between grain boundaries, and the absence of homogeneity in crystalline orientation, material thickness and layer stacking. Unfortunately, state-of-the-art, large-area crystal growth techniques, such as CVD, often fail in producing defect-free materials, and moreover, there is currently no easily applicable, non-invasive and fast characterization method of the quality of 2D crystals.

Recently, the potential for nonlinear optical processes in TMDs has been attracting significant scientific interest. Several groups have explored methodologies to acquire information about the TMD crystals by analyzing their second harmonic generation (SHG) signal [23-31], which is very sensitive to crystal symmetry. The capability of mapping the armchair orientation distribution over large areas of 2D materials with high resolution, could provide a unique tool towards the evaluation of their crystal quality.

## References


[1] Novoselov KS, Jiang D, Schedin F, Booth TJ, Khotkevich VV et al. Two-dimensional atomic crystals. Proc Natl Acad Sci U.S.A. **102**, 10451-10453 (2005).

[2] Novoselov KS, Geim AK, Morozov SV, Jiang D, Zhang Y et al. Electric field effect in atomically thin carbon films. Science **306**, 666-669 (2004).

[3] Mak KF, Lee C, Hone J, Shan J, Heinz TF. Atomically thin $MoS_2$: a new direct-gap semiconductor, Phys Rev Lett **105**, 136805(4) (2010).

[4] Splendiani A, Sun L, Zhang Y, Li T, Kim J et al. Emerging photoluminescence in monolayer $MoS_2$. Nano Lett **10**, 1271–1275 (2010).

[5] Xiao D, Liu GB, Feng W, Xu X, Yao W. Coupled spin and valley physics in monolayers of MoS2 and other group-VI dichalcogenides. Phys Rev Lett **108**, 196802 (2012).

[6] Mak KF, He K, Shan J, Heinz TF. Control of valley polarization in monolayer $MoS_2$ by optical helicity. Nat Nanotech **7**, 494–498 (2012).

[7] Zeng H, Dai J, Yao W, Xiao D, Cui X. Valley polarization in $MoS_2$ monolayers by optical pumping. Nat Nanotech **7**, 490–493 (2012).

[8] Kioseoglou G, Hanbicki AT, Currie M, Friedman AL, Gunlycke D, Jonker BT. Valley polarization and intervalley scattering in monolayer MoS2. Appl Phys Lett **101**, 221907 (2012)

[9] Radisavljevic B, Radenovic A, Brivio J, Giacometti V, Kis A. Single-layer MoS2 transistors. Nat Nanotech **6**, 147–150 (2011).

[10] Wang G, Chernikov A, Glazov MM, Heinz TF, Marie X et al. Colloquium: excitons in atomically thin transition metaldichalcogenides. Rev Mod Phys **90**, 021001 (2018).

[11] Paradisanos I, Germanis S, Pelekanos NT, Fotakis C, Kymakis E et al. Room temperature observation of biexcitons in exfoliated $WS_2$ monolayers. Appl Phys Lett **110**, 193102 (2017).

[12] Ferrari AC, Bonaccorso F, Falko V, Novoselov KS, Roche S et al. Science and Technology Roadmap for Graphene, Related Two-Dimensional Crystals, and Hybrid Systems. Nanoscale **7**, 4598−4810 (2015).

[13] Wang QH, Kalantar-Zadeh K, Kis A, Coleman JN, Strano MS. Electronics and optoelectronics of two-dimensional transition metal dichalcogenides. Nat Nanotechnol **7**, 699–712 (2012).

[14] Mak KF, Shan J. Photonics and optoelectronics of 2D semiconductor transition metal dichalcogenides. Nat Photonics **10**, 216–226 (2016).

[15] Bonaccorso F, Colombo L, Yu G, Stoller M, Tozzini V et al. Graphene, related two-dimensional crystals, and hybrid systems for energy conversion and storage. Science **347,** 6217 (2015).

[16] Schaibley JR, Yu H, Clark G, Rivera P, Ross JS et al. Valleytronics in 2D materials. Nat Rev Mat **1**, 16055 (2016).

[17] Kalantar-zadeh K, Ou JZ, Daeneke T, Strano MS, Pumera M, Gras SL. Two Dimensional Transition Metal Dichalcogenides in Biosystems. Adv Funct Mater **25**, 5086-5099 (2015).

[18] Li X, Shan JY, Zhang WZ, Su S, Yuwen LH, Wang, LH. Recent Advances in Synthesis and Biomedical Applications of Two Dimensional Transition Metal Dichalcogenide Nanosheets. Small **13**, 1602660 (2017).

[19] Najmaei S, Yuan JT, Zhang J, Ajayan P, Lou J. Synthesis and defect investigation of two-dimensional molybdenum disulfide atomic layers. Acc Chem Res **48**, 31-40 (2015).

[20] Zou X, Yakobson BI. An open canvas-2D materials with defects, disorder, and functionality. Acc Chem Res **48**, 73–80 (2015).

[21] Paradisanos I, Pliatsikas N, Patsalas P, Fotakis C, Kymakis E et al. Spatial non-uniformity in exfoliated $WS_2$ single layers. Nanoscale **8**, 16197–16203 (2016).

[22] van der Zande AM, Huang PY, Chenet DA, Berkelbach TC, You YM et al. Grains and grain boundaries in highly crystalline monolayer molybdenum disulphide. Nat Mater **12,** 554–561 (2013)

[23] Psilodimitrakopoulos S, Mouchliadis L, Paradisanos I, Lemonis A, Kioseoglou G, Stratakis E. Ultrahigh-resolution Nonlinear Optical Imaging of the Armchair Orientation in 2D Transition Metal Dichalcogenides. Light. Light: Sci Appl **7**, 18005 (2018)

[24] Kumar N, Najmaei S, Cui QN, Ceballos F, Ajayan PM et al. Second harmonic microscopy of monolayer $MoS_2$. Phys Rev B **87**, 161403 (2013).

[25] Malard LM, Alencar TV, Barboza APM, Mak KF, de Paula AM. Observation of intense second harmonic generation from $MoS_2$ atomic crystals. Phys Rev B **87**, 201401 (2013).

[26] Li YL, Rao Y, Mak KF, You YM, Wang SY et al. Probing symmetry properties of few-layer $MoS_2$ and h-BN by optical second-harmonic generation. Nano Lett **13**, 3329–3333 (2013).

[27] Yin X, Ye Z, Chenet DA, Ye Y, O'Brien K et al. Edge nonlinear optics on a $MoS_2$ atomic monolayer. Science **344**, 488–490 (2014)
[28] Clark DJ, Senthilkumar V, Le CT, Weerawarne DL, Shim B et al. Strong optical nonlinearity of CVD-grown MoS 2 monolayer as probed by wavelength-dependent second-harmonic generation. Phys Rev B **90**, 121409 (2014).
[29] Hsu WT, Zhao ZA, Li LJ, Chen CH, Chiu MH et al. Second harmonic generation from artificially stacked transition metal dichalcogenide twisted bilayers. ACS Nano **8**, 2951–2958 (2014).
[30] Wang Y, Xiao J, Yang S, Wang Y, Zhang X. Second harmonic generation spectroscopy on two-dimensionalmaterials. Opt. Mater. Express **9**(3), 1136–1149 (2019).
[31] Zhao M, Ye Z, Suzuki R, Ye Y, Zhu et al. Atomically phase-matched second-harmonic generation in a 2D crystal. Light Sci. Appl. **5**, e16131 (2016).

## 1.7 State of the art - Real-time spatially resolved determination of twist angle in TMD heterobilayers

Stacks of TMD monolayers, or commonly called van der Waals heterostructures, offer exciting opportunities for the study of novel optical phenomena. Vertical stacks of different TMD layers, in particular, exhibit new optoelectronic properties, not present in the constituent materials [1]. For example, the first reports on a $MoSe_2/WSe_2$ TMD heterobilayer revealed a new type of bound electron-hole state, the intralayer exciton, which has the electron and hole located within one layer of a TMD [2]. Recently, the existence of a bound electron-hole pair, with the carriers located in adjacent monolayers, coined as the interlayer exciton, was additionally discovered [3-5]. The $MoSe_2/WSe_2$ heterostructure allows the formation of excitons from electrons and holes in distinct layers, producing interlayer excitons with large binding energy and long lifetime [6]. On the other hand, in a heterostructure built from two $MoS_2$ monolayers separated by an atomically thin h-BN spacer, the electrons and holes generated in the system are accumulated in the opposite monolayers and form bosonic bound states, the indirect excitons. The long lifetime of interacting indirect excitons leads to local exciton superfluidity which produces superconducting states at room temperature [7]. Furthermore, evidence of interlayer exciton condensation in 2D $MoSe_2/WSe_2$ layers has been presented, creating opportunities for exploring condensate-based optoelectronics and exciton-mediated high-temperature superconductivity [8]. It has been further reported that an

optically-generated spin-valley polarization in one monolayer can be transferred accross layers of a 2D $MoSe_2/WSe_2$ heterostructure [9].

In a TMD heterobilayer, the two constituent layers might possess different crystal orientations and different lattice periods. This difference in the crystal orientations is described in terms of a moiré pattern. A moiré pattern introduces a new periodicity in the atomic structure that influences the electron and hole tunnelling between the two layers. Recently, experimental evidence of interlayer excitons trapped in a moiré potential of a $MoSe_2/WSe_2$ heterobilayer was reported [10]. The periodicity of this moiré superlattice is determined by the mismatch in the lattice constants of the constituent layers and by the twist angle between the layers [11, 12]. A moiré pattern can be controlled by the rotation between the adjacent layers, and in this context, twist angles and moiré patterns have been regarded as new degrees of freedom, enabling tuning of the physical properties of stacked 2D TMDs upon tailoring their interlayer coupling [13, 14]. For example, long-lived interlayer excitons in $MoSe_2/WSe_2$ heterostructures have been formed through electrical control of the individual layers [15], while a dynamically rotated heterostructure has also been demonstrated [16]. The above representative observations indicate the strong potential to harness and tune the physical properties of 2D TMD heterostructures via the adjustment of the twist angle between the stacked layers.

So far, the techniques used to calculate the twist angle in heterobilayers are based either on simple observations of scanning electron microscopy (SEM) images, for identifying sharp edges indicative of the zig-zag termination [13], or on the analysis of SHG signals [9-12, 14, 17]. The latter appears to be the most reliable method for the determination of the twist angle in TMD heterobilayers. Indeed, in recent publications on TMD heterobilayers, twist angles have been calculated using polarization-resolved SHG (P-SHG) or phase-resolved SHG techniques [9-11]. Within the P-SHG approach, the crystal orientation of a TMD monolayer is obtained either by rotating the sample or by rotating the excitation linear polarization parallel to a rotating analyzer in front of the detector [9-12, 14, 17]. On the other hand, by using phase-resolved SHG measurements, the AA or AB stacking is also identified [9-11].

In the aforementioned studies [9-12, 14, 17], the SHG signals were acquired solely from monolayer regions and subsequently the individual main crystallographic directions (defined by the corresponding armchair angle) measured for each monolayer were used to deduce the twist angle in the overlapping region. Unavoidably, this methodology requires many measurements and post-

processing fitting in order to obtain the result, a time-consuming process. Furthermore, all such methods do not take into account the interference between the SHG signals originating from the two individual monolayers, in their overlapping area [18]. Therefore, an interference-based method should be the most reliable for calculating a twist angle, since it can provide the result in a single step directly at the overlapping region, without relying on its indirect determination via the subtraction of the armchair angles from individual monolayers. It was only recently when a P-SHG methodology was reported, that maps with high accuracy the twist angle in the overlapping region of TMD homobilayers [19]. The method was based on the optical contrast, due to interference of the respective SHG signals, obtained from the overlapping region of stacked monolayers, enabling optical mapping of the twist angle.

## References


[1] He, J., Hummer, K. & Franchini, C. Stacking effects on the electronic and optical properties of bilayer transition metal dichalcogenides $MoS_2$, $MoSe_2$, $WS_2$, and $WSe_2$. Phys. Rev. B **89**, 075409 (2014).

[2] Mueller, T. & Malic, E. Exciton physics and device application of two-dimensional transition metal dichalcogenide semiconductors. npj 2D Mater. Appl. **2**, 29 (2018).

[3] Yu, H., Wang, Y., Tong, Q., Xu, X. & Yao, W. Anomalous Light Cones and Valley Optical Selection Rules of Interlayer Excitons in Twisted Heterobilayers. Phys. Rev. Lett. **115**, 187002 (2015).

[4] Kunstmann, J. et al. Momentum-space indirect interlayer excitons in transition-metal dichalcogenide van der Waals heterostructures. Nature Physics **14**, 801–805 (2018).

[5] Rivera, P. et al. Interlayer valley excitons in heterobilayers of transition metal dichalcogenides. Nature Nanotech. **13,** 1004–1015 (2018).

[6] Tartakovskii, A. Excitons in 2D heterostructures. Nat. Rev. Phys. **2,** 8–9 (2020).

[7] Fogler, M. M., Butov, L. V. & Novoselov, K. S. High temperature superfluidity with indirect excitons in van der Waals heterostructures. Nat. Commun. **5**, 4555 (2014).

[8] Wang, Z. et al. Evidence of high- temperature exciton condensation in two-dimensional atomic double layers. Nature **574**, 76–80 (2019).

[9] Schaibley, J. R. et al. Directional interlayer spin-valley transfer in two-dimensional heterostructures. Nat. Commun. **7**, 13747 (2016).

[10] Seyler, K. L. et al. Signatures of moiré-trapped valley excitons in $MoSe_2/WSe_2$ heterobilayers. Nature **567**, 66–70 (2019).

[11] Tran, K. et al. Evidence for moiré excitons in van der Waals heterostructures. Nature **567,** 71–75 (2019).

[12] Jin, C. et al. Observation of moiré excitons in $WSe_2/WS_2$ heterostructure superlattices. Nature **567,** 76–80 (2019).

[13] Nayak, P. K. et al. Probing Evolution of Twist-Angle-Dependent Interlayer Excitons in $MoSe_2$/$WSe_2$ van der Waals Heterostructures. ACS Nano **11**, 4, 4041–4050 (2017).

[14] Alexeev, E. M. et al. Resonantly hybridized excitons in moiré superlattices in van der Waals heterostructures. Nature **567,** 81–86 (2019).

[15] Jauregui, L. A. et al. Electrical control of interlayer exciton dynamics in atomically thin heterostructures. Science **366**, 6467, 870-875 (2019).

[16] Ribeiro-Palau, R. et al. Twistable electronics with dynamically rotatable heterostructures. Science **361**, 6403, 690-693 (2018).

[17] Hsu, W.-T. et al. Negative circular polarization emissions from $WSe_2/MoSe_2$ commensurate heterobilayers. Nat. Commun. **9,** 1356 (2018).

[18] Hsu, W.-T. et al. Second Harmonic Generation from Artificially Stacked Transition Metal Dichalcogenide Twisted Bilayers. ACS Nano **8**, 3, 2951–2958 (2014).

[19] Psilodimitrakopoulos, S. et al. Twist Angle mapping in layered $WS_2$ by Polarization-Resolved Second Harmonic Generation. Sci. Rep. **9**, 14285 (2019).

## 1.8 State of the art - Nonlinear optical imaging of in-plane anisotropy in 2D SnS

Group IV monochalcogenides, also known as group IV-VI metal monochalcogenides, and denoted by MX with M = Sn, Ge and X = S, Se, are a class of layered, orthorhombic, semiconducting 2D materials attracting significant interest [1-3]. They are known as phosphorene analogues [1-4], since they share similar puckered or wavy lattice structures with phosphorene, a 2D format of black phosphorus [5, 6]. The in-plane structural anisotropy of MXs, with puckered structure along the AC direction [3], is the origin of in-plane anisotropic physical properties [1-3, 7, 8]. A plethora of properties have been reported to exhibit in-plane anisotropic response, including carrier mobility [7], optical absorption, reflection, extinction, refraction [8], and Raman spectral behavior [1]. The in-plane anisotropic response is exhibited along the distinguished in-plane AC and ZZ crystallographic directions, offering an additional degree of freedom in manipulating their properties [1-3, 7, 8]. For example, polarization-sensitive photodetectors have been presented based on the intrinsic linear dichroism of GeSe [8], and black phosphorus (**Figure 1.11**) [9]. Furthermore, monolayers MXs are predicted to be multiferroic with coupled ferroelectricity and ferroelasticity,

and large spontaneous polarization [10, 11]. Indeed, in-plane ferroelectricity has been recently demonstrated for micrometer-size monolayer SnS at room temperature [12].

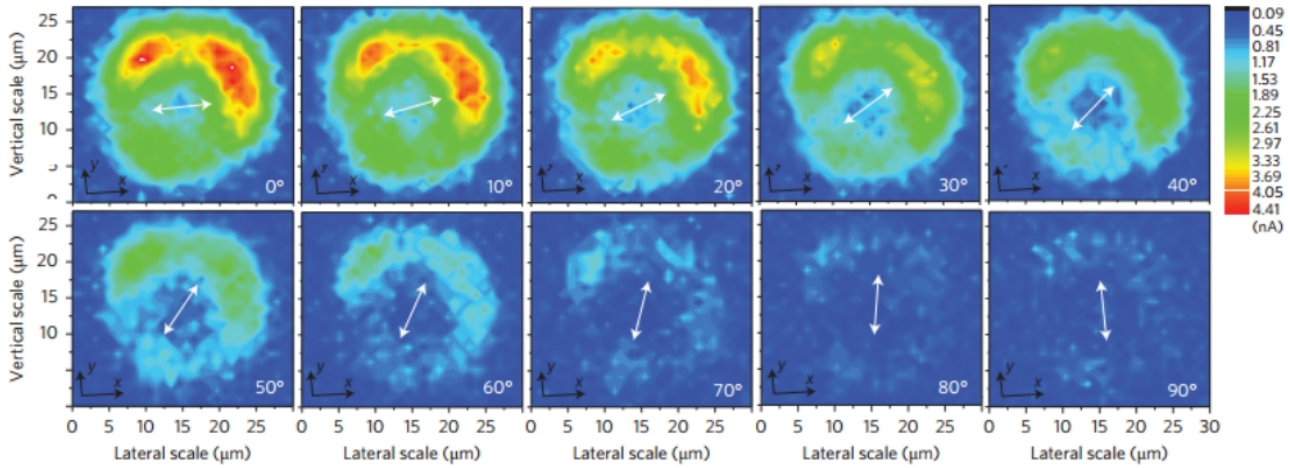


**Figure 1.11.** Photocurrent microscopy images of black phosphorus photodetector with different light polarizations (white arrows). Reproduced from Ref. 9.

Recently, the nonlinear optical properties of MXs have been addressed [12-16]. Nonlinear optics plays an important role in all aspects of modern photonics, with nonlinear media being used in photonic devices for photon generation, manipulation, transmission, detection and imaging [17-20]. Applications of nonlinear optics in a wide range of fields have been explored, including nonlinear silicon photonics [21], quantum nonlinear optics [22], nonlinear plasmonics [23], material characterization [24-26], and biomedical optics [27, 28]. SHG is possibly the most widely studied nonlinear optical process, in which radiation at twice the frequency of the incident light is generated [17-20]. It emerges in media that lack inversion symmetry, such as various 2D layered materials, and is widely used to characterize their properties [24-26, 29, 30]. Furthermore, SHG has been combined with microscopy techniques enabling imaging of 2D materials. In this context, P-SHG imaging has been recently demonstrated as a powerful tool to probe the properties of 2D group VI transition metal dichalcogenides (TMDs), such as $MoS_2$, $WS_2$, $MoSe_2$ and $WSe_2$ [31-37]. Specifically, it has enabled direct optical imaging of the atomic edges and boundaries of a 2D material, based on the observation of electronic structure changes at the edges of monolayer $MoS_2$ [31]. Furthermore, it has been used to calculate and map in a pixel-by-pixel manner the main crystallographic direction (armchair) of 2D TMDs [31-33], and quantify their crystal quality [32, 33], determine the twist-angle in TMD homobilayers [34, 35], and heterobilayers [36], and probe the valley population imbalance [37].

The 2D MXs are characterized by broken inversion symmetry, a fact that renders them suitable for SHG conversion [12-15]. Indeed, using first-principles electronic structure theory, Wang and Qian theoretically predicted giant optical SHG in monolayer MXs [13]. They predicted that the strength of SHG susceptibility of GeSe and SnSe monolayers is more than one order of magnitude higher than that of monolayer $MoS_2$. These results were also supported by another theoretical work by Panday and Fregoso [14]. Recently, Higashitarumizu et al. performed polarized SHG spectroscopy on a micrometer-size monolayer SnS [12], while Zhu et al. reported anisotropic SHG in few-layer SnS [15].

## References


[1] A. S. Sarkar, E. Stratakis, *Adv. Sci.* **2020**, 2001655.

[2] F. Xia, H. Wang, J. C. M. Hwang, A. H. C. Neto, L. Yang, *Nat. Rev. Phys.* **2019**, 1, 306.

[3] L. Li, W. Han, L. Pi, P. Niu, J. Han, C. Wang, B. Su, H. Li, J. Xiong, Y. Bando, T. Zhai, *InfoMat* **2019**, 1:54-73.

[4] L. C. Gomes, A. Carvalho, *Phys. Rev. B* **2015**, 92, 085406.

[5] H. Liu, A. T. Neal, Z. Zhu, Z. Luo, X. Xu, D. Tománek, P. D. Ye, *ACS Nano* **2014**, 8 4033-4041.

[6] A. Carvalho, M. Wang, X. Zhu, A. S. Rodin, H. Su, A. H. C. Neto, *Nat. Rev. Mater.* **2016**, 1, 16061.

[7] Z. Tian, C. Guo, M. Zhao, R. Li, J. Xue, *ACS Nano* **2017**, 11, 2219.

[8] Y. Yang, S.-C. Liu, Y. Wang, M. Long, C.-M. Dai, S. Chen, B. Zhang, Z. Sun, Z. Sun, C. Hu, S. Zhang, L. Tong, G. Zhang, D.-J. Xue, J.-S. Hu, *Adv. Opt. Mater.* **2019**, 7, 1801311.

[9] H. Yuan, X. Liu, F. Afshinmanesh, W. Li, G. Xu, J. Sun, B. Lian, A. G. Curto, G. Ye, Y. Hikita, Z. Shen, S.-C. Zhang, X. Chen, M. Brongersma, H. Y. Hwang, Y. Cui, *Nat. Nanotechnol.* **2015**, 10, 707.

[10] M. Wu, X. C. Zeng, *Nano Lett.* **2016**, 16, 3236-3241.

[11] H. Wang, X. Qian, *2D Mater.* **2017**, 4, 015042.

[12] N. Higashitarumizu, H. Kawamoto, C.-J. Lee, B.-H. Lin, F.-H. Chu, I. Yonemori, T. Nishimura, K. Wakabayashi, W.-H. Chang, K. Nagashio, *Nat. Commun.* **2020**, 11, 2428.

[13] H. Wang and X. Qian, *Nano Lett.* **2017**, 17, 5027.

[14] S.R. Panday, B. M. Fregoso, *J. Phys.: Condens. Matter* **2017**, 29, 43LT01.

[15] M. Zhu, M. Zhong, X. Guo, Y. Wang, Z. Chen, H. Huang, J. He, C. Su, K. P. Loh, *Adv. Optical Mater.* **2021**, 2101200.

[16] A. Dasgupta, J. Gao, X. Yang, *Laser Photonics Rev.* **2020**, 1900416.

[17] R. W. Boyd, *Nonlinear Optics*, Academic Press, Elsevier **2020**.

[18] Y. R. Shen, *The Principles of Nonlinear Optics*, New York, NY: Wiley Press **1984**.

[19] C. Li, *Nonlinear Optics, Principles and Applications*, Springer, Singapore **2017**.

[20] G. New, *Introduction to Nonlinear Optics*, Cambridge University Press 2011

[21] J. Leuthold, C. Koos, W. Freude, *Nat. Photonics* **2010**, 4, 535.

[22] D. E. Chang, V. Vuletic, M. D. Lukin, *Nat. Photonics* **2014**, 8, 685.

[23] M. Kauranen, A. V. Zayats, *Nat. Photonics* **2012**, 6, 737.

[24] A. Autere, H. Jussila, Y. Dai, Y. Wang, H. Lipsanen, Z. Sun, *Adv. Mater.* **2018**, 1705963.

[25] X. Wen, Z. Gong, D. Li, *InfoMat.* **2019**, 1-21.

[26] L. Zhou, H. Fu, T. Lv, C. Wang, H. Gao, D. Li, L. Deng, W. Xiong, *Nanomaterials* **2020**, 10, 2263.

[27] D. Xydias, G. Ziakas, S. Psilodimitrakopoulos, A. Lemonis, E. Bagli, T. Fotsis, A. Gravanis, D. S. Tzeranis, E. Stratakis, *Biomedical Optics Express* **2021**, 12, 2, 1136-1153.

[28] V. Tsafas, E. Gavgiotaki, M. Tzardi, E. Tsafa, C. Fotakis, I. Athanassakis, G. Filippidis, *J. Biophotonics* **2020**, 13:e202000180.

[29] Y. Wang, J. Xiao, S. Yang, Y. Wang, X. Zhang, *Opt Mater Express* **2019**, 9, 1136-1149.

[30] H. Ma, J. Liang, H. Hong, K. Liu, D. Zou, M. Wu, K. Liu, *Nanoscale* **2020**, 12, 22891-22903.

[31] X. Yin, Z. Ye, D. A. Chenet, Y. Ye, K. O'Brien, J. C. Hone, X. Zhang, *Science* **2014**, 344 , 488.

[32] S. Psilodimitrakopoulos, L. Mouchliadis, I. Paradisanos, A. Lemonis, G. Kioseoglou, E. Stratakis, *Light Sci. Appl.* **2018**, 7, 18005.

[33] G. M. Maragkakis, S. Psilodimitrakopoulos S, L. Mouchliadis, I. Paradisanos, A. Lemonis, G. Kioseoglou, E. Stratakis, *Opto-Electron Adv* **2019**, 2, 190026.

[34] S. Psilodimitrakopoulos, L. Mouchliadis, I. Paradisanos, G. Kourmoulakis, A. Lemonis, G. Kioseoglou, E. Stratakis, *Sci. Rep.* **2019**, 9, 14285.

[35] S. Psilodimitrakopoulos, A. Orekhov, L. Mouchliadis, D. Jannis, G. M. Maragkakis, G. Kourmoulakis, N. Gauquelin, G. Kioseoglou, J. Verbeeck, E. Stratakis, *npj 2D Mater. Appl.* **2021**, 5, 77.

[36] S. Psilodimitrakopoulos, L. Mouchliadis, G. M. Maragkakis, G. Kourmoulakis, A. Lemonis, G. Kioseoglou, E. Stratakis, *2D Mater.* **2021**, 8, 015015.

[37] L. Mouchliadis, S. Psilodimitrakopoulos, G. M. Maragkakis, I. Demeridou, G. Kourmoulakis, A. Lemonis, G. Kioseoglou, E. Stratakis, *npj 2D Mater. Appl.* **2021**, 5, 6.

## 1.9 State of the art - Anisotropic THG in 2D tin sulfide

The nonlinear optical properties of 2D layered materials have been recently attracting considerable interest for both fundamental studies and technological applications, based on light generation of additional frequencies and their modulation, that can also be used for material characterization [1-6]. Second harmonic generation (SHG) and THG by 2D group-VI transition metal dichalcogenides (TMD) crystals, such as $MoS_2$, $WS_2$, $MoSe_2$ and $WSe_2$, have already been at the center of this interest, providing useful information on their structural properties [1-12]. For example, THG microscopy has enabled rapid visualization of grain boundaries in monolayer $MoS_2$ [11].

Recently, another family of layered 2D materials has been gaining growing attention, namely the group-IV monochalcogenides, also known as group IV-VI metal monochalcogenides, and denoted by MX with M = Sn or Ge and X = S or Se [13-15]. MXs are layered, orthorhombic, semiconducting 2D materials, known as phosphorene analogues [13-16], given that they share similar puckered or wavy lattice structures with phosphorene, a 2D format of black phosphorus [17, 18]. Importantly, MXs feature in-plane anisotropic physical properties [13-15, 19, 20], originating from their in-plane structural anisotropy, with puckered structure along the armchair (AC) crystallographic direction [15]. Properties with reported in-plane anisotropic response include carrier mobility [19], optical absorption, reflection, extinction, and refraction [20], and Raman spectral behavior [13]. The in-plane anisotropic response is exhibited along the distinguished in-plane AC and zigzag (ZZ) crystallographic directions, offering an additional degree of freedom in manipulating their properties [13-15, 19, 20]. For example, polarization-sensitive photodetectors have been presented, based on the intrinsic linear dichroism of GeSe [20] and black phosphorus [21]. Furthermore, monolayer MXs are predicted to be multiferroic with coupled ferroelectricity and ferroelasticity, and large spontaneous polarization [22, 23]. Indeed, in-plane ferroelectricity has been demonstrated for monolayer SnS at room temperature [24]. Moreover, access to the valley-related degree of freedom has been reported [25, 26].

Recently, studies on the nonlinear optical properties of MXs have also been generating interesting research [24, 27-33]. In particular, monolayer MXs have been theoretically predicted to produce giant optical SHG [27, 28]. Moreover, polarized SHG spectroscopy on monolayer SnS [24], efficient and anisotropic SHG in few-layer SnS [29], SHG imaging of ultrathin SnS [30], and wavelength-dependent SHG from few-layer ferroelectric SnS [31] have been reported. Finally, the nonlinear optical absorption properties of SnS [32] and SnSe [33] have been studied, revealing their saturable absorption properties.

However, the THG properties of 2D SnS remain unexplored. THG is a process in which three incident photons with frequency ω generate coherent radiation with frequency 3ω [34]. Notably, THG, in contrast to SHG, does not require non-centrosymmetry, and thus can also be observed in centrosymmetric crystals. Importantly, polarization-dependent anisotropic THG has been reported for various 2D materials, including germanium selenide (GeSe) [35], which belongs to the family of MXs, black phosphorus (BP) [36-38], silicon phosphide (SiP) [39], germanium arsenide (GeAs) [40], arsenic trisulfide ($As_2S3$) [41], and rhenium disulfide ($ReS_2$) [42].

## References


[1] A. Autere, H. Jussila, Y. Dai, Y. Wang, H. Lipsanen, Z. Sun, *Adv. Mater.* **2018**, 30, 1705963.

[2] X. Wen, Z. Gong, D. Li, *InfoMat.* **2019**, 1, 317-337.

[3] L. Zhou, H. Fu, T. Lv, C. Wang, H. Gao, D. Li, L. Deng, W. Xiong, *Nanomaterials* **2020**, 10, 2263.

[4] J. W. You, S. R. Bongu, Q. Bao, N. C. Panoiu, *Nanophotonics* **2019**, 8, 1, 63–97.

[5] H. Ma, J. Liang, H. Hong, K. Liu, D. Zou, M. Wu, K. Liu, *Nanoscale* **2020**, 12, 22891-22903.

[6] Y. Wang, J. Xiao, S. Yang, Y. Wang, X. Zhang, *Opt Mater Express* **2019**, 9, 1136-1149.

[7] A. Autere, H. Jussila, A. Marini, J. R. M. Saavedra, Y. Dai, A. Säynätjoki, L. Karvonen, H. Yang, B. Amirsolaimani, R. A. Norwood, N. Peyghambarian, H. Lipsanen, K. Kieu, F. J. G. de Abajo, Z. Sun, *Physical Review B* **2018**, 98, 115426.

[8] A. Säynätjoki, L. Karvonen, H. Rostami, A. Autere, S. Mehravar, A. Lombardo, R. A. Norwood, T. Hasan, N. Peyghambarian, H. Lipsanen, K. Kieu, A. C. Ferrari, M. Polini, Z. Sun, *Nat. Commun.* **2017**, 8, 893.

[9] C. Torres-Torres, N. Perea-López, A. L. Elías, H. R. Gutiérrez, D. A. Cullen, A. Berkdemir, F. López-Urías, H. Terrones, M. Terrones, *2D Mater.* **2016**, 3, 21005.

[10] R. I Woodward, R. T. Murray, C. F. Phelan, R. E. P. de Oliveira, T. H. Runcorn, E. J. R. Kelleher, S. Li,

E. C. de Oliveira, G. J. M. Fechine, G. Eda, C. J. S. de Matos, *2D Mater.* **2016**, 4, 11006.

[11] L. Karvonen, A. Säynätjoki, M. J Huttunen, A. Autere, B. Amirsolaimani, R. A. Norwood, N. Peyghambarian, H. Lipsanen, G. Eda, K. Kieu, Z. Sun, *Nat. Commun.* **2017**, 8, 15714.

[12] H. G. Rosa, Y. W. Ho, I. Verzhbitskiy, M. J. F. L. Rodrigues, T. Taniguchi, K. Watanabe, G. Eda, V. M. Pereira, J. C. V. Gomes, *Sci Rep* **2018**, 8, 10035.

[13] A. S. Sarkar, E. Stratakis, *Adv. Sci.* **2020**, 7, 2001655.

[14] F. Xia, H. Wang, J. C. M. Hwang, A. H. C. Neto, L. Yang, *Nat. Rev. Phys.* **2019**, 1, 306.

[15] L. Li, W. Han, L. Pi, P. Niu, J. Han, C. Wang, B. Su, H. Li, J. Xiong, Y. Bando, T. Zhai, *InfoMat.* **2019**, 1, 54-73.

[16] L. C. Gomes, A. Carvalho, *Physical Review B* **2015**, 92, 085406.

[17] H. Liu, A. T. Neal, Z. Zhu, Z. Luo, X. Xu, D. Tománek, P. D. Ye, *ACS Nano* **2014**, 8, 4033-4041.

[18] A. Carvalho, M. Wang, X. Zhu, A. S. Rodin, H. Su, A. H. C. Neto, *Nat Rev Mater* **2016**, 1, 16061.

[19] Z. Tian, C. Guo, M. Zhao, R. Li, J. Xue, *ACS Nano* **2017**, 11, 2219.

[20] Y. Yang, S.-C. Liu, Y. Wang, M. Long, C.-M. Dai, S. Chen, B. Zhang, Z. Sun, Z. Sun, C. Hu, S. Zhang, L. Tong, G. Zhang, D.-J. Xue, J.-S. Hu, *Adv. Opt. Mater.* **2019**, 7, 1801311.

[21] H. Yuan, X. Liu, F. Afshinmanesh, W. Li, G. Xu, J. Sun, B. Lian, A. G. Curto, G. Ye, Y. Hikita, Z. Shen, S.-C. Zhang, X. Chen, M. Brongersma, H. Y. Hwang, Y. Cui, *Nat. Nanotechnol.* **2015**, 10, 707.

[22] M. Wu, X. C. Zeng, *Nano Lett.* **2016**, 16, 3236-3241.

[23] H. Wang, X. Qian, *2D Mater.* **2017**, 4, 015042.

[24] N. Higashitarumizu, H. Kawamoto, C.-J. Lee, B.-H. Lin, F.-H. Chu, I. Yonemori, T. Nishimura, K. Wakabayashi, W.-H. Chang, K. Nagashio, *Nat. Commun.* **2020**, 11, 2428.

[25] S. Lin, A. Carvalho, S. Yan, R. Li, S. Kim, A. Rodin, L. Carvalho, E. M. Chan, X. Wang, A. H. C. Neto, J. Yao, *Nat. Commun.* **2018**, 9, 1455.

[26] C. Chen, X. Chen, Y. Shao, B. Deng, Q. Guo, C. Ma, F. Xia, *ACS Photonics* **2018**, 5, 3814-3819.

[27] H. Wang, X. Qian, *Nano Lett.* **2017**, 17, 5027.

[28] S. R. Panday, B. M. Fregoso, *J. Phys.: Condens. Matter* **2017**, 29, 43LT01.

[29] M. Zhu, M. Zhong, X. Guo, Y. Wang, Z. Chen, H. Huang, J. He, C. Su, K. P. Loh, *Adv. Optical Mater.* **2021**, 9, 2101200.

[30] G. M. Maragkakis, S. Psilodimitrakopoulos, L. Mouchliadis, A. S. Sarkar, A. Lemonis, G. Kioseoglou, E. Stratakis, *Adv. Optical Mater.* **2022**, 10, 2270038.

[31] R. Moqbel, Y.-R. Chang, Z.-Y. Li, S.-H. Kung, H.-Y. Cheng, C.-C. Lee, K. Nagashio, K.-H. Lin, *2D Mater.* **2023**, 10, 015022.

[32] Z. Xie, F. Zhang, Z. Liang, T. Fan, Z. Li, X. Jiang, H. Chen, J. Li, H. Zhang, *Photonics Research* **2019**, 7, 5.

[33] C. Zhang, H. Ouyang, R. Miao, Y. Sui, H. Hao, Y. Tang, J. You, X. Zheng, Z. Xu, X. Cheng, T. Jiang, *Adv. Optical Mater.* **2019**, 7, 1900631.

[34] R. W. Boyd, *Nonlinear Optics*, Academic Press, Elsevier **2020**.

[35] A. Dasgupta, J. Gao, X. Yang, *Laser Photonics Rev.* **2020**, 14, 1900416.

[36] M. J. L. F. Rodrigues, C. J. S. de Matos, Y. W. Ho, H. Peixoto, R. E. P. de Oliveira, H.-Y. Wu, A. H. C. Neto, J. Viana-Gomes, *Adv. Mater.* **2016**, 28, 10693-10700.

[37] A. Autere, C. R. Ryder, A. Säynätjoki, L. Karvonen, B. Amirsolaimani, R. A. Norwood, N. Peyghambarian, K. Kieu, H. Lipsanen, M. C. Hersam, Z. Sun, *J. Phys. Chem. Lett.* **2017**, 8, 1343.

[38] N. Youngblood, R. Peng, A. Nemilentsau, T. Low, M. Li, *ACS Photonics* **2017**, 4, 1, 8–14.

[39] H. Sar, J. Gao, X. Yang, *Sci Rep* **2021**, 11, 6372.

[40] H. Sar, J. Gao, X. Yang, *Sci Rep* **2020**, 10, 14282.

[41] R. P. N. Tripathi, X. Yang, J. Gao, *Opt. Express* **2022**, 30, 22661-22670.

[42] Q. Cui, R. A. Muniz, J. E. Sipe, H. Zhao, *Phys. Rev. B* **2017**, 95, 165406.

# Chapter 2 – Imaging the crystal orientation of 2D transition metal dichalcogenides using polarization-resolved second-harmonic generation


## Abstract

We use laser-scanning nonlinear imaging microscopy in atomically thin TMDs to reveal information on the crystalline orientation distribution, within the 2D lattice. In particular, we perform P-SHG imaging in a stationary, raster-scanned CVD-grown $WS_2$ flake, in order to obtain with high-precision a spatially resolved map of the orientation of its main crystallographic axis (armchair orientation). At the same time, by fitting the experimental P-SHG images of sub-micron resolution into a generalized nonlinear model, we are able to determine the armchair orientation for every pixel of the image of the 2D material, with further improved resolution. This pixel-wise mapping of the armchair orientation of 2D $WS_2$ allows us to distinguish between different domains, reveal fine structure, and estimate the crystal orientation variability, which can be used as a unique crystal quality marker over large-areas. The necessity and superiority of a polarization-resolved analysis over intensity-only measurements is experimentally demonstrated, while the advantages of P-SHG over other techniques are analysed and discussed.


## 2.1 Beyond state of the art

In this work, we acquire pixel-by-pixel information about the armchair orientation by measuring the SHG intensity, while rotating the linear polarization of the laser beam. It is revealed that crystal imperfections are creating sharp contrast in the P-SHG image among domains of different crystallographic orientations, e.g. grain boundaries or defected regions. Such sensitivity enables detailed mapping of the various crystallographic orientations over large areas, providing invaluable information on crystal structure, which is shown to be unattainable with traditional, intensity-only SHG imaging.

### 2.1.1 P-SHG as a powerful tool for characterizing 2D materials

The present work further supports the unique capabilities of P-SHG as a method for determining the crystalline integrity of 2D TMDs [1]. First, the crystal characterization can be performed rapidly and in an all-optical manner via a single measurement process. Moreover, it can be applied to both forward and epi detection geometry, allowing the study of samples in their original (even opaque) substrates. Therefore, it is minimally invasive and does not require sample preparation, in contrast to TEM microscopy, which necessitates the transfer of the sample to an electron-permeable TEM-supporting membrane, which is a time-consuming and invasive process.

More important, unlike the SHG intensity-only method used for the determination of the main crystallographic axis by rotation of the sample, in the P-SHG approach, the change of the polarization of the fundamental field allows pixel-by-pixel imaging with ultrahigh resolution that is determined by the pixel size. As a result, the contrast in P-SHG analysis offers a mechanism that provides resolution beyond the optical one, in the ‘polarization space’, enabling to detect changes in the armchair direction with accuracy ~$0.5^0$.

Another advantage of raster-scanning P-SHG over traditional SHG imaging is that it allows the mapping of a large area, and therefore is a unique tool for the characterization of grain boundaries and other extended defects in polycrystalline structures. Finally, incorporation of a P-SHG setup into a CVD chamber could potentially lead to an in situ, real-time evaluation of crystal quality (in analogy with RHEED in molecular beam epitaxy), which would signify an important advance towards the production of defect-free 2D materials. A comparison between P-SHG with traditional SHG is also shown in the following table (**Table 2.1**).

**Table 2.1**. Comparison of P-SHG with traditional SHG methods.

| | SHG | P-SHG |
|---|---|---|
| Detection of armchair orientation | ✓ | ✓ |
| Pixel-by-pixel mapping of the armchair orientation over large areas | X | ✓ |
| Application as crystal quality marker over large crystal regions | X | ✓ |
| Identification of the boundaries between regions of different crystal orientations | X | ✓ |

## 2.2 Results and discussion

### 2.2.1 Theoretical formulation for P-SHG in TMDs

### Nonlinear optical response of 2D TMDs

The induced nonlinear polarization that leads to SHG in crystals, $P_i(2\omega)=\varepsilon_0\sum_{j,k}\chi^{(2)}_{ijk}E_j(\omega)E_k(\omega)$, is governed by the second-order susceptibility tensor $\chi^{(2)}_{ijk}$, a third-rank tensor that describes the crystal symmetry, and is nonzero for non-centrosymmetric media [2].

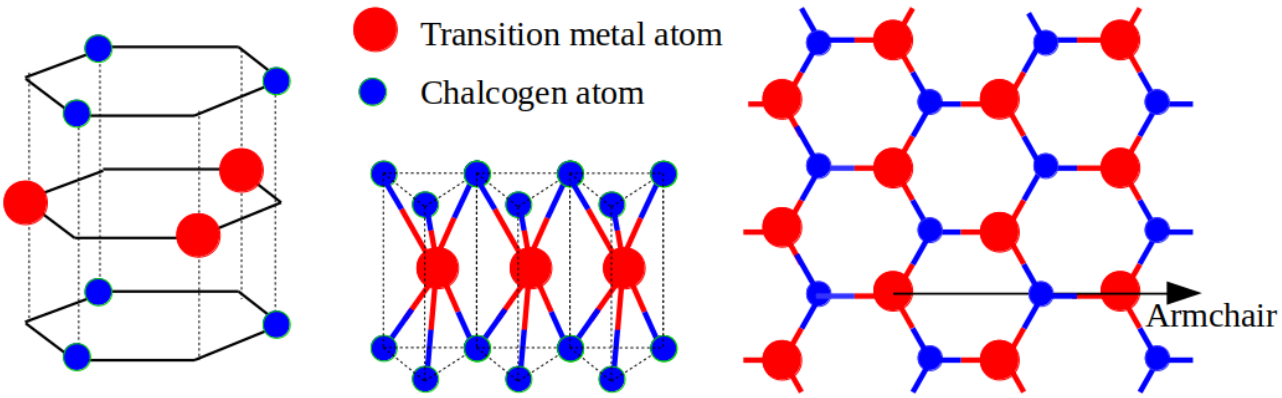


**Figure 2.1.** Schematic representation of the structure of 2D TMDs, containing three sublattices, with a plane of metal atoms being hexagonally packed between two planes of chalgogen atoms.

The structure of monolayer $MX_2$, shown in **Fig. 2.1**, comprises three sublattices: an atomic plane of metal atoms, with threefold coordinate symmetry, is hexagonally packed between two trigonal planes of chalgogen atoms. $WS_2$ crystals with 2H stacking order belong to $D_{6h}$ symmetry group and are inversion symmetric, for an even number of layers. However, for odd layer number, the symmetry is broken and the crystal belongs to the $D_{3h}$ space group. Under this symmetry, $\chi^{(2)}$ has four nonzero elements, namely $\chi^{(2)}_{xxx} = -\chi^{(2)}_{xyy} = -\chi^{(2)}_{yyx} = -\chi^{(2)}_{yxy}$, where x, y, z denote the crystalline coordinates, with *x* being the mirror symmetry axis (the armchair direction), and y the axis along which the mirror symmetry is broken (the zigzag direction). The finite second-order optical susceptibility, along with the atomic thickness of 2D TMDs which ensures phase matching, suggest strong optical SHG, which, indeed, has been observed and studied [1, 3-10]. For the case of TMDs with $D_{3h}$ point symmetry, including the monolayers, the SHG equation can be written in matrix form as

$$\begin{pmatrix} P_x^{2\omega} \\ P_y^{2\omega} \\ P_z^{2\omega} \end{pmatrix} = \varepsilon_0 \chi^{(2)}_{xxx} \begin{pmatrix} 1 & -1 & 0 & 0 & 0 & 0 \\ 0 & 0 & 0 & 0 & 0 & -1 \\ 0 & 0 & 0 & 0 & 0 & 0 \end{pmatrix} \begin{pmatrix} E_x^{\omega} E_x^{\omega} \\ E_y^{\omega} E_y^{\omega} \\ E_z^{\omega} E_z^{\omega} \\ 2E_y^{\omega} E_z^{\omega} \\ 2E_x^{\omega} E_z^{\omega} \\ 2E_x^{\omega} E_y^{\omega} \end{pmatrix} \quad (1)$$

## Methodology for measuring 2D TMD crystal orientation using P-SHG

The adopted experimental configuration, presented in **Fig. 2.2**, consists of two coordinate systems: the laboratory X-Y-Z, and the crystalline x-y-z, with Z≡z, and x parallel to the armchair orientation and at angle θ from X. The fundamental field is propagating along Z axis, normally incident on the crystal, and it is linearly polarized along the sample plane, at an angle $\varphi$ with respect to X laboratory axis. By rotating the zero-order half-waveplate, we rotate the orientation of the excitation linear polarization at the sample plane, and we record the sample-produced SHG as function of φ. Before reaching the detector, SHG is passing through a linear polarizer, at constant angle ζ from X.

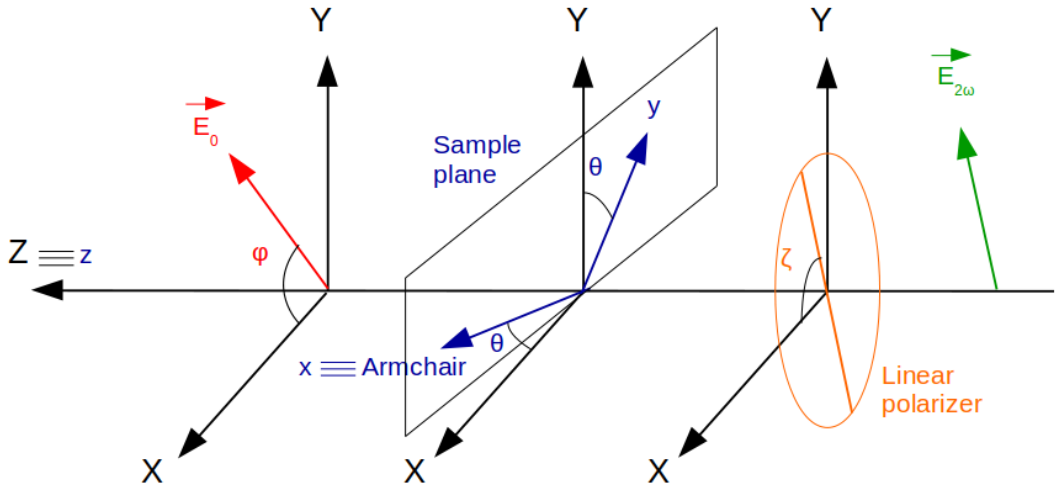


**Figure 2.2.** The experimental configuration, showing the laboratory X-Y-Z, and the crystalline x-y-z coordinate systems. Angles φ, θ, and ζ describe, respectively, the orientation of the rotating fundamental linear polarization, crystal armchair, and linear polarizer, with respect to X laboratory axis.

In order to address the laser propagation, we employ the Jones formalism. The excitation polarization after the retarder plate may be expressed as the Jones vector $\begin{pmatrix} cos\varphi \\ sin\varphi \end{pmatrix}$, where the amplitude of the electric field is normalized to unity. Expression of the Jones vector in crystalline coordinates is achieved by multiplication with the rotation matrix $\begin{pmatrix} cos\theta & sin\theta \\ -sin\theta & cos\theta \end{pmatrix}$, containing the armchair angle θ. The result for the nonlinear polarization in crystalline coordinates is $\begin{pmatrix} P_x^{2\omega} \\ P_y^{2\omega} \end{pmatrix} = \varepsilon_0 \chi_{xxx}^{(2)} \begin{pmatrix} \cos[2(\theta-\varphi)] \\ \sin[2(\theta-\varphi)] \end{pmatrix}$, or by rotating back to lab coordinates, $\begin{pmatrix} P_x^{2\omega} \\ P_y^{2\omega} \end{pmatrix} = \varepsilon_0 \chi_{xxx}^{(2)} \begin{pmatrix} \cos(3\theta-2\varphi) \\ \sin(3\theta-2\varphi) \end{pmatrix}$. Finally, in order to account for the polarizer, the polarization vector of the detected SHG signal is found after multiplying with the Jones matrix $\begin{pmatrix} \cos^2\zeta & cos\zeta \cdot sin\zeta \\ cos\zeta \cdot sin\zeta & \sin^2\zeta \end{pmatrix}$. The final SHG intensity recorded by the detector can be expressed as

$$I_{SHG} = A \cdot \cos^2(\zeta - 3\theta + 2\varphi) \quad (2)$$

where A is a multiplication factor depending on $\chi^{(2)}$ and the excitation amplitude.

For ζ=0 and ζ=π/2, i.e. polarizer paraller to X and Y laboratory axis, respectively, the SHG intensity reads [1]

$$I_X = A \cdot \cos^2(3\theta - 2\varphi) \quad (3)$$

and

$$I_Y = A \cdot \sin^2(3\theta - 2\varphi) \quad (4)$$

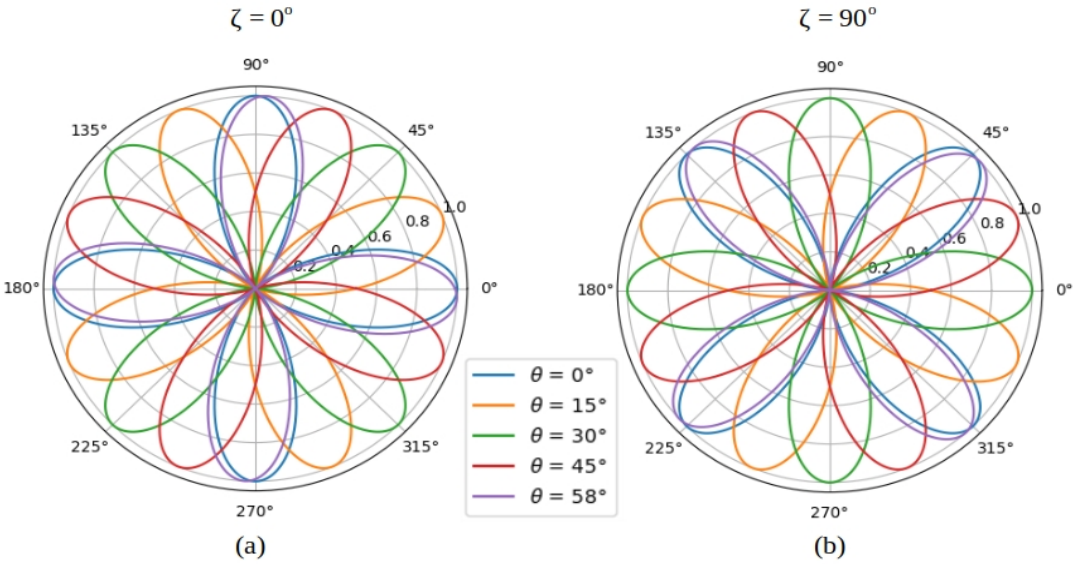


**Figure 2.3.** Simulated P-SHG modulation presented in polar diagrams, as function of the linear polarization orientation φ, with φ ϵ [$1^0$, $360^0$], for fixed polarizer at angle (**a**) ζ=$0^0$ and (**b**) ζ=$90^0$. The orientation of the four-fold pattern rotates for different crystal armchair directions θ.

These equations summarize the polarization-dependent SHG modulation from 2D TMDs, for the experimental configuration presented here. This modulation is plotted in polar diagrams in **Fig. 2.3** as a function of φ, with φ ϵϵ [$1^0$, $360^0$], for fixed polarizer (ζ=$0^0$ and ζ=$90^0$). As may be seen, a four-fold pattern (four-leave rose) is obtained, which rotates for different values of crystal armchair orientation, θ. Given that each θ corresponds to a characteristic polar modulation of specific orientation, we can calculate θ for every pixel of an area image, by fitting pixel-by-pixel the P-SHG experimental data to Eq. 2. It should be noted that, since there exist three equivalent armchair directions in each hexagon of the crystal lattice (threefold rotational symmetry), one can determine this direction modulo 60°, constraining θ ∈ϵ [0°–60°], while sampling φ in [0°–90°] is adequate to extract all possible armchair orientations. The armchair angle could also be determined by combining Eq. 3, 4, as

$$\theta = \frac{1}{3}\left(2\varphi + \tan^{-1}\sqrt{\frac{I_Y}{I_X}}\right) \quad (5)$$

## Estimation of fitting error

As we discussed, we can experimentally calculate the armchair angle θ, by performing fitting to the P-SHG experimental data with Eq. 3. These experimental results will be characterized by a quality of fitting $R^2$, showing how good is the consistency between the experimental data and the theoretical fitting. Here we attempt to correlate this quality of fitting with the error characterizing our fitting results.

In order to do this, we have created "ideal" P-SHG data to which we have applied Gaussian noise. By increasing the noise, we reduce the quality of fitting $R^2$ (**Fig. 2.4**). **Fig. 2.5** presents the error of the fitting procedure, i.e., the actual armchair angle minus the fitted armchair angle, as function of the quality of fitting $R^2$. As may be seen, for $R^2 \geq 90\,\%$, the error is less than $0.4^0$, and for $R^2 \geq 60\,\%$, the error is less than $1^0$, supporting the accuracy of our approach.

For a more advanced methodology of quantifying the above error, see the Supporting Information of our submitted manuscript: Maragkakis G. M. et al., "Anisotropic Third Harmonic Generation in Two-Dimensional Tin Sulfide". More specifically, in that work, in the "ideal" P-THG values, we have applied 1000 realizations of Poisson noise, and then performed the same simultaneous fitting procedure adopted to fit the real experimental data, for each realization. Then as the smallest detectable change in the AC angle, we have utilized the standard deviation value, $\sigma_\theta$, that resulted from the 1000 realizations of Poisson noise.

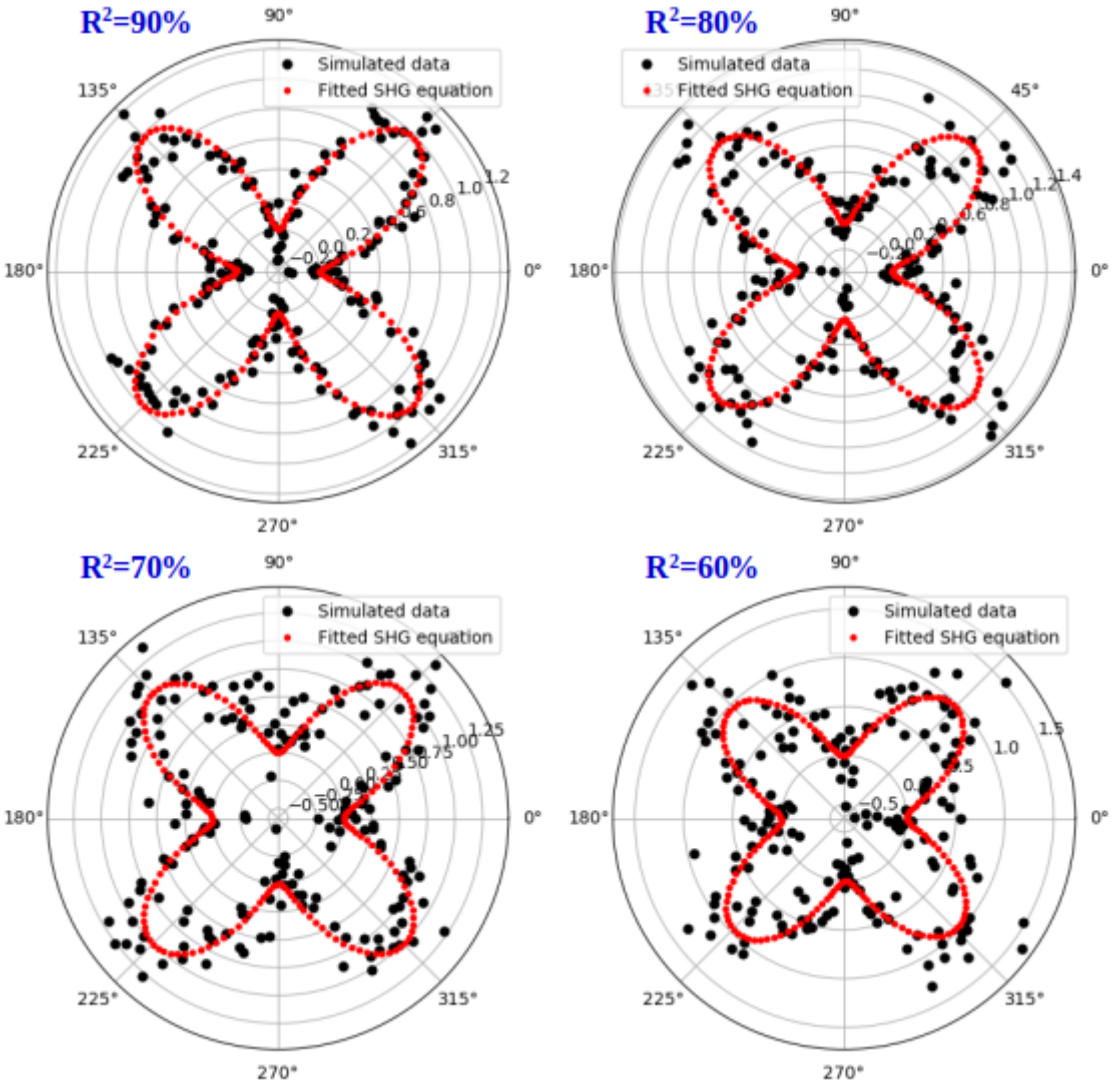


**Figure 2.4.** Fitting with Eq. 3 (red line) to simulated data (black dots) of P-SHG in a TMD. By increasing the noise in the simulated data, the quality of fitting $R^2$ is reduced.

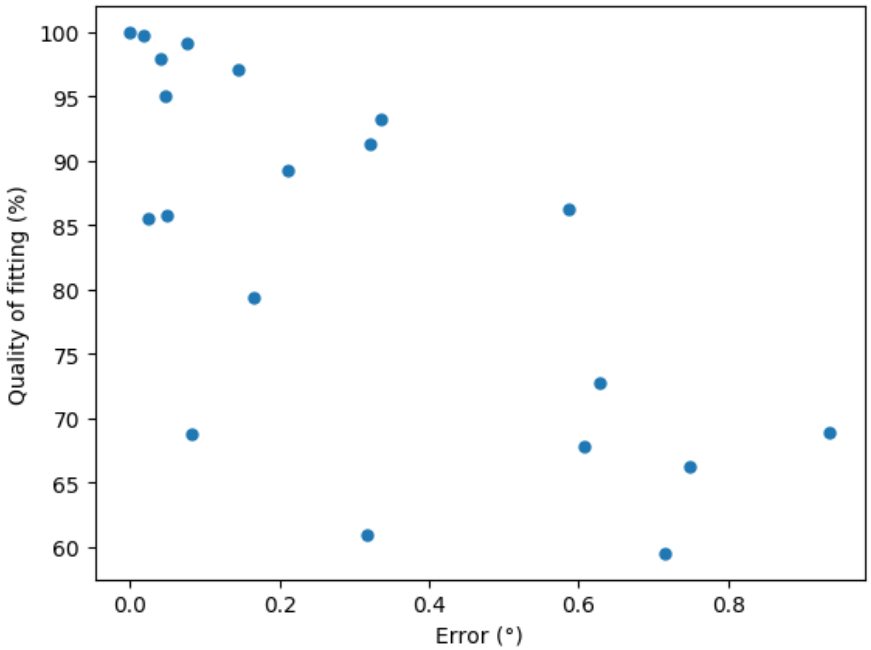

**Figure 2.5.** The error of the fitting procedure, i.e., the actual AC angle minus the fitted AC angle, as function of the quality of fitting $R^2$.

## Extending the consideration for multi-layer structures

The approach we described applies to crystals of $D_{3h}$ symmetry, where the dipoles created by the incident field act as surface array antennas radiating at double frequency and thus producing SHG signals. In the case of multi-layer systems, the SH fields from each layer interfere before detection, and can be treated as a vector superposition, giving:

$$\vec{E}_S = \sum_{i=1}^{N} \vec{E}_i \quad (6)$$

where N is the total number of layers, and $\vec{E}_i$ can be obtained by

$$\vec{E}_i = A_i \cdot \cos(\zeta - 3\theta_i + 2\varphi) \cdot (cos\zeta \cdot \hat{X} + sin\zeta \cdot \hat{Y}) \quad (7)$$

For $\zeta=0^0$, we get the simplified form $\vec{E}_i = A_i \cdot \cos(3\theta_i - 2\varphi) \cdot \hat{X}$.

The total intensity recorded by the detector can then be expressed as

$$I_S^{PMT} = |\vec{E}_S|^2 = \left|\sum_{i=1}^{N} \vec{E}_i\right|^2 = \sum_{i=1}^{N} I_i + \sum_{\substack{i,j \\ (i \neq j)}}^{N} \sqrt{I_i I_j} \cdot \cos(3\delta_{ij}) \quad (8)$$

with $I_i$ the intensity of the *i*th layer, and $\delta_{ij}$ the twist angle between layers *i* and *j*, $\delta_{ij} = \theta_i - \theta_j$. For *N=2*, the SHG intensity of the bilayer is given by [8]

$$I_{BL} = I_1 + I_2 + 2\sqrt{I_1 I_2} \cdot \cos(3\delta) \quad (9)$$

Furthermore, for layers of equal intensity ($I_1 = I_2 = I_{ML}$) at zero twist angle ($\delta = 0$), we obtain, $I_{BL} = 4I_{ML}$, i.e. the well-known result that SHG intensity scales quadratically with layer number, while for $\delta = \pi/6$, we have $I_{BL} = 2I_{ML}$.If the intensities are measured, the twist angle could also be estimated from (9), as [8]

$$\delta = \frac{1}{3} \cdot \cos^{-1}\left(\frac{I_{BL} - I_1 - I_2}{2\sqrt{I_1 I_2}}\right) \quad (10)$$

or

$$\delta = \frac{1}{3} \cdot \cos^{-1}\left(\frac{I_{BL}}{2I_{ML}} - 1\right) \quad (11)$$

for the case of $I_1 = I_2 = I_{ML}$.

### 2.2.2 Experimental results of P-SHG in TMDs

Typical experimental configurations investigating the main crystallographic orientation of 2D TMDs are based on the rotation of the sample (e.g. [3-6]). In such experiments, the parallel and perpendicular polarization component of the second harmonic field is measured, with dependency $I_X \sim \cos^2(3\theta)$ and $I_Y \sim \sin^2(3\theta)$, respectively, where θ is the angle between the armchair direction and the polarization orientation of the incident field. This results in a six-leave rose polar diagram.

In contrast, here, we rotate the orientation of the linear polarization of the excitation, measuring P-SHG in stationary raster-scanned crystals, allowing pixel-wise mapping of the armchair orientation. For this purpose, we define angles θ and φ, which characterize the armchair direction and fundamental field polarization, respectively, both with respect to the X laboratory axis (see **Fig 2.2**). In our approach, high angular accuracy was realized by using a step of only 1° for the excitation polarization orientation φ. In **Fig. 2.6**, we present P-SHG images of raster-scanned $WS_2$, for $\varphi \in [0°–360°]$ with step 40° for each consecutive image, and the linear polarizer at constant angle, ζ=0°. Rotation of the fundamental field is found to switch on and off the P-SHG signal from the triangular flake according to its relative armchair crystal orientation θ.

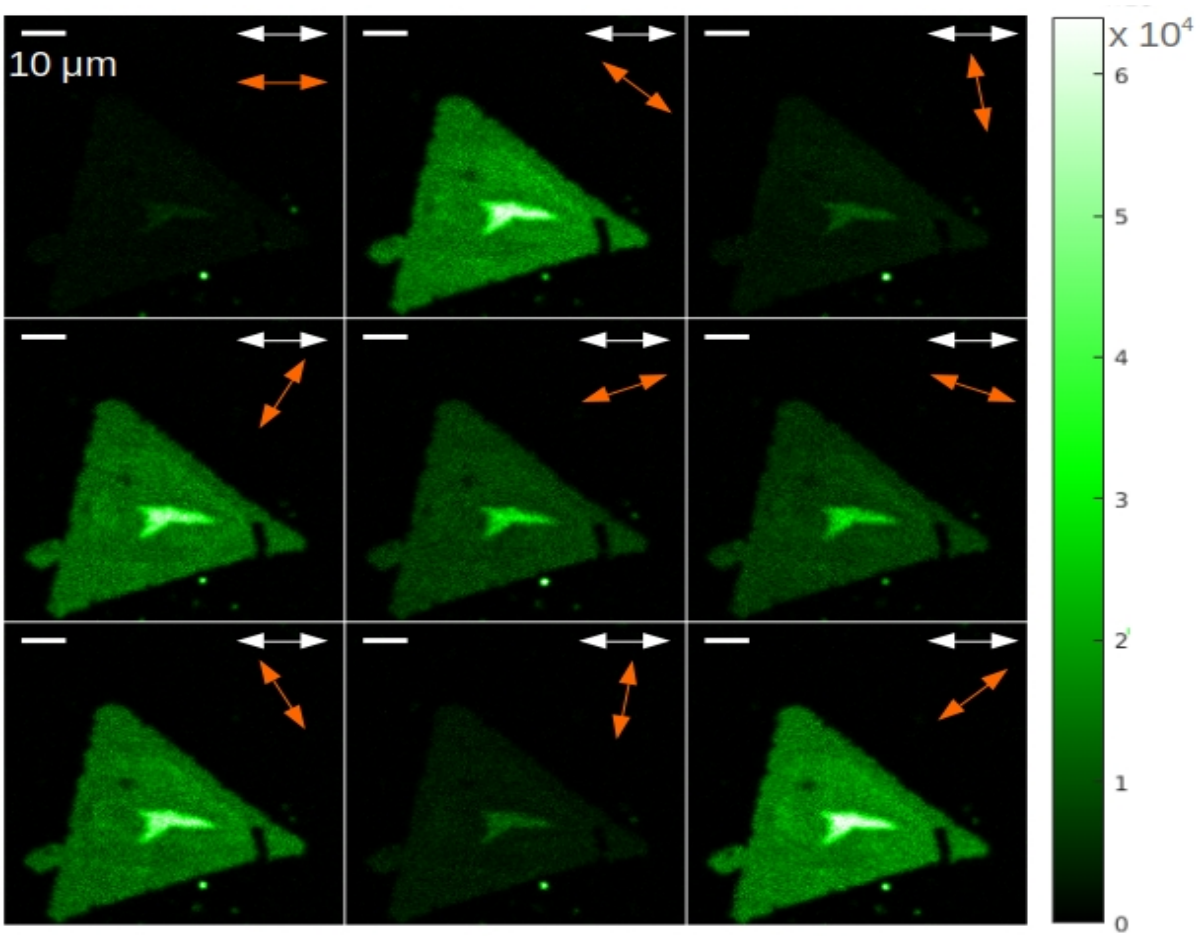


**Figure 2.6.** Snapshots of experimental P-SHG images of a $WS_2$ flake, CVD-grown on a sapphire substrate. The white double arrow shows the constant angle, ζ=0°, of the linear polarizer, while the orange double arrow shows the rotating angle, φ, of the excitation linear polarization. Here, the rotation of φ ∈ [0°–360°] with step 40°, clearly shows the switching on and off of the SHG signal.

By summing up the P-SHG images for φ ∈ [0°–90°] with step 1°, we obtain **Fig. 2.7a**, showing the total SHG signal collected. In contrast to **Fig. 2.6**, where the P-SHG signal is changing with respect to the orientation φ of the excitation linear polarization, the sum of the P-SHG images is no longer polarization-dependent. Since the dependence on the armchair crystal angle θ is lost, any differences in intensity observed in **Fig. 2.7a** can now be attributed only to crystal structure variations, most probably material thickness or layer stacking. For example, it is known that larger number N of 3R-stacked monolayers generates SHG of higher intensity [10], which depends quadratically on the number of layers.

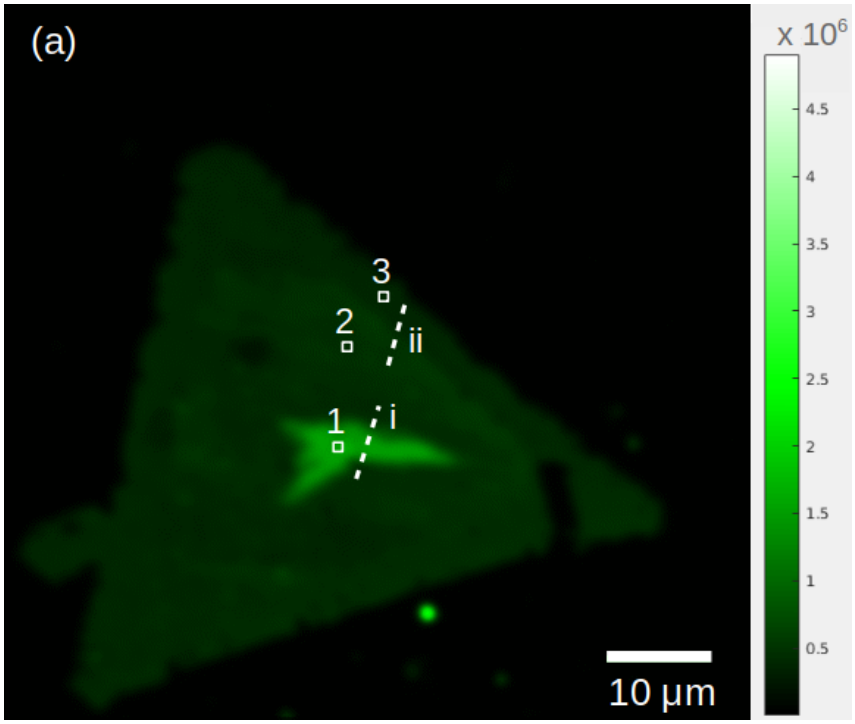
(a)
x 10^6
4.5
4
3.5
3
2.5
2
1.5
1
0.5
3
2
ii
1
i
10 μm

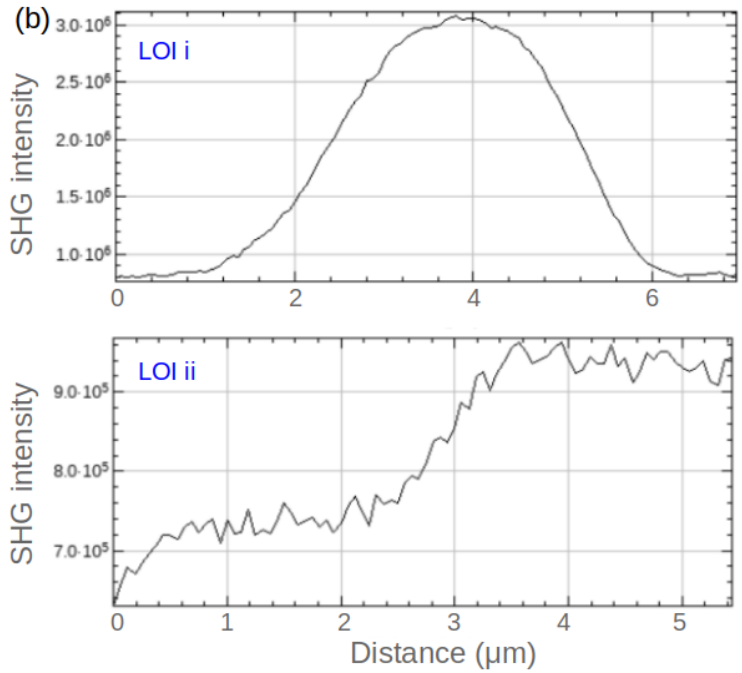
(b)
LOI i
SHG intensity
3.0·10^6
2.5·10^6
2.0·10^6
1.5·10^6
1.0·10^6
0
2
4
6
LOI ii
SHG intensity
9.0·10^5
8.0·10^5
7.0·10^5
0
1
2
3
4
5
Distance (μm)

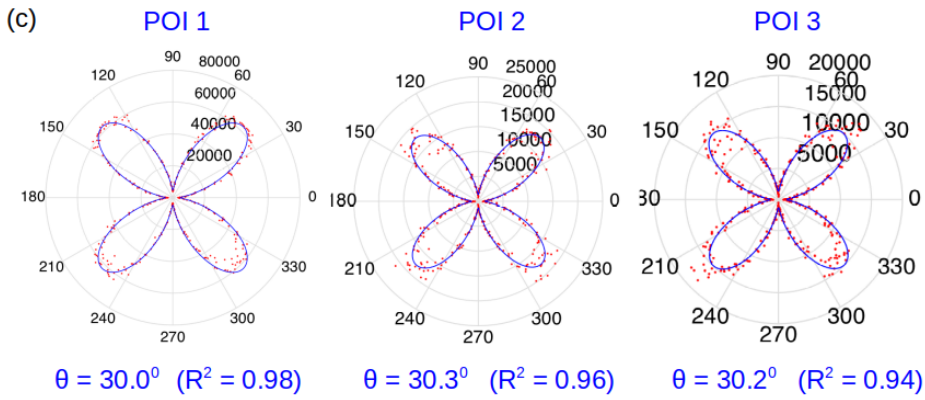
(c)
POI 1
POI 2
POI 3
θ = 30.0^0 (R^2 = 0.98)
θ = 30.3^0 (R^2 = 0.96)
θ = 30.2^0 (R^2 = 0.94)

**Figure 2.7. a**) Integration of the experimentally detected P-SHG intensity from the $WS_2$ island, for $\varphi \in [0°–90°]$ with step 1°, presented upon marking three points of interest (POIs) and two lines of interest (LOIs), for further analysis. The POIs are actually single pixels of the 1200x1200 original image, magnified here, for illustration purposes. **b**) Intensity profile of the experimental P-SHG modulation presented in (a), along the LOIs shown there. As may be seen for LOI i, the intensity in the central, brighter area is magnified by a factor of ~4, which suggests the presence of second layer [8]. (**c**) Polar diagrams of the experimental P-SHG modulation for $\varphi \in [0°–360°]$ with step 1°, for the POIs illustrated in (a). We show with red color the raw data, and with blue the fitting using Eq. 3. We also present the retrieved values of the armchair orientation θ and the quality of fitting $R^{2.}$

Aiming to experimentally explore these considerations, we present the intensity profile of detected SHG intensity (**Fig. 2.7b**), along two LOIs shown in **Fig. 2.7a**. As can be seen, in the case of LOI i, the intensity in the central, brighter area of the triangle is magnified by a factor of ~4, which suggests the presence of a second layer at twist angle $0^0$. Let us now examine this assumption based on our P-SHG analysis. We focus on the specific pixels of interest, POIs 1 and 2, shown in **Fig. 2.7a**, which belong to different intensity regions. By plotting the experimental P-SHG data in a polar diagram, for $\varphi \in [0°–360°]$ with step 1°, and by fitting using Eq. 3, we can determine the armchair angle θ, for each pixel. Indeed, in **Fig. 2.7c**, we present the raw data (in red) and fitted line (in blue), that correspond to the three POIs, along with the retrieved armchair angles and quality of fitting $R^2$. As can be seen, POIs 1-3, correspond to almost identical values of θ, and thus the P-SHG analysis further supports the presence of a second layer, at the central, brighter area, vertically stacked at twist angle $0^0$, as was suggested by intensity-only SHG measurements.

For the case, however, of LOI ii, the intensity-only SHG measurements, considered alone, could give misleading results. More specifically, the intensity profile of LOI ii (**Fig 2.7b**), shows a signal change of ~1.3. By using Eq. 11, this corresponds to a twist angle of $\delta=37^0$. Nevertheless, by performing P-SHG analysis, we find a similar θ for the POIs 2 and 3, and therefore $\delta\sim0^0$. A possible explanation for the intensity variation between POIs 2 and 3 might be the change in stacking sequence [10]. The above example indicates that SHG intensity-only measurements are insufficient for an all-optical determination of the twist angle between layers of different armchair orientations, and therefore a polarization-dependent analysis is necessary.

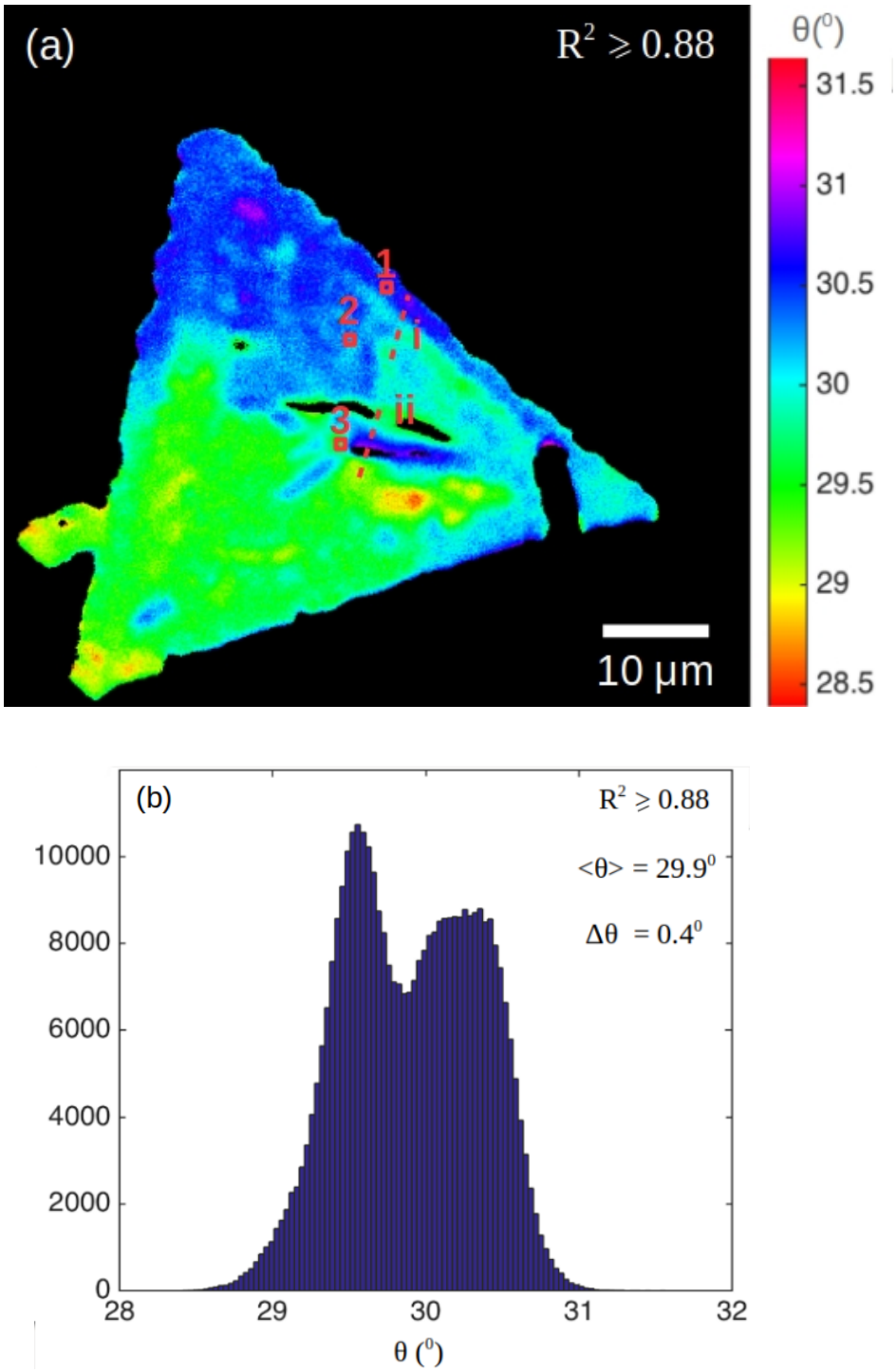


**Figure 2.8.** Mapping in **a**) 2D diagram and **b**) histogram of the armchair orientation distribution of the $WS_2$ flake, based on the pixel-by-pixel fitting ($R^2 \geq 0.88$) of Eq. 3 on the experimental P-SHG modulation for $\varphi \in [0°–360°]$ with step 1°. Significant color changes in the map, or equivalently, large standard deviation ($\Delta\theta$) of the histogram, denote inhomogeneity in either crystalline orientation, material thickness, or layer stacking.

By repeating this analysis for every pixel of the P-SHG image, for φ ∈ [0°–360°] with step 1°, we obtain the color map presented in **Fig. 2.8a**, showing the distribution of armchair directions across the $WS_2$ TMD flake, and the corresponding histogram (**Fig. 2.8b**). Color variation in such a map, quantified by the standard deviation of the respective histogram, denotes absence of homogeneity in crystalline properties, supporting the application-suitability of the presented technique as a crystal quality marker.

## 2.3 Methods

### 2.3.1 Experimental setup for measuring P-SHG in stationary raster-scanned samples

The experimental setup of our laser-scanning microscope is schematically shown in **Fig. 2.9**. It is based on a diode-pumped Yb:KGW fs oscillator (1.2 W, 1030 nm, 70–90 fs, 76 MHz, Pharos-SP, Light Conversion, Vilnius, Lithuania), a custom-built inverted microscope (Axio Observer Z1, Carl Zeiss, Jena, Germany), and a pair of silver-coated galvanometric mirrors (6215H, Cambridge Technology, Bedford, MA, USA). First, the beam passes through a zero-order half-wave retardation plate (QWPO-1030-10-2, CVI Laser), with which the orientation of the linear polarization of the excitation beam at the sample plane, can be rotated using a motorized rotation stage (M-060.DG, Physik Instrumente, Karlsruhe, Germany). A pair of achromatic doublet lenses, forming a telescope, suitably expands the laser spot in order to fill the back aperture of the objective lens, while the galvanometric mirrors direct the scanning beam towards the inverted microscope and its motorized turret box, just below the objective (Plan-Apochromat × 40/1.3NA, Carl Zeiss).

At the microscope turret box, we have the choice of using either a silver-coated mirror (PFR10-P01, ThorLabs, Newton, NJ, USA), or a short-pass dichroic mirror (DMSP805R, ThorLabs), both at 45°, depending on whether we detect the signal in the forward direction (silver-coated), or the backwards or both simultaneously (dichroic). P-SHG measurements in the forward direction ensure that our setup is insensitive to the different orientations of laser polarization, given the silver coating of all mirrors (PF 10-03-P01, ThorLabs), including the galvanometric. It is important to note, however, that our setup also permits P-SHG collection in the backward direction, allowing the study of samples in their original substrates, confirming the minimally invasive character of the technique. It also permits simultaneous imaging of P-SHG and (back reflected) two-photon-

absorption-induced photoluminescence (TPL), in the forward and epi direction, respectively, by using suitable filters, the same objective, and a second detector.

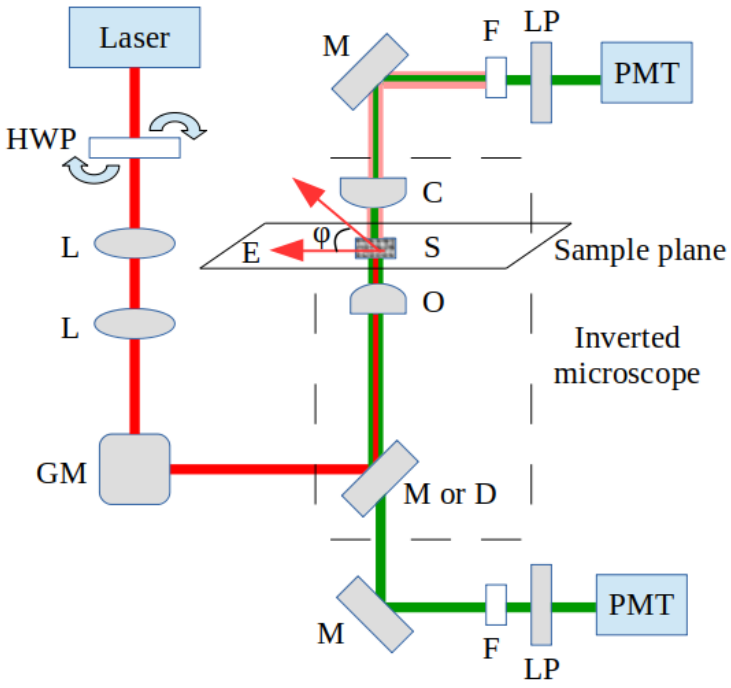


**Figure 2.9.** Schematic representation of the experimental setup, also adopted in [1], allowing high-resolution P-SHG measurements in stationary, raster-scanned samples. Abbreviations, as met by the laser fundamental pulse: HWP: zero-order half-waveplate, L: lens, GM: galvanometric mirrors, M: mirror, D: dichroic, O: objective, S: sample, C: condenser, F: filters, LP: linear polarizer, PMT: photomultiplier tube. The linear polarization of the excitation electric field (E) starts horizontal in the sample plane and is rotated clockwise with an angle φ (see also **Fig. 2.2**).

For the experimental results presented here, we work in the forward detection geometry. The beam, reflected by the silver-coated mirror, is tightly focused by the microscope objective lens to a diffraction-limited spot onto the sample, which produces SHG. This signal is collected by a high numerical aperture condenser lens (achromatic-aplanatic, 1.4NA, Carl Zeiss), and then filtered by a short-pass filter (FF01-720/SP, Semrock, Rochester, NY, USA), to remove residual from the fundamental pulse, as well as a narrow bandpass filter (FF01-514/3, Semrock), centered at the second harmonic wavelength, to separate it from TPL. Finally, the beam passes through a rotating film polarizer (LPVIS100-MP, ThorLabs), and is detected by a photomultiplier tube (PMT) (H9305-04, Hamamatsu, Hizuoka, Japan).

The galvanometric mirrors and the PMTs are connected to a connector block (BNC-2110, National Instruments, Austin, TX, USA), which is interfaced to a PC through a DAQ (PCI 6259, National Instruments). Coordination of PMT recordings with the galvanometric mirrors for the image formation, as well as the movements of all the microscope motors, is carried out using LabView (National Instruments) software.

### 2.3.2 Samples

The $WS_2$ sample was grown by the low-pressure CVD method on a c-cut (0001) sapphire substrate (2D semiconductors). It was characterized using micro-Raman spectroscopy with a 473 nm excitation wavelength.

## References


[1] Psilodimitrakopoulos S, Mouchliadis L, Paradisanos I, Lemonis A, Kioseoglou G, Stratakis E. Ultrahigh-resolution Nonlinear Optical Imaging of the Armchair Orientation in 2D Transition Metal Dichalcogenides. Light. Light: Sci Appl **7**, 18005 (2018)

[2] Boyd RW. Nonlinear Optics. 3rd edn. San Diego: Academic Press (2008).

[3] Kumar N, Najmaei S, Cui QN, Ceballos F, Ajayan PM et al. Second harmonic microscopy of monolayer $MoS_2$. Phys Rev B **87**, 161403 (2013).

[4] Malard LM, Alencar TV, Barboza APM, Mak KF, de Paula AM. Observation of intense second harmonic generation from $MoS_2$ atomic crystals. Phys Rev B **87**, 201401 (2013).

[5] Li YL, Rao Y, Mak KF, You YM, Wang SY et al. Probing symmetry properties of few-layer $MoS_2$ and h-BN by optical second-harmonic generation. Nano Lett **13**, 3329–3333 (2013).

[6] Yin X, Ye Z, Chenet DA, Ye Y, O'Brien K et al. Edge nonlinear optics on a $MoS_2$ atomic monolayer. Science **344**, 488-490 (2014)

[7] Clark DJ, Senthilkumar V, Le CT, Weerawarne DL, Shim B et al. Strong optical nonlinearity of CVD-grown MoS 2 monolayer as probed by wavelength-dependent second-harmonic generation. Phys Rev B **90**, 121409 (2014).

[8] Hsu WT, Zhao ZA, Li LJ, Chen CH, Chiu MH et al. Second harmonic generation from artificially stacked transition metal dichalcogenide twisted bilayers. ACS Nano **8**, 2951–2958 (2014).

[9] Wang Y, Xiao J, Yang S, Wang Y, Zhang X. Second harmonic generation spectroscopy on two-dimensionalmaterials. Opt. Mater. Express **9**(3), 1136–1149 (2019).

[10] Zhao M, Ye Z, Suzuki R, Ye Y, Zhu et al. Atomically phase-matched second-harmonic generation in a 2D crystal. Light Sci. Appl. **5**, e16131 (2016).

# Chapter 3 - Real-time spatially resolved determination of twist angle in transition metal dichalcogenide heterobilayers


## Abstract

2D TMDs offer unique optoelectronic capabilities due to their direct bandgap semiconductor nature in monolayer form. Atomically thin TMDs can be assembled in vertical stacks that are held together by van der Waals forces, enabling interlayer coupling between the layers. This creates new physical properties that depend on the relative orientation (twist angle) between the TMD monolayers. Accurate and fast measurement of the twist angle is therefore of utmost importance for characterizing a 2D TMD heterostructure. Here, we present a nonlinear imaging technique based on second harmonic generation (SHG) microscopy, that enables instantaneous mapping of the twist angle between the two stacked TMD monolayers. By using a polarization beam splitter in the detection path and two detectors measuring two orthogonal SHG polarization components, we acquire with a single-shot measurement the twist angle in a $WS_2/MoS_2$ heterobilayer, in real time. Remarkably, the twist angle is measured directly in the overlapping region based on a SHG interference model. The demonstrated technique offers a powerful tool for the rapid, all-optical and spatially resolved twist angle determination in large-area 2D TMD heterostructures.


## 3.1 Beyond state of the art

In this work, we use SHG microscopy for the real-time and spatially resolved determination of a twist angle in large areas of TMD heterobilayers. In particular, by analyzing the produced SHG signals in two orthogonal directions, we extract, for every point of a large area, the twist angle and the armchair crystal orientation of each individual 2D TMD monolayer constituting a heterobilayer. Remarkably, upon using a polarization beam splitter in the detection path and two detectors, the twist angle can be acquired with a single-shot measurement in real time. This is feasible due to the coherence of SHG signals, enabling a polarization analysis to reveal the armchair orientations of the

layers whose individual SHG signals interfered to produce the detected SHG. The robustness of our methodology lies in performing these polarization measurements directly in the regions of overlapping monolayers. In addition, this approach combined with the adopted laser-scanning imaging, allows the detection of possible local spatial variations of twist angle in large crystal areas, enabling the quantification of crystal quality for emerging TMD applications.

## 3.2 Results and discussion

### 3.2.1 Theoretical formulation

The generated second harmonic signal from a 2D TMD crystal is described by its corresponding second-order optical susceptibility tensor, $\chi^{(2)}_{TMD}$, the value of which dictates the strength of the produced SHG signal. Atomically thin crystals of different atomic constituents exhibit different $\chi^{(2)}_{TMD}$ values and consequently different strengths in their SHG production [1, 2]. For a $TMD_1$ monolayer belonging to $D_{3h}$ point symmetry group, only the following $\chi^{(2)}_{TMD_1}$ tensor elements contribute to the SHG signal: $\chi^{(2)}_{x_1x_1x_1} = -\chi^{(2)}_{x_1y_1y_1} = -\chi^{(2)}_{y_1y_1x_1} = -\chi^{(2)}_{y_1x_1y_1}$, where $x_1$,$y_1$,$z_1$ denote the $TMD_1$ crystal coordinate system, with $x_1$ being along the $TMD_1$ armchair direction (**Fig. 3.1a**).

In our experimental configuration, the excitation laser beam propagates along Z-axis and the $x_1$ armchair direction of $TMD_1$ is at angle $\theta_1$ with respect to *X*-axis (**Fig. 3.1a**). In a heterobilayer structure, a second $TMD_2$ monolayer of different type is stacked above $TMD_1$. This monolayer has different $\chi^{(2)}_{TMD_2}$ and its armchair orientation is lying in $x_2$ direction, at angle $\theta_2$ with respect to *X*-axis (**Fig. 3.1a**). In **Fig. 3.1c** showing a CCD image of a $WS_2/MoS_2$ heterobilayer, one can identify two different types of regions, created by the above stacking, which produce different SHG signals. Specifically, we identify regions where only one of the two TMD monolayers is present, as well as the region where the two monolayers spatially overlap. For the area where only one TMD monolayer (MO) is present, the SHG intensity when rotating the pump linear polarization orientation $\varphi$ and detecting the SHG *parallel* (s) to X-axis, is given by [3]:

$$I^{2\omega}_{s,i(MO)} = \left[A_i \cos\left(3\theta_i - 2\varphi\right)\right]^2 \quad (1)$$

where $A_i = E_0^2 \varepsilon_0 \chi^{(2)}_{x_i x_i x_i}$, $i = 1, 2$, with $\varepsilon_0$ being the dielectric constant and $E_0$ the amplitude of the excitation field. On the other hand, for SHG detection *perpendicular* (p) to X -axis, we obtain:

$$I^{2\omega}_{p,i(MO)} = \left[A_i \sin\left(3\theta_i - 2\varphi\right)\right]^2 \quad (2)$$

We can then conveniently calculate $A_i$ and $\theta_i$ for each individual TMD monolayer, by fitting SHG intensities (from a region with only one TMD present), for different angles $\varphi$, to Eq. (1) or Eq. (2) for the parallel or perpendicular to X-axis SHG detection, respectively [3].

Alternatively, we can also calculate each individual armchair orientation $\theta_i$ by fixing the excitation linear polarization parallel to *X*-axis ($\varphi = 0^o$), then performing two (simultaneous) SHG intensity measurements ($I^{2\omega}_{s(MO)}$ for parallel and $I^{2\omega}_{p(MO)}$ for perpendicular to X-axis SHG detection), from a region with only one $TMD_i$ monolayer present, and finally substituting to the following formula obtained after combining Eq. 1 and Eq. 2 [4]:

$$\theta_i = \frac{\pm 1}{3}\left[\tan^{-1}\sqrt{\frac{I^{2\omega}_{p,i(MO)}}{I^{2\omega}_{s,i(MO)}}} + k\pi\right] \quad (3)$$

where k is an integer. In Eq. 3 we note that negative angle values and values with modulo $60^0$ are allowed. This is the well-known uncertainty in the calculation of the armchair orientation using the P-SHG technique [3], i.e. angles differing by integer multiples of π/3 are equivalent (this includes the case of negative solutions). Henceforth, we consider all armchair angles between $0^0$ and $60^0$ and therefore choose the positive solution of Eq. 3 for k = 0.

Then, for known $\theta_i$, by using Eq. 1 for $\varphi = 0^o$, we can instantaneously acquire $A_i$ through:

$$A_i = \frac{\sqrt{I^{2\omega}_{s,i(MO)}}}{\cos 3\theta_i} \quad (4)$$

In the overlapping region, the SHG signals of the two different TMD monolayers interfere and the overall produced SHG is governed by their vectorial addition. For the case of fixed pump linear polarization parallel to *X*-axis ($\varphi = 0^o$) and SHG detection *parallel* to *X*-axis, the SHG from *N* stacked TMD monolayers is described by:

$$I^{2\omega}_{s} = \left|\sum_{i=1}^{N} A_i \cos 3\theta_i\right|^2 \quad (5)$$

In the case of a heterobilayer (BI), Eq. 5 with $N = 2$ and $A_1 \neq A_2$ reduces to:

$$I^{2\omega}_{s(BI)} = \left[A_1 \cos 3\theta_1 + A_2 \cos 3\theta_2\right]^2 \quad (6)$$

If we now choose SHG detection *perpendicular* to *X*-axis, the SHG produced from the 2D heterostructure is given by:

$$I^{2\omega}_{p(BI)} = \left[A_1 \sin 3\theta_1 + A_2 \sin 3\theta_2\right]^2 \quad (7)$$

If we combine Eq. 6 and Eq. 7, we obtain:

$$\theta_2 = \frac{1}{3}\tan^{-1}\frac{\sqrt{I^{2\omega}_{p(BI)}} - A_1 \sin 3\theta_1}{\sqrt{I^{2\omega}_{s(BI)}} - A_1 \cos 3\theta_1} \qquad (8)$$

By combining Eq. 8 with Eq. 3 and Eq. 4, we acquire a formula that calculates the twist angle, from SHG intensity measurements:

$$\theta_2 - \theta_1 = \frac{1}{3}\left[\tan^{-1}\frac{\sqrt{I^{2\omega}_{p(BI)}} - \sqrt{I^{2\omega}_{p(MO)}}}{\sqrt{I^{2\omega}_{s(BI)}} - \sqrt{I^{2\omega}_{s(MO)}}} - \tan^{-1}\sqrt{\frac{I^{2\omega}_{p(MO)}}{I^{2\omega}_{s(MO)}}}\right] \qquad (9)$$

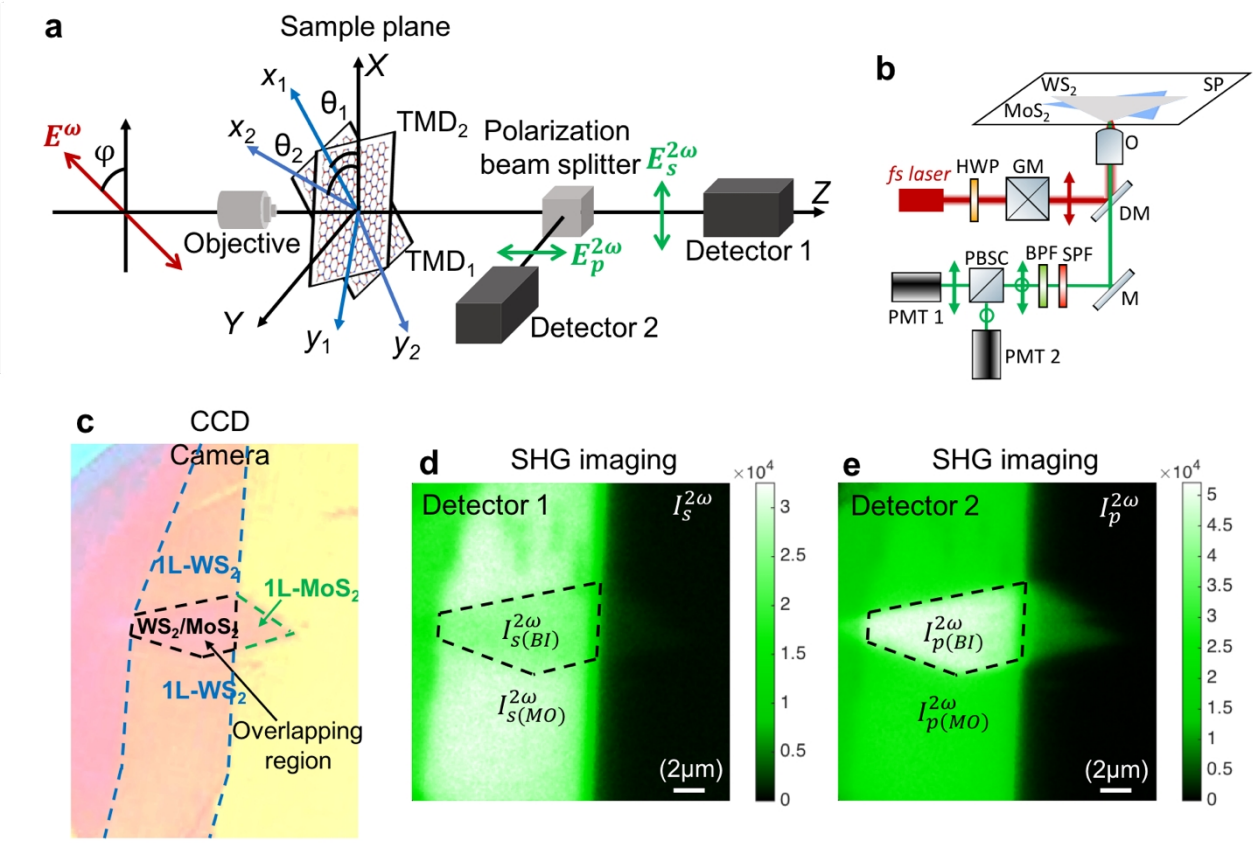


**Figure 3.1**. Basic principles of the reported SHG imaging technique for mapping twist angles in TMD heterobilayers. **a**) Illustration of the adopted experimental configuration. We have assumed fixed linear polarization of the laser beam parallel to *X*-axis ($\varphi = 0^o$. **b**) Illustration of the experimental setup (abbreviations are discussed in Methods). **c**) CCD image of the $WS_2/MoS_2$ heterobilayer we have studied. The regions of $WS_2$ monolayer, $MoS_2$ monolayer, and their overlap are denoted. **d**) SHG intensity image of the $WS_2/MoS_2$ heterobilayer, for the parallel to X-axis SHG component, $I^{2\omega}_{s,1(MO)}$ and **e**) for the perpendicular component, $I^{2\omega}_{p(BI)}$. For the real-time calculation of twist angle directly in the overlapping area, we need two SHG intensities for each SHG component,

all of which are obtained by a single-shot measurement; two in a plain monolayer region ($I^{2\omega}_{s,1(MO)}$ and $I^{2\omega}_{p,1(MO)}$) and two in the overlapping region ($I^{2\omega}_{s(BI)}$ and $I^{2\omega}_{p(BI)}$).

### 3.2.2 Experimental procedure

Following the above analysis, we can calculate the twist angle $\theta_2 - \theta_1$ using Eq. 9, by recording two SHG intensity measurements, one for the parallel (**Fig. 3.1d**) and one for the perpendicular to X-axis SHG component (**Fig. 3.1e**), i) in the region with only one TMD present and obtain $I^{2\omega}_{s(MO)}$ and $I^{2\omega}_{p(MO)}$, respectively, and ii) in the overlapping region of the two TMD monolayers and obtain $I^{2\omega}_{s(BI)}$ and $I^{2\omega}_{p(BI)}$, respectively. These four SHG intensity recordings, excited by a single-shot measurement, can be performed simultaneously using a polarization beam splitter and two orthogonally placed detectors, as shown in the experimental configuration in **Fig. 3.1a**. As a consequence, using Eq. 9, we can extract in real time the twist angle in the overlapping area. Considering that in our experiment we also utilize a laser raster-scanning approach (see Methods), we can additionally obtain in real time and in a single scan a map of the twist angle distribution in the overlapping area of a TMD heterobilayer. Note that although our method is demonstrated in a $MoS_2/WS_2$ heterobilayer, it is also applicable in other combinations of 2D TMDs as long as the centrosymmetry of the whole structure is not restored. In addition, graphene-based heterostructures with broken symmetry (e.g. strained) are also suitable for application of the real-time determination of the twist angle. Finally, the method can be extended to arbitrary number layers by successive application of Eq. 9 between adjacent layers. In this case, the armchair angle of the first layer is obtained by using Eq. 3 and then the twist angle between the first and second layer is determined through Eq. 9. In turn, the same equation is used for determining the twist angle between the second and third layer and so on and so forth.

Given that 2D TMD samples are a few nm thick, effects of birefringence or polarization scrambling due to scattering are negligible and therefore do not affect our polarization measurements. Calibration of the detector gain has been performed by imaging a $WS_2$ monolayer with armchair direction $\theta \sim 15^o$, and equating the SHG intensities recorded by the two orthogonally placed detectors, for excitation linear polarization angle $\varphi = 0^o$.

In order to create the $WS_2/MoS_2$ heterobilayer (**Fig. 3.1c**), both monolayers were produced by mechanical exfoliation and stacked with dry stamping on a $Si/SiO_2$ substrate. Prior to SHG measurements, the monolayers were characterized using Raman spectroscopy. The excitation source used for the SHG experiments is a fs oscillator with 1030nm fundamental pulse and repetition rate in the order of MHz, which is adequate to excite nonlinear signals including SHG and two-photon photoluminescence [3]. As the laser beam is scanning the sample, the SHG signal is recorded at frequent time intervals from every point of the sample and SHG images are created. Following this procedure (common for multi-photon and confocal microscopy), we acquire an image of 500x500 measurements (pixels) in about 1s and one of 900x900 pixels in about 3s.

### 3.2.3 Experimental results

As mentioned above, the produced SHG is recorded in two orthogonal polarization directions and therefore, in combination with the adopted laser raster-scanning technique, two SHG intensity images can be simultaneously obtained (**Fig. 3.1d** and **Fig. 3.1e**). We can then use these two SHG images as input to Eq. 3 and Eq. 9, in order to obtain pixel-by-pixel and in real time the crystal orientation for both the overlapping and the plain monolayer regions. Having implemented the above analysis in our microscope's image acquisition software, new real-time, pixel-by-pixel images are formed, mapping the crystal orientation of the monolayer areas as well as the twist angle in the overlapping region.

More specifically, for the particular case of our sample shown in **Fig. 3.1c**, upon using as input to Eq. 3 the values obtained from each pixel of the SHG images shown in **Fig. 3.1d** and **Fig. 3.1e**, we acquire the map depicted in **Fig. 3.2a**, along with its histogram presented in **Fig. 3.2b**, for a particular region of interest (ROI) (white rectangular in **Fig. 3.2a**). This histogram shows a spectrum in the angle domain, formed by the distribution of the armchair orientations present in the respective ROI. By correlating the position of the monolayer $WS_2$ in **Fig. 3.2a** with the colormap values of the figure, we identify in the histogram of **Fig. 3.2b** the peak that corresponds to its armchair orientation (lying between the two red dashed lines), providing mean armchair orientation $\langle \theta_{WS_2} \rangle = 14.34^o$, with standard deviation $\sigma = 0.49^o$ (**Fig. 3.2c**). Furthermore, in the overlapping region, we acquire using Eq. 9 the map of the twist angle of the $WS_2/MoS_2$ heterobilayer (**Fig. 3.2d**), providing *mean twist angle* $\langle \theta_{MoS_2} - \theta_{WS_2} \rangle = 7.01^o$ with $\sigma = 0.87^o$. Note that the central peak in the histogram of **Fig. 3.2b** corresponds to the so-called *effective armchair orientation* in the

overlapping region. This effective angle can also be used to calculate the twist angle, as in the case of TMD homostructures [5] (see supplementary information (available online at stacks.iop.org/2DM/8/015015/mmedia)).

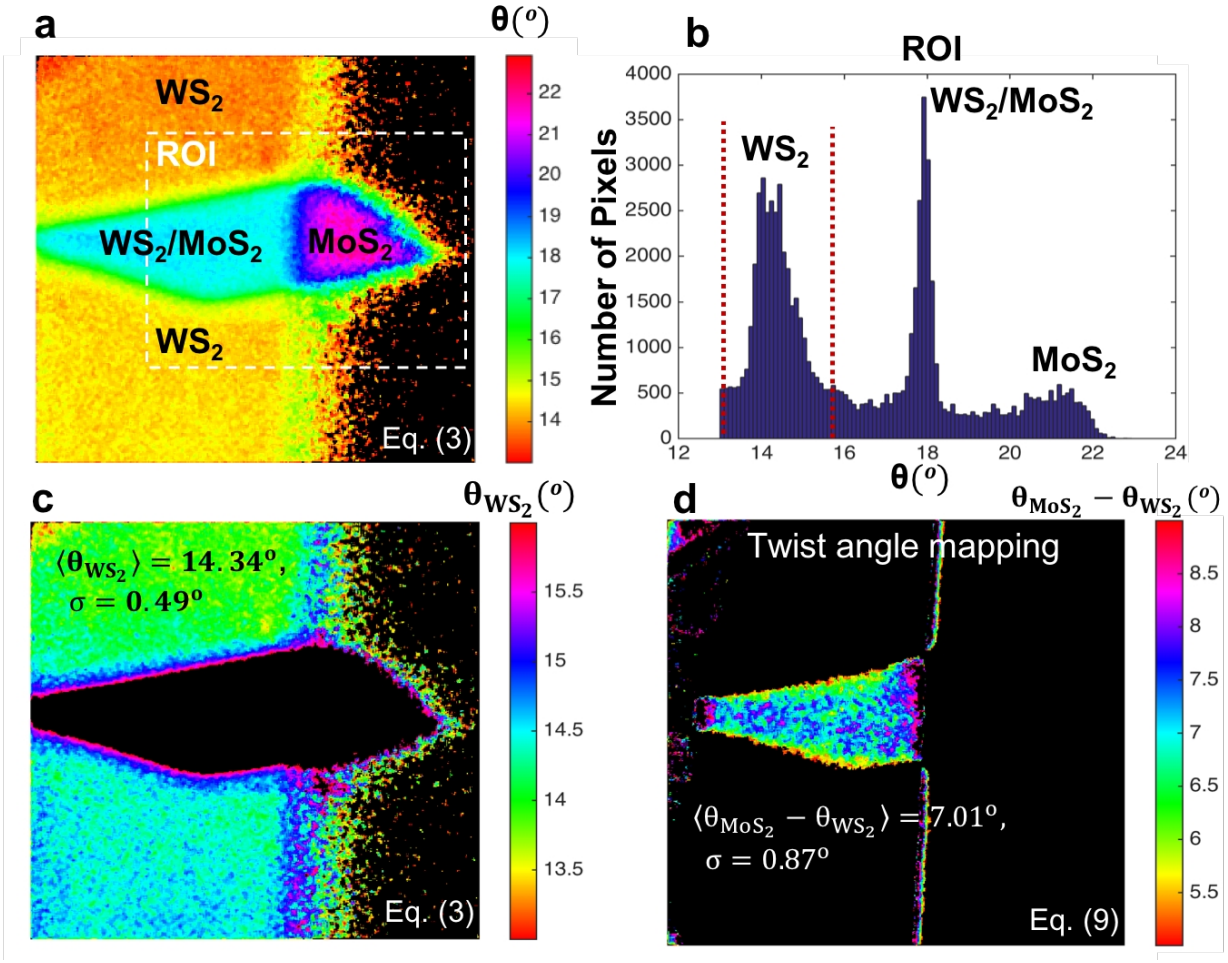


**Figure 3.2.** Demonstration of the reported methodology for mapping the twist angle in the $WS_2/MoS_2$ heterobilayer of Fig. 1c. **a**) Colormap and **b**) histogram (for the selected ROI) of the armchair orientations obtained upon using pixel-by-pixel the SHG intensity images of Fig. 3.1d and Fig. 3.1e as input to Eq. 3. Note that the values inside the overlapping area do not yet correspond to the twist angle, but to the $WS_2/MoS_2$ effective armchair orientation. **c**) Colormap of the monolayer $WS_2$ armchair orientation, created again by using as input to Eq. 3 the same SHG images, providing the shown mean value. **d**) Colormap of the twist angle, obtained upon using as input to Eq. 9 the same SHG images and the calculated $\langle \theta_{WS_2} \rangle$, providing the shown mean value.

In order to validate the results of the reported methodology, we use the value $\langle \theta_{WS_2} \rangle = 14.34^o$, extracted from **Fig. 3.2c**, the SHG intensity image of **Fig. 3.1d**, and Eq. 4, in order to calculate the

amplitude $A_{WS_2}$, obtaining $\langle A_{WS_2} \rangle = 4.12 \cdot 10^4$ with $\sigma = 0.73 \cdot 10^4$ (arbitary units). Then, with the values of $A_{WS_2}$ and $\theta_{WS_2}$ known, we can use Eq. 8 in the overlapping region to calculate the armchair orientation of $MoS_2$, giving $\langle \theta_{MoS_2} \rangle = 21.49^o$ with $\sigma = 1.08^o$. This value is very close to $\langle \theta_{MoS_2} \rangle = 21.05^o$ with $\sigma = 0.57^o$, obtained from our novel technique using Eq. 3 (**Fig. 3.3b**), for the area containing only $MoS_2$ monolayer shown in **Fig 3.3a**. This agreement within the range of σ validates the robustness of the real-time extraction of the twist angle inside the overlapping region of the $WS_2/MoS_2$ heterobilayer.

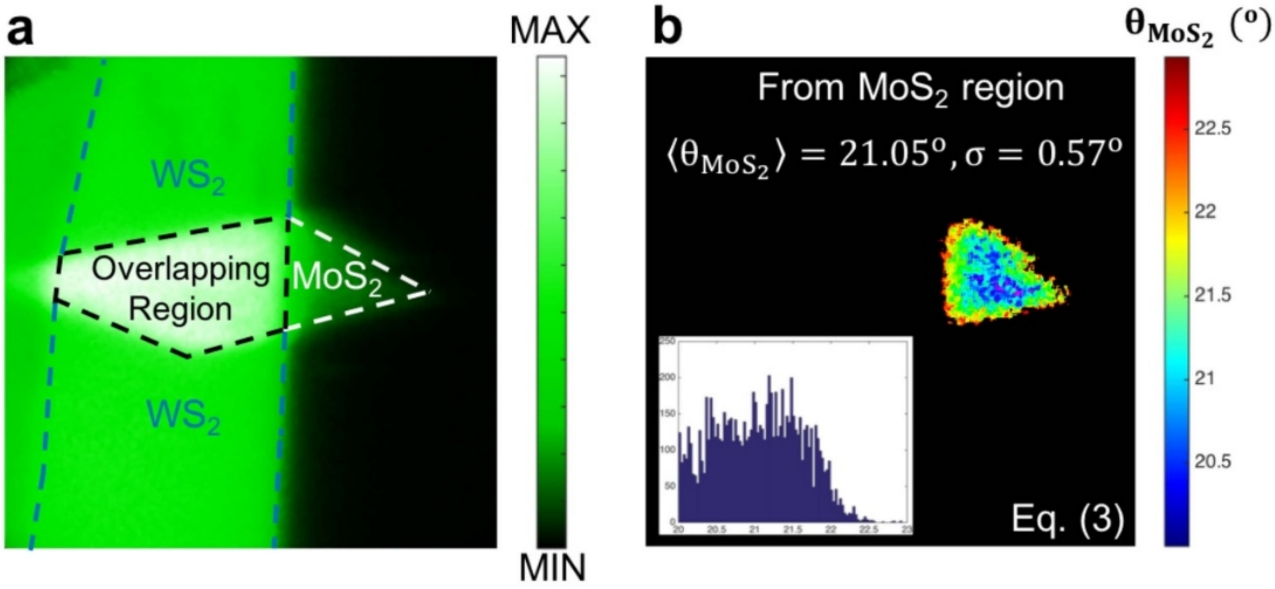


**Figure 3.3.** Validation analysis based on the real-time imaging of the armchair orientation of monolayer $MoS_2$, measured in the overlapping region and compared with the result from the area containing only $MoS_2$ monolayer. **a**) SHG intensity image of the $WS_2/MoS_2$ heterobilayer of Fig. 1c, which corresponds to the sum of Fig. 1d and Fig. 1e. The regions of $WS_2$ monolayer, $MoS_2$ monolayer, and the overlap are denoted. **b**) Imaging of the armchair orientation of monolayer $MoS_2$ measured in the region of individual $MoS_2$ monolayer, yields $\langle \theta_{MoS_2} \rangle = 21.05^o$ with $\sigma = 0.57^o$. In the overlapping region the calculated armchair angle is $\langle \theta_{MoS_2} \rangle = 21.49^o$, with $\sigma = 1.08^o$,. The two results are very close and within the range of σ. The histogram in the inset shows the respective angle distributions.

In order to further test our results, we have additionally performed independent high-resolution P-SHG measurements by rotating the excitation linear polarization angle $\varphi$ with step of 1°, and having removed the polarization beam splitter cube and the one detector from the setup of Fig. 3.1b [3]. In Fig. 3.4a we show representative P-SHG intensity snapshots for different orientations of $\varphi$ (denoted

by the white rotating arrow), for the perpendicular to X-axis SHG component $I_p^{2\omega}(\varphi)$. Three pixels of interest (POI) are also shown, one for each individual monolayer and one in the WS2/MoS2 heterobilayer region. By fitting the recorded P-SHG modulations $I_p^{2\omega}(\varphi)$ to Eq. 2, we acquire the armchair orientation for each POI (Fig. 3.4b-d). This P-SHG analysis yields individual armchair orientations $\theta_{WS_2}=14.13^o$ and $\theta_{MoS_2}=21.39^o$, for quality of fitting $R^2\geq 95\%$ and $R^2\geq 84\%$, respectively . These results are again very close to the results obtained from the reported real-time methodology, i.e. $\langle\theta_{WS_2}\rangle=14.34^o$ with $\sigma=0.49^o$ and $\langle\theta_{MoS_2}\rangle=21.05^o$ with $\sigma=0.57^o$. Note that the armchair orientation calculated in the overlapping area, $\theta_{WS_2/MoS_2}=18.83^o$ ($R^2\geq 93\%$) (Fig. 3.4d), again corresponds to the effective armchair orientation.

It is worth emphasizing that, usually until now, twist angles have been indirectly calculated via measuring both individual angles outside the overlapping area, with their difference considered as the twist angle inside the overlapping region [e.g. 6-11]. On the contrary, our methodology takes advantage of the SHG interference effect and its theoretical formulation, to map twist angles via SHG measurements performed directly in the overlapping region. This approach enables mapping of possible variations of a twist angle in the overlapping area due to crystal imperfections and/or strain effects, which were impossible to probe with the currently available methodologies.

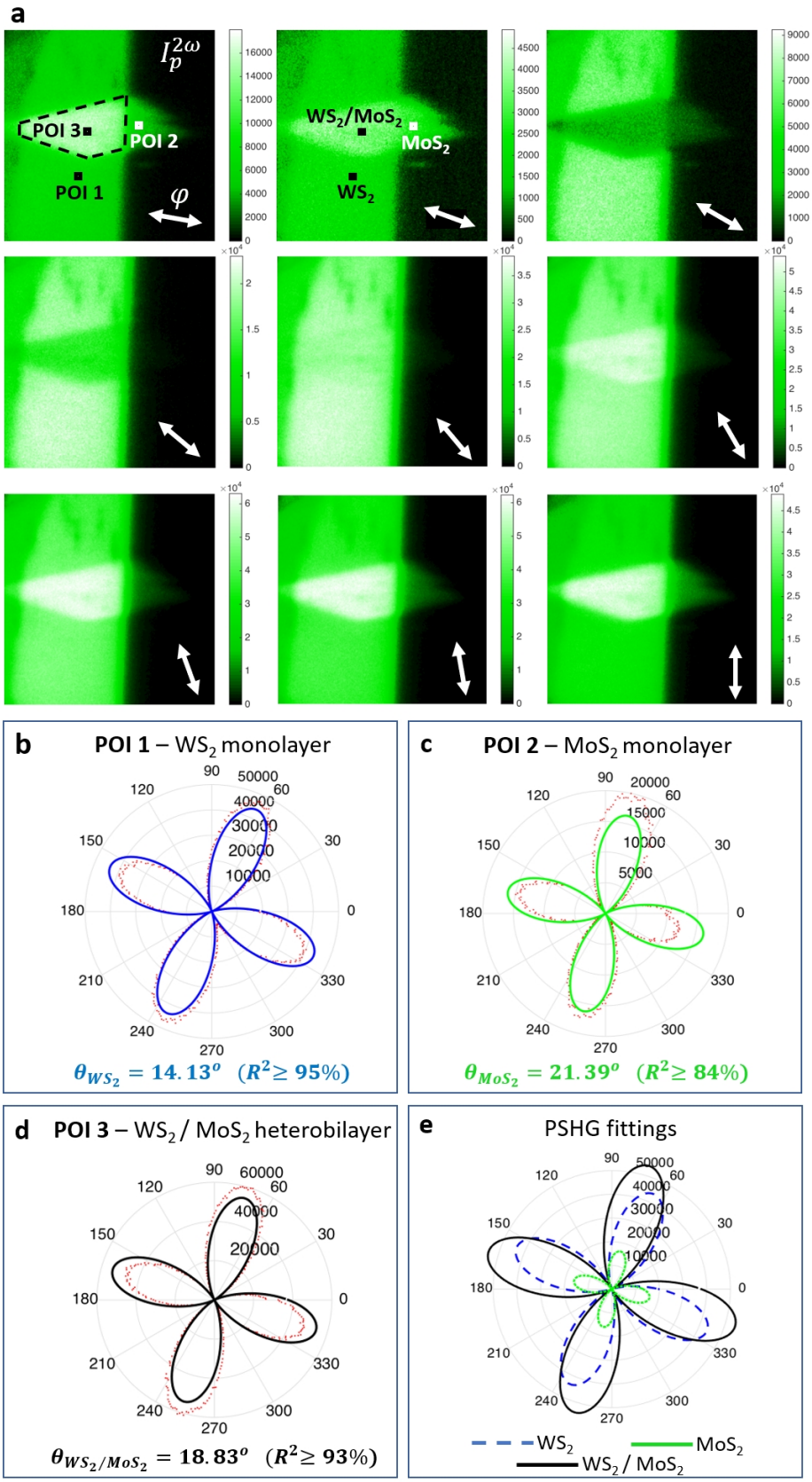


**Figure 3.4.** Further validation analysis based on the comparison of our results with independent P-SHG measurements. **a**) Representative P-SHG intensity snapshots of the perpendicular to X-axis

SHG component $I_p^{2\omega}(\varphi)$, obtained while rotating the linear polarization orientation $\varphi$ (white arrow) of the laser beam. We have selected three POIs, one for each individual monolayer and one in the $WS_2/MoS_2$ heterobilayer region. **b-d)** Polar diagrams of the recorded P-SHG modulations $I_p^{2\omega}(\varphi)$ for each POI, showing the data (red dots) and the fitting to Eq. 2 (blue, green and black line, respectively). This analysis produces individual armchair orientations $\theta_{WS_2}=14.13^o$ and $\theta_{MoS_2}=21.39^o$ (for the denoted quality of fitting $R^2$), which are again very close to the real-time demonstrated results. The calculated effective armchair orientation $\theta_{WS_2/MoS_2}$ in the overlapping region is also reported. **e)** Polar diagram presenting together the fitting lines from the three POIs.

## 3.3 Methods

### 3.3.1 Experimental apparatus

Our experimental apparatus is based on a diode-pumped Yb:KGW fs oscillator (1030 nm, 70–90 fs, 76 MHz, Pharos-SP, Light Conversion, Vilnius, Lithuania) guided into a custom-built Axio Observer Z1 (Carl Zeiss, Jena, Germany) inverted microscope (**Fig. 3.1b**). The laser beam is passing through a zero-order half-wave retardation plate (HWP) (QWPO-1030-10-2, CVI Laser), placed at a motorized rotation stage (M-060.DG, Physik Instrumente, Karlsruhe, Germany) that can rotate with high accuracy ($1^0$ for results in **Fig. 3.4b-d**) the orientation of the excitation linear polarization. Raster-scanning of the beam at the sample plane (SP) is performed using a pair of silver-coated galvanometric mirrors (GM) (6215H, Cambridge Technology, Bedford, MA, USA). The beam is reflected on a short-pass dichroic mirror (DM) at $45^0$ (DMSP805R, ThorLabs: Newton NJ, USA) placed at the motorized turret box of the microscope, just below the objective (O) (Plan-Apochromat 40x/1.3NA, Carl Zeiss). The mean polarization extinction ratio of the orthogonal linear polarization orientations, calculated using crossed polarization measurements at the sample plane, was 18:1. In the backward direction, the SHG signal is collected by the same objective used for excitation, passes through the dichroic mirror, is reflected by a mirror (M), and is separated from the residual laser pulse using a short-pass filter (SPF) (FF01-680/SP, Semrock, Rochester, NY, USA) and from any unwanted signal using a narrow bandpass filter (BPF) (FF01-514/3, Semrock). A polarization beam splitter cube (PBSC) (CCM5-PBS201, ThorLabs) is placed just in front of the two photomultiplier tube (PMT) modules (H9305-04, Hamamatsu, Hamamatsu City, Japan) to measure the orthogonal SHG signals. Coordination of PMT recordings with the galvanometric

mirrors for the image formation, as well as the movement of the motor, is carried out using LabView (National Instruments Austin, TX, USA) software.

### 3.3.2 Material fabrication and characterization

Information regarding the the sample preparation and characterization can be found in the original publication [12].

## References


[1] Malard, L. M., Alencar, T. V., Barboza, A. P. M., Mak, K. F. & de Paula, A. M. Observation of Intense Second Harmonic Generation from $MoS_2$ Atomic Crystals. Phys. Rev. B **87**, 201401(R) (2013).

[2] Janisch, C. et al. Extraordinary Second Harmonic Generation in Tungsten Disulfide Monolayers. Sci. Rep. **4,** 5530 (2015).

[3] Psilodimitrakopoulos, S. et al. Ultrahigh-resolution nonlinear optical imaging of the armchair orientation in 2D transition metal dichalcogenides. Light Sci. Appl. **7**, 18005 (2018).

[4] David, S. N. et al. Rapid, all-optical crystal orientation imaging of two-dimensional transition metal dichalcogenide monolayers. Appl. Phys. Lett. **107**, 111902 (2015).

[5] Psilodimitrakopoulos, S. et al. 2019 Twist angle mapping in layered WS2 by polarization-resolved second harmonic generation Sci. Rep. **9** 14285 (2019).

[6] Schaibley J R, Rivera P, Yu H, Seyler K L, Yan J, Mandrus D G, Taniguchi T, Watanabe K, Yao W and Xu X Directional interlayer spin-valley transfer in two-dimensional heterostructures Nat. Commun. **7** 13747 (2016)

[7] Seyler K L, Rivera P, Yu H, Wilson N P, Ray E L, Mandrus D G, Yan J, Yao W and Xu X 2019 Signatures of moiré-trapped valley excitons in $MoSe_2/WSe_2$ heterobilayers Nature **567** 66–70 (2019)

[8] Tran K et al 2019 Evidence for moiré excitons in van der Waals heterostructures Nature **567** 71–75 (2019)

[9] Jin C et al Observation of moiré excitons in $WSe_2/WS_2$ heterostructure superlattices Nature **567** 76–80 (2019)

[10] Alexeev, E. M. et al. Resonantly hybridized excitons in moiré superlattices in van der Waals heterostructures. Nature **567,** 81–86 (2019).

[11] Hsu, W.-T. et al. Negative circular polarization emissions from $WSe_2/MoSe_2$ commensurate heterobilayers. Nat. Commun. **9,** 1356 (2018).
[12] Psilodimitrakopoulos S, Mouchliadis L, Maragkakis G M, Kourmoulakis G, Lemonis A, Kioseoglou G, Stratakis E, 2D Mater. **8,** 015015 (2021).

# Chapter 4 - Nonlinear optical imaging of in-plane anisotropy in two-dimensional SnS


## Abstract

2D tin(II) sulfide (SnS) crystals belong to a class of orthorhombic semiconducting materials with remarkable properties, such as in-plane anisotropic optical and electronic response, and multiferroic nature. The 2D SnS crystals exhibit anisotropic response along the in-plane AC and ZZ crystallographic directions, offering an additional degree of freedom in manipulating their behavior. Here we take advantage of the lack of inversion symmetry of the 2D SnS crystal, that produces SHG, to perform P-SHG nonlinear imaging of the in-plane anisotropy. We fit the P-SHG experimental data with a nonlinear optics model, that allows us to calculate the AC/ZZ orientation from every point of the 2D crystal and to map with high-resolution the AC/ZZ direction of several 2D SnS flakes belonging in the same field of view. It is found that the P-SHG intensity polar patterns are associated with the crystallographic axes of the flakes and with the relative strength of the second-order nonlinear susceptibility tensor in different directions. Therefore, our method provides quantitative information of the optical in-plane anisotropy of orthorhombic 2D crystals, offering great promise for performance characterization during device operation in the emerging optoelectronic applications of such crystals.


## 4.1 Beyond state of the art

In this work, we extend the use of the P-SHG microscopy technique in order to investigate the properties of the orthorhombic 2D MXs. The P-SHG methodology applied here is based on high-resolution P-SHG imaging microscopy, with spatial resolution of approximately 500nm (see Methods). The subsequent fitting of the P-SHG polar diagrams for every pixel of the image with a theoretical model that accounts for the orthorhombic crystal structure of MXs, enables the calculation of the AC/ZZ direction from every point of a 2D SnS flake and the estimation of two ratios of the second-order nonlinear optical susceptibility tensor elements. We perform the same procedure for several different 2D SnS crystal flakes within the same field of view. It is shown that the mean and the standard deviation of the spatial distributions of the acquired values provide new

means of contrast capable to discriminate 2D SnS crystals in the same image based on their in-plane structural anisotropy. Therefore, our technique provides insight into the nonlinear optical properties of 2D MXs and can serve as a useful characterization tool for emerging applications.

## 4.2 Results and discussion

### 4.2.1 Theoretical formulation of SHG from orthorhombic MXs

In order to describe the interaction of an excitation field with a 2D orthorhombic MX crystal (**Fig. 4.1a**) and the subsequent production of SHG, we use the Jones formalism [1-7]. The two coordinate systems considered are schematically shown in **Fig. 4.1b**: the laboratory frame (X, Y, Z) and the crystal coordinates (x, y, z), where $z \equiv Z$. The laser beam propagates along Z axis, normally incident on the crystal, and linearly polarized along the sample plane, at an angle $\varphi$ with respect to X laboratory axis. By rotating the half-waveplate, we vary the orientation of the excitation linear polarization, and record the SHG emerging from the sample as function of the polarization angle φ. The x axis is taken parallel to the ZZ direction of the crystal and at angle $\theta$ from X. The y direction is then along the AC crystallographic direction, which coincides with the mirror symmetry axis (**Fig. 4.1a**).

The excitation field after passing the half-wave retardation plate can be expressed in laboratory coordinates by the Jones vector $\begin{pmatrix} E_0 cos\varphi \\ E_0 sin\varphi \end{pmatrix}$, where $E_0$ is the amplitude of the electric field. The expression of this vector in crystal coordinates is given by multiplying with the rotation matrix $\begin{pmatrix} cos\theta & sin\theta \\ -sin\theta & cos\theta \end{pmatrix}$, giving $E^{\omega} = \begin{pmatrix} E_0 \cos(\varphi - \theta) \\ E_0 \sin(\varphi - \theta) \end{pmatrix}$.

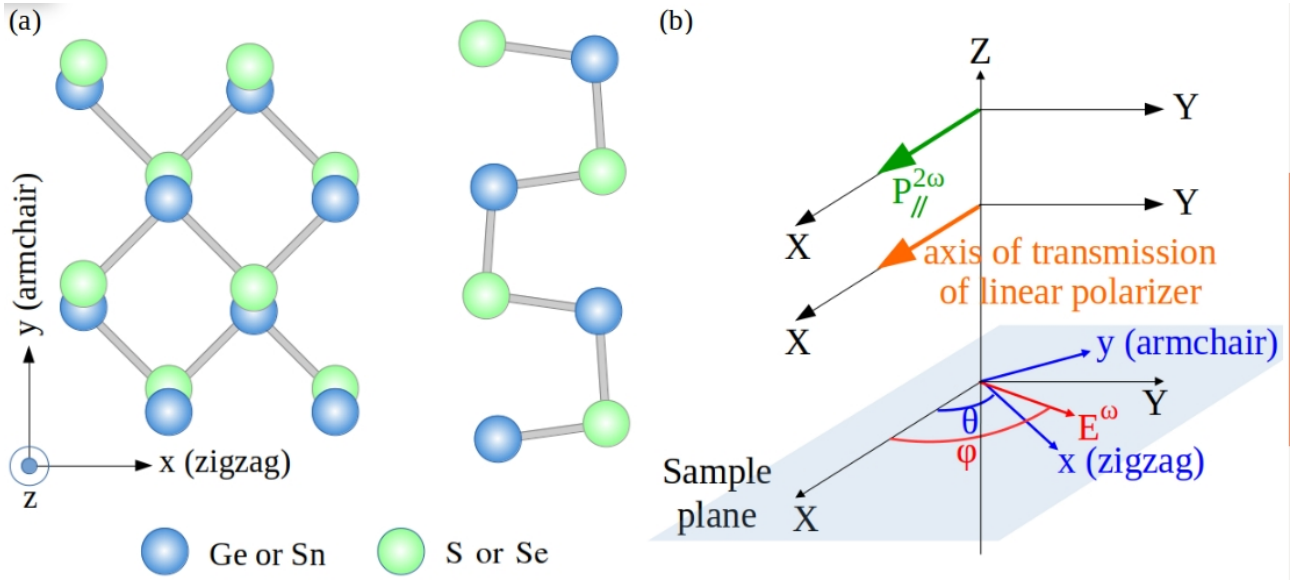


**Figure 4.1. a**) Schematic of the crystal structure of orthorhombic 2D MXs, as seen from the top (left) and the side (right). **b**) Illustration of the two coordinate systems, the laboratory X, Y, Z, and the crystal, x, y, Z, adopted in our experimental configuration. The angles φ and θ describe the orientation of the laser field $E^{\omega}$ and the ZZ crystallographic direction relative to the X laboratory axis, respectively. $P^{2\omega}_{//}$ shows the detected component of the generated SHG field.

The 2D MXs belong to the non-centrosymmetric, orthorhombic point group $C_{2v}$ (mm2) [8]. Thus, they have five independent, nonzero SHG susceptibility tensor elements, namely: $\chi^{(2)}_{yxx}, \chi^{(2)}_{yyy}, \chi^{(2)}_{yzz}, \chi^{(2)}_{xyx}=\chi^{(2)}_{xxy}$, and $\chi^{(2)}_{zzy}=\chi^{(2)}_{zyz}$, where $\chi^{(2)}_{ijk}$ is the second-order nonlinear optical susceptibility tensor element along the different directions [8]. As a result, the nonlinear polarization can be written in matrix form as [9]:

$$\begin{pmatrix} P_x^{2\omega} \\ P_y^{2\omega} \\ P_z^{2\omega} \end{pmatrix} = \varepsilon_0 \begin{pmatrix} 0 & 0 & 0 & 0 & 0 & \chi^{(2)}_{xxy} \\ \chi^{(2)}_{yxx} & \chi^{(2)}_{yyy} & \chi^{(2)}_{yzz} & 0 & 0 & 0 \\ 0 & 0 & 0 & \chi^{(2)}_{zyz} & 0 & 0 \end{pmatrix} \begin{pmatrix} E_x^{\omega} E_x^{\omega} \\ E_y^{\omega} E_y^{\omega} \\ E_z^{\omega} E_z^{\omega} \\ 2E_y^{\omega} E_z^{\omega} \\ 2E_x^{\omega} E_z^{\omega} \\ 2E_x^{\omega} E_y^{\omega} \end{pmatrix} \quad (1)$$

where $\varepsilon_0$ is the permittivity of the free space. Given that the excitation field is polarized along the sample plane, we have considered $E_z^{\omega}=0$, and thus the SHG equation is reduced to:

$$\begin{pmatrix} P_x^{2\omega} \\ P_y^{2\omega} \end{pmatrix} = \varepsilon_0 E_0^2 \begin{pmatrix} \chi^{(2)}_{xxy} \sin\left[2(\varphi-\theta)\right] \\ \chi^{(2)}_{yxx} \cos^2(\varphi-\theta) + \chi^{(2)}_{yyy} \sin^2(\varphi-\theta) \end{pmatrix} \quad (2)$$

where terms including only three independent SHG susceptibility tensor elements survive. We then transform this expression back to laboratory coordinates. In order to account for the effect of the linear polarizer placed before the detector, we multiple the SHG field with the Jones matrix $\begin{pmatrix} \cos^2\zeta & sin\zeta cos\zeta \\ sin\zeta cos\zeta & \sin^2\zeta \end{pmatrix}$, where ζ is the angle between the transmission axis of the polarizer and the X laboratory axis. In this work, we have set $\zeta = 0$, i.e., the axis of transmission of the polarizer parallel to X axis, and we measure the corresponding component of the SHG response, $P_{//}^{2\omega}$, whose intensity $I_{//}^{2\omega}$ is calculated as:

$$I_{//}^{2\omega} \sim \frac{1}{16}\left[\begin{array}{c} 2\left(\chi_{yxx}^{(2)}+\chi_{yyy}^{(2)}\right)sin\theta+\left(2\chi_{xxy}^{(2)}-\chi_{yxx}^{(2)}+\chi_{yyy}^{(2)}\right)\sin(\theta-2\varphi) \\ +\left(2\chi_{xxy}^{(2)}+\chi_{yxx}^{(2)}-\chi_{yyy}^{(2)}\right)\sin(3\theta-2\varphi) \end{array}\right]^2 \quad (3)$$

In this relationship, the SHG intensity is expressed in terms of the absolute values of the $\chi^{(2)}$ tensor elements. Instead, we can express it in terms of dimensionless ratios of the $\chi^{(2)}$ tensor elements, obtaining:

$$I_{//}^{2\omega} = a\left[2(b+1)sin\theta+(2c-b+1)\sin(\theta-2\varphi)+(2c+b-1)\sin(3\theta-2\varphi)\right]^2 \quad (4)$$

where

$$b = \chi_{yxx}^{(2)}/\chi_{yyy}^{(2)}, c = \chi_{xxy}^{(2)}/\chi_{yyy}^{(2)} \quad (5)$$

and $a = \varepsilon_0^2 E_0^4/\left[16\left(\chi_{yyy}^{(2)}\right)^2\right]$ is a multiplication factor. The SHG intensity can also be expressed in the equivalent form, which is used to fit the P-SHG experimental data:

$$I_{//}^{2\omega} = a\left[2(b+1)sin\theta+(b-1)\left[(e-1)\sin(\theta-2\varphi)+(e+1)\sin(3\theta-2\varphi)\right]\right]^2 \quad (6)$$

where

$$e = 2c/(b-1) \quad (7)$$

In **Fig. 4.2**, we present the numerical simulation of the $I_{//}^{2\omega}$ modulation, described by Eq. 4, in polar plots, as a function of the orientation of the linear polarization of the excitation field, φ, for fixed values of b, c, and for different AC/ZZ directions. Remarkably, the shape of the polar diagram itself is predicted to change for different values of the AC/ZZ directions. Three possible shapes are obtained: one with four symmetric lobes, one with four lobes symmetric in pairs, and one with two symmetric lobes. This shape change is in contrast to the corresponding behavior of the P-SHG polar diagrams of monolayer TMDs, which belong to the $D_{3h}$ point symmetry group, for which the $\chi^{(2)}$ tensor exhibits only one independent element [1, 2]. In that case, we have observed a characteristic four-lobe pattern, which rotates for different values of the crystal armchair direction.

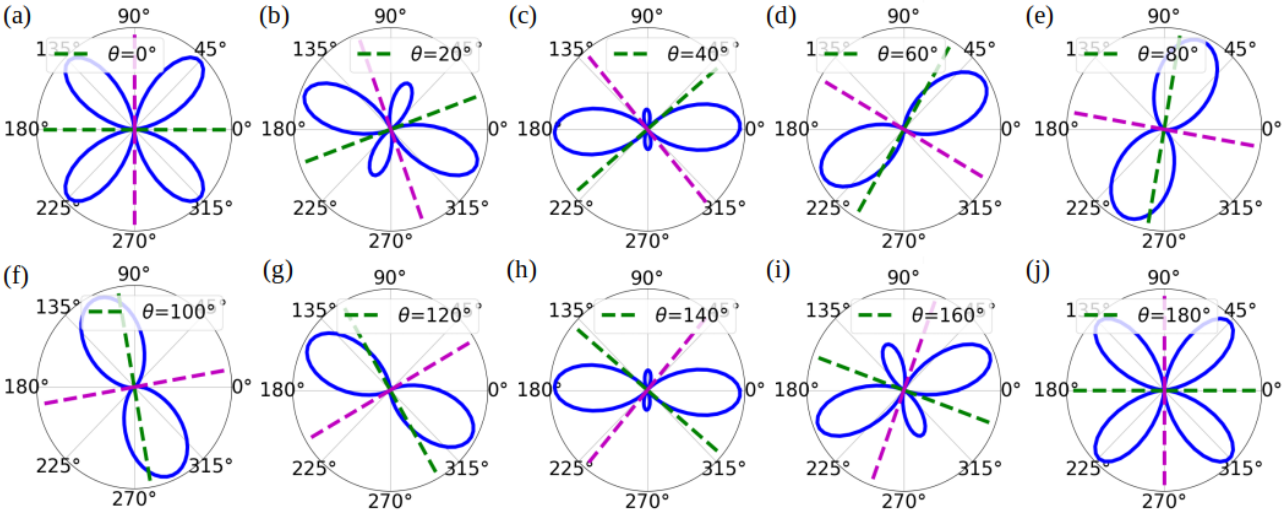


**Figure 4.2.** Numerical simulations of the theoretical P-SHG intensity produced by a 2D MX, described by Eq. 4. We plot $I_{//}^{2\omega}$ in polar diagrams, as a function of the orientation of the linearly polarized excitation angle φ for fixed values $b=5$, $c=6.5$, and for different ZZ directions θ, with θ ϵ $[0^{\circ}, 180^{\circ}]$ with step $20^{\circ}$. The AC/ZZ directions are illustrated with the magenta/green lines for each case.

The changes in the shape of the P-SHG polar diagrams, shown in **Fig. 4.2**, reflect the in-plane anisotropy of the orthorhombic MXs. Indeed, the origin of this shape change is described by Eq. 6, where the SHG intensity depends on four parameters, i.e., a, b, c and θ. We are therefore able to establish a direct link between the P-SHG intensity modulation and the in-plane anisotropy of orthorhombic MXs through these four parameters. In particular, the shape of the theoretically predicted P-SHG polar diagrams shown in **Fig. 4.2** is determined by the corresponding ZZ direction θ and the tensor elements ratios b and c. The parameters b and c (Eq. 5) denote the relative contribution of different directions to the SHG signals. In **Fig. 4.3, 4.4** we simulate the effect of different values of the $\chi^{(2)}$ element ratios b and c, respectively, on the P-SHG polar diagrams.

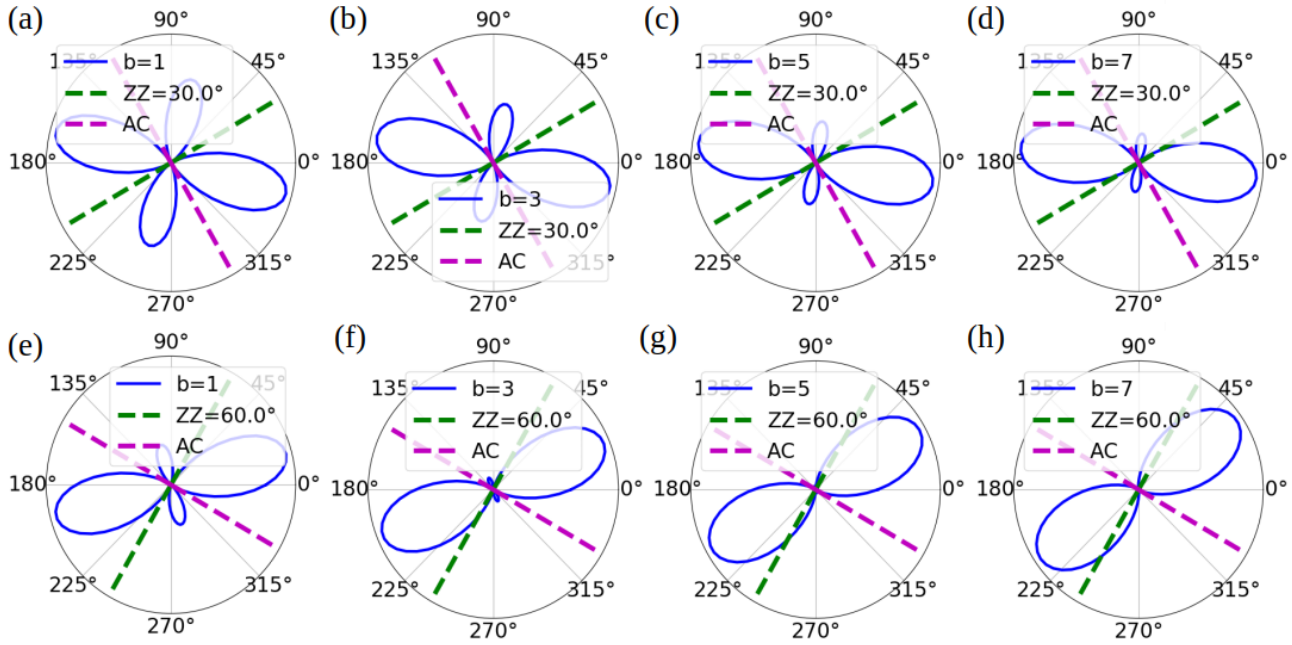


**Figure 4.3.** Theoretical simulation of the P-SHG intensity produced by a group IV monochalcogenide, described by Eq. 4. In order to investigate the effect of the $x^{(2)}$ tensor element ratio b, we plot $I_{//}^{2\omega}$ in polar diagrams, as function of the orientation of the linear polarization of the pump laser beam, φ, for fixed value $c = 6.5$, and for two different AC/ZZ directions.

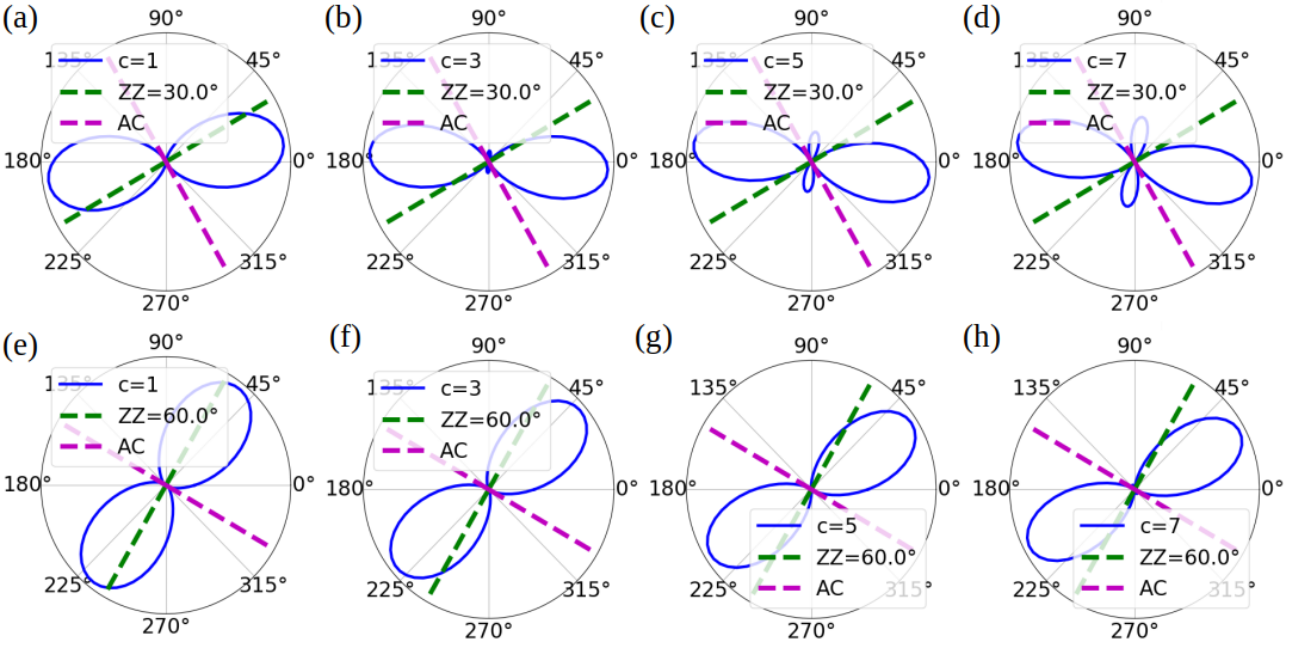


**Figure 4.4.** Theoretical simulation of the P-SHG intensity produced by a group IV monochalcogenide, described by Eq. 4. In order to investigate the effect of the $x^{(2)}$ tensor element

ratio c, we plot $I_{//}^{2\omega}$ in polar diagrams, as function of the orientation of the linear polarization of the pump laser beam, φ, for fixed value $b=5$, and for two different AC/ZZ directions.

In contrast to the monolayer TMDs where the AC direction can be calculated modulo 60° (due to their threefold rotational symmetry i.e., the fact that they have three equivalent AC axes), in the case of 2D MXs, the AC direction is unique. This is readily reflected in the SHG polar diagrams of MXs which are the same every 180° in the AC/ZZ direction.

To describe the SHG intensity generated from an ultrathin orthorhombic 2D MX, with N number of layers with AA stacking sequence, we extend the interference model introduced for 2D TMDs [3, 10]. Neglecting propagation effects, the second harmonic field arising will have the form of vector superposition:

$$E^{2\omega}=E_1^{2\omega}+E_2^{2\omega}+...+E_N^{2\omega} \quad (8)$$

where the indices denote the second harmonic signal from the corresponding layers. The total SHG intensity produced by the N-layer structure, will then be:

$$I^{2\omega}=\left|E_1\right|^2+\left|E_2\right|^2+...+\left|E_N\right|^2+2E_1\cdot E_2+...+2E_{N-1}\cdot E_N \quad (9)$$

$$I^{2\omega}=I_1+I_2+...+I_N+2\sqrt{I_1 I_2}\cos\delta_{1,2}+...+2\sqrt{I_{N-1}I_N}\cos\delta_{N-1,N} \quad (10)$$

where $\delta_{i,j}$, $i,j=1,2,...,N$ denote the relative angle between layers $i$ and $j$, i.e., the twist-angles, and the frequency index 2ω is suppressed for simplicity. If we assume for simplicity that the SHG intensity from the individual layers is equal ($I_1=I_2=...=I_N=I_{ML}$) and that the three layers are aligned (i.e., all twist-angles are zero), we find that

$$I^{2\omega}=N I_{ML}+I_{ML}N(N-1) \quad (11)$$

$$I^{2\omega}=N^2 I_{ML} \quad (12)$$

This is the well-known result that the SHG intensity from 2D flakes with zero twist-angle scales quadratically with the number of layers. It is valid for ultrathin non-centrosymmetric SnS with AA stacking sequence, where each layer contributes constructively in the detected SHG.

### 4.2.2 Nonlinear imaging of in-plane anisotropy in SnS

Using our custom-built polarization-resolved nonlinear microscope presented in **Fig. 4.5**, we raster-scan a specific sample area, and by rotating the linear polarization angle of the pump beam, φ, with a step of 2°, we record 180 spatially resolved images of $I_{//}^{2\omega}$. We then fit those images with Eq. 6 and estimate: i) the ZZ direction θ (and thus the perpendicular AC direction too); ii) the $\chi^{(2)}$ tensor

element parameters b and e; and iii) the multiplication factor a. This is performed for every pixel of the image enabling the extraction of spatially resolved images of the ZZ crystal direction and the tensor element parameter values, as well as the corresponding distributions of such values.

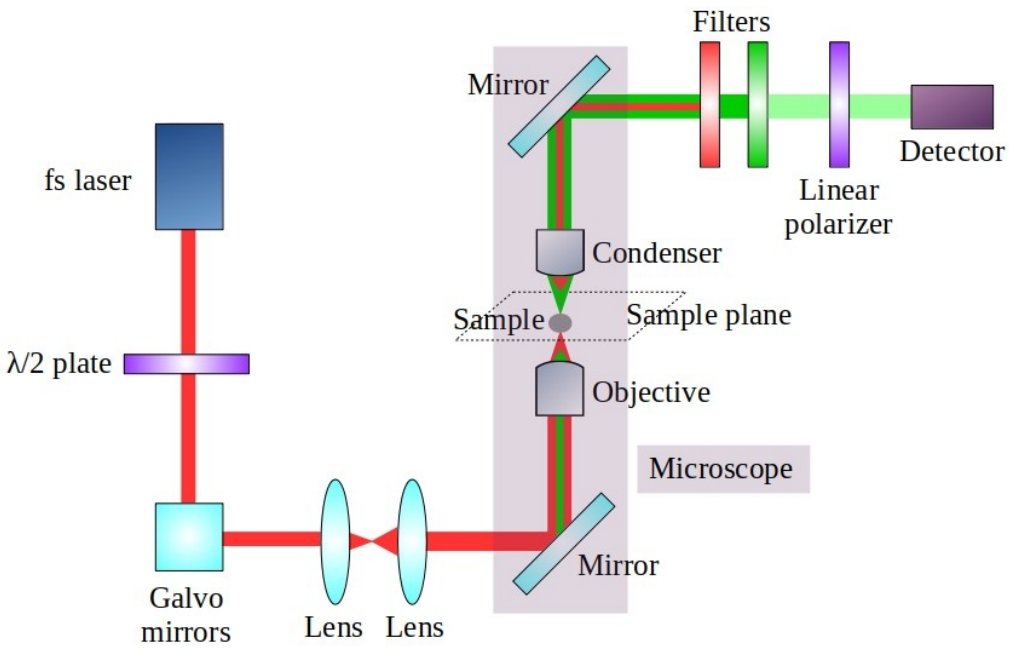


**Figure 4.5.** Illustration of the experimental setup. The fs laser beam is guided into the microscope and excites SHG produced by a stationary 2D SnS crystal. By rotating a λ/2 plate, we rotate the orientation of the linear polarization of the excitation field, as a function of which we record the second harmonic signal. A pair of galvanometric mirrors is used to raster-scan an area of the sample and obtain SHG images. The setup is discussed in detail in Methods.

In order to confirm the SHG process, we measure the average SHG intensity produced by a 2D SnS flake as function of the excitation power, shown in **Fig. 4.6** in a log-scale plot. Indeed, we obtain a quadratic power-law dependence, as expected.

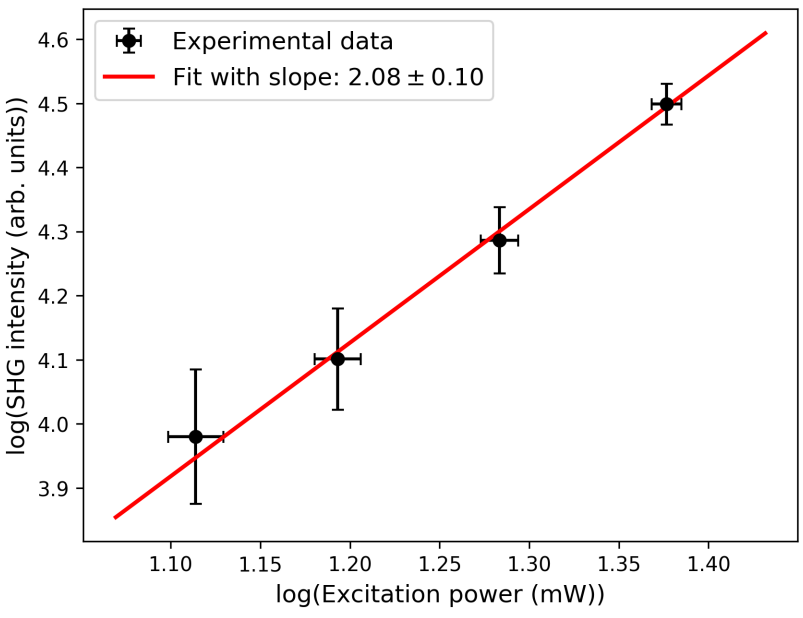

**Figure 4.6.** Log-scale plot of the average SHG intensity produced by a 2D SnS flake as function of the excitation power. The quadratic dependence confirms the SHG process.

In **Fig. 4.7**, we present representative P-SHG images of different 2D SnS crystals, belonging in the same field of view, for several orientations of the laser linear polarization φ denoted by the red arrow. A number of SnS flakes, appearing as bright spots of submicron dimensions, is observed. Six regions of interest (ROIs) containing SnS crystals are illustrated by the white arrows. While changing φ, we observe differences in the SHG intensity of the individual SnS flakes, in accordance with the theoretical predictions of Eqs. 4 and 6. We also note that the detected SHG signals from the different flakes are modulating out of phase. This is due to the different AC/ZZ crystallographic orientations and/or due to differences in the tensor element ratios among the different SnS flakes.

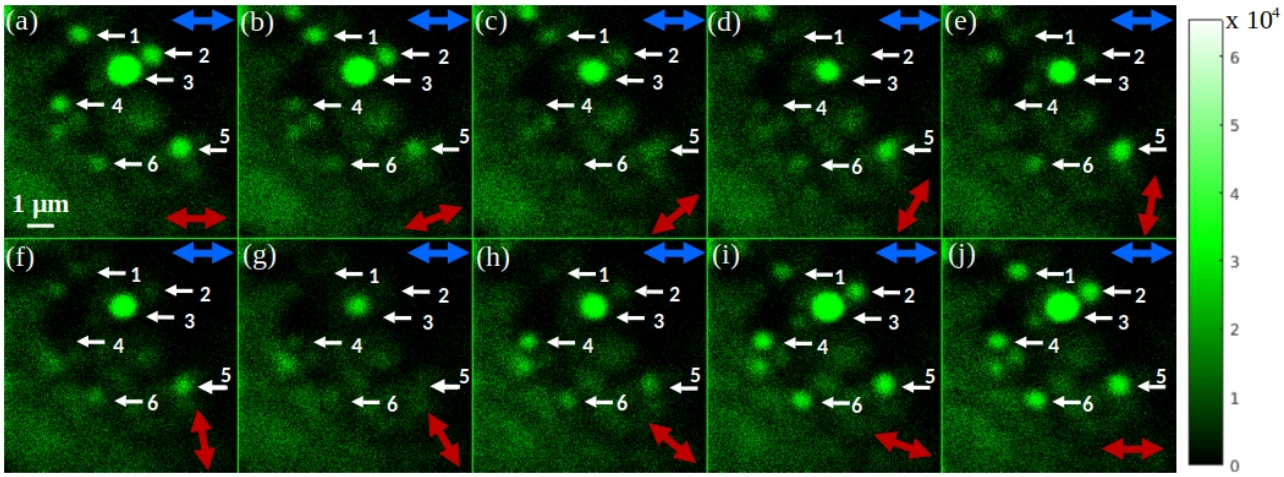


**Figure 4.7.** Experimental P-SHG images of ultrathin SnS crystals belonging in the same field of view for different values of the orientation of the laser linear polarization (φ in Eq. 4), denoted by the red arrows, with φ ϵ [0°, 180°] with step 20°. The blue arrows indicate the direction of the polarization of the detected SHG signals. Brighter color indicates higher P-SHG intensity in arbitrary units. We note that the SHG signals from the 2D SnS crystals (ROIs 1-6 pointed by the arrows), are modulating out of phase. The scale bar in the first image illustrates 1 μm.

We focus on six regions of interest (ROIs) containing SnS crystals, illustrated by white arrows in **Fig. 4.7**. In **Fig. 4.8a**, we present for such ROIs the sum of the 180 P-SHG intensity images for all orientations of the excitation linear polarization φ. In **Fig. 4.8b-g** , we present polar plots of the P-SHG modulation (in red dots) taken from one pixel inside the ROIs depicted in **Fig. 4.8a**. These modulations agree with the mean and the integrated P-SHG modulation of each ROI (see **Fig. 4.9**

for two representative examples). We note that the diagrams in **Fig. 4.8b-g** confirm the theoretical prediction that different SnS flakes can produce P-SHG polar plots of different shape (see **Fig. 4.2**), depending on the ZZ crystallographic direction and the parameters b and e. Using our methodology, this is observed within the same field of view, providing new means of contrast. The third possible shape of the P-SHG polar diagrams, with two single lobes as theoretically predicted in **Fig. 4.2d-g**, has been also experimentally demonstrated for another SnS flake and is presented in **Fig. 4.10**. By fitting (blue line) the experimental data with Eq. 6, we are able to calculate the AC/ZZ crystallographic direction and the $\chi^{(2)}$ element ratios, i.e., parameters b and c for each pixel (summarized in **Table 4.1**).

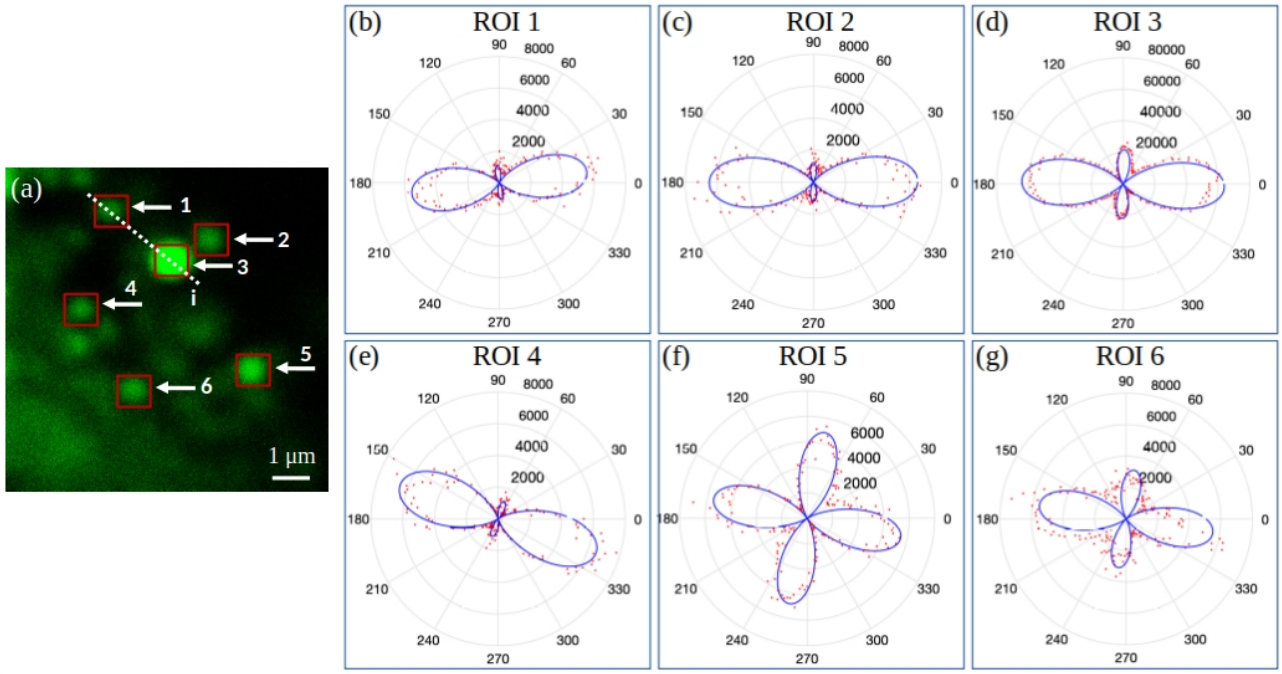


**Figure 4.8. a**) Sum of the SHG intensity for all orientations of the linearly polarized excitation angle φ, corresponding to the same field of view shown in **Fig. 4.7**. Brighter color indicates higher SHG intensity. The scale bar illustrates 1 μm. **b-g**) Experimental data (red dots) of the P-SHG intensity taken from one pixel inside each ROI depicted in **Fig. 4.8a**, presented in polar plots as function of the angle φ. By fitting (blue line) with Eq. 6, we are able to calculate the ZZ crystallographic direction and the tensor element parameters b and e, for each pixel (summarized in **Table 4.1** Interestingly, the shape of the polar-diagrams changes for different flakes, which is the signature of differences in their in-plane anisotropy.

**Table 4.1.** Summary of the fitted parameters θ, a, b and e, for all datasets demonstrated in **Fig. 4.8b-g**, with the corresponding quality of fitting $R^2$. The $\chi^{(2)}$ parameter c is calculated through Eq. 7.

| ROI | Zigzag direction θ (°) | Parameter a (arb. units) | Parameter $b = \chi^{(2)}_{yxx} / \chi^{(2)}_{yyy}$ | Parameter e | Quality of fitting | Parameter $c = \chi^{(2)}_{xxy} / \chi^{(2)}_{yyy}$ |
|---|---|---|---|---|---|---|
| 1 | -33.96 | 2.78 | 5.05 | 7.33 | 85 % | 14.84 |
| 2 | -40.35 | 2.57 | 6.16 | 7.15 | 92 % | 18.45 |
| 3 | 40.76 | 2.29 | 16.34 | 8.55 | 91 % | 65.58 |
| 4 | 23.67 | 2.56 | 9.09 | 3.75 | 91 % | 15.17 |
| 5 | 29.25 | 0.30 | 13.05 | 3.77 | 73 % | 22.71 |
| 6 | 29.36 | 0.91 | 12.59 | 3.07 | 56 % | 17.79 |

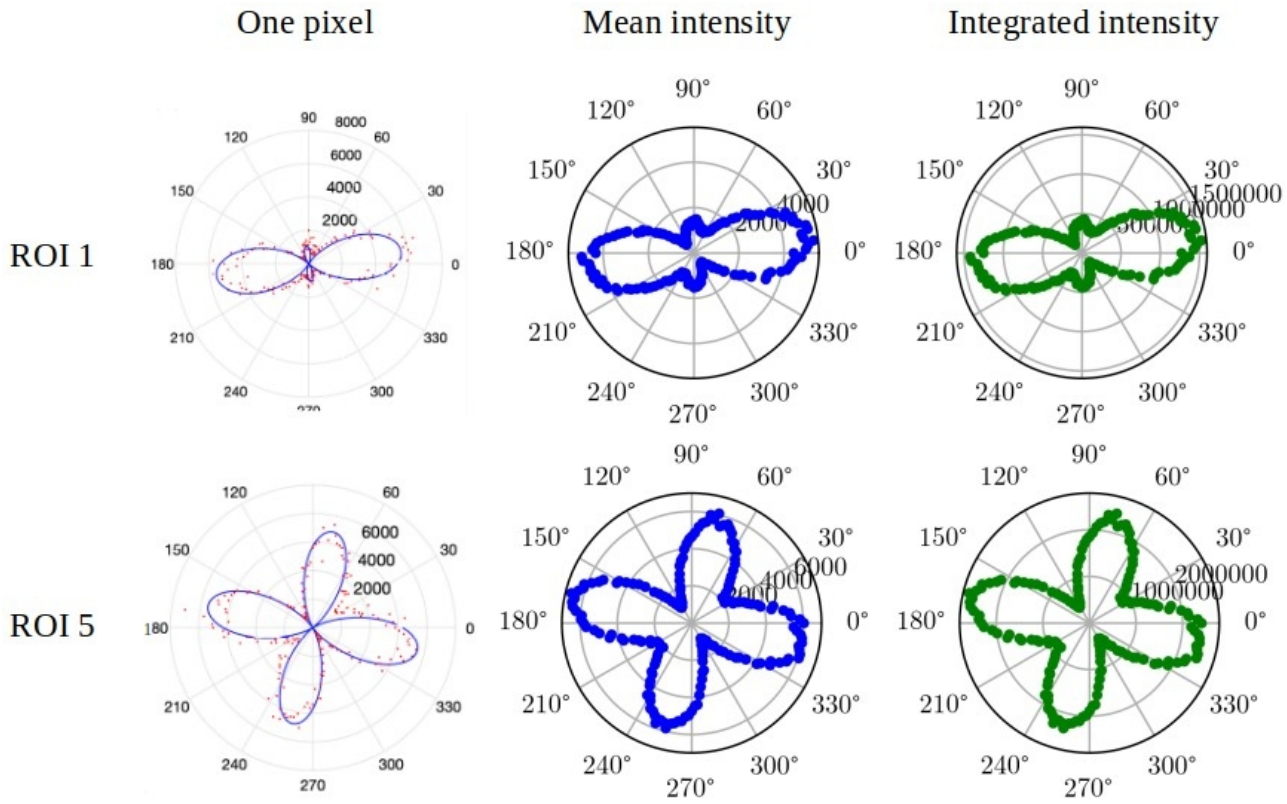


**Figure 4.9.** Comparison of the P-SHG modulation of one pixel of ROI 1 (**Fig. 4.8a**) and ROI 5 (**Fig. 4.8a**) with the corresponding P-SHG modulations of the mean intensity and the integrated intensity (sum of the intensity) of the whole ROI.

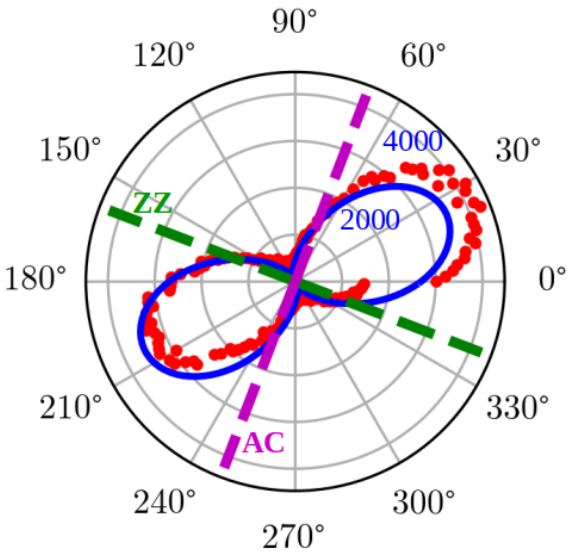


**Figure 4.10.** Experimental data (in red) of the SHG intensity as function of the incident field polarization angle, φ, in polar plots, for a flake of similar SnS. By fitting (blue line) with the SHG equation we have derived (Eq. 4), we are able to calculate the AC/ZZ crystallographic direction for each flake.

This fitting can also be performed in a pixel-by-pixel manner, producing spatially resolved ZZ orientation maps. Such maps along with their corresponding image histograms are presented in **Fig. 4.11**, for the ROIs 1, 4-6 depicted in **Fig. 4.8a**. Although, to date, only micrometer-size SnS monolayers have been realized, our technique can provide useful information on crystal quality and the presence of grain boundaries and defects in larger-area crystals [1, 2]. Using the same fitting procedure, we additionally produce distributions of values (image histograms) for the $\chi^{(2)}$ tensor element parameters b and e, which are presented in **Fig. 4.12**. All such histograms are subsequently fitted with a Gaussian function in order to calculate the mean and standard deviation of the distribution of values for each parameter. **Table 4.2** summarizes the results of the fitted parameters θ, b and e (mean and sigma), along with the values of c, calculated through Eq. 7. Considering the broad range of the b, c and e values, the results listed in **Table 4.2** provide experimental and quantitative evidence on the highly anisotropic nature of the $\chi^{(2)}$ tensor of SnS.

To compare our findings with the literature, we use the values of the $\chi^{(2)}$ tensor elements of monolayer MXs that have been theoretically calculated from first-principles using density functional theory [8]. For the particular case of SnS and for excitation pulse centred at $1028\,nm$ ($\hbar\omega \simeq 1.2\,eV$), they have been calculated to be $\chi^{(2)}_{yyy} \simeq 65 \cdot 10^4\, pm^2 V^{-1}$, $\chi^{(2)}_{yxx} \simeq 50 \cdot 10^4 \frac{pm^2}{V}$,

$\chi^{(2)}_{yyy} \simeq 10 \cdot 10^4\, pm^2 V^{-1}$ (see Fig. S2d in Ref. [8]). These values correspond to $b = \chi^{(2)}_{yxx}/\chi^{(2)}_{yyy} \simeq 5$, $c = \chi^{(2)}_{xxy}/\chi^{(2)}_{yyy} \simeq 6.5$, $e = 2c/(b-1) \simeq 3.25$, which agree with the experimental evidence that c is higher than b, while such values are within the same order of magnitude with the experimental values of **Table 4.2**. The deviations from the literature values, the broad histograms, and the different values of the $\chi^{(2)}$ parameters among different 2D SnS crystals may be attributed to i) deformation in the crystal lattice during the sample preparation [11], ii) varying contributions to the SHG signal from the $\chi^{(2)}$ tensor elements along different directions, and iii) the adopted fitting procedure. Indeed, to our knowledge, there is only one work in which the authors have experimentally calculated relative magnitudes of the $\chi^{(3)}$ (instead of the $\chi^{(2)}$) tensor of a MX (few-layer GeSe) [11]. In this work, the authors have also reported deviations among different flakes, which they state that may be attributed to the deformation in the crystal lattice during the exfoliation process. Such phenomenon has also been observed in the anisotropic third harmonic generation in the exfoliated black phosphorus flakes [12].

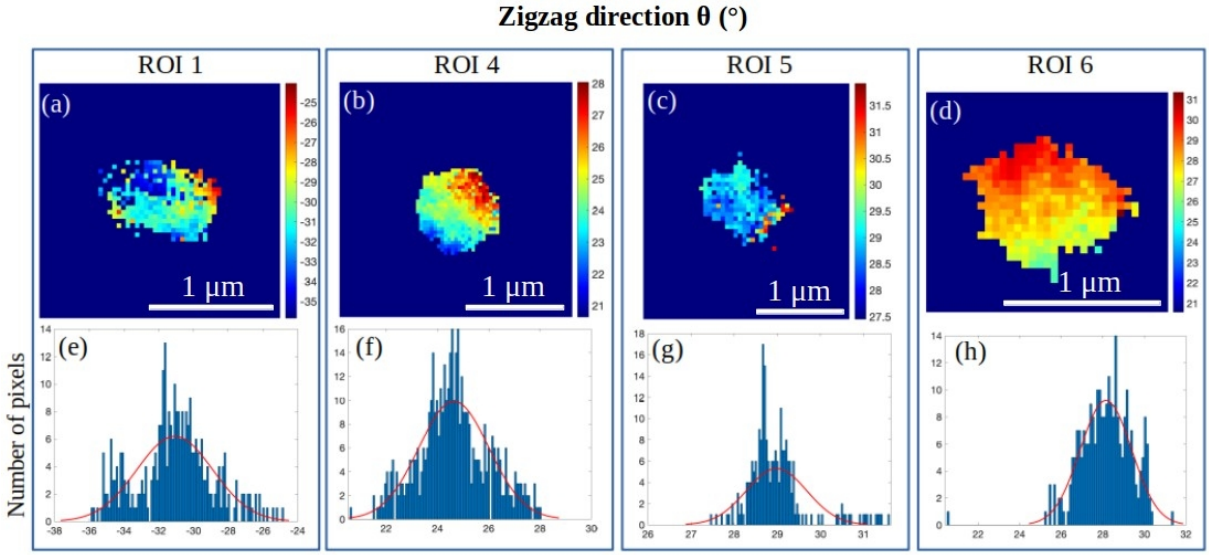


**Figure 4.11. a-d**) Pixel-by-pixel spatially resolved mapping of the ZZ crystallographic direction θ for the ultrathin SnS crystals which correspond to the ROIs 1, 4-6 depicted in **Fig. 4.8a**. We present pixels that survived quality of fitting larger than 80%, 88%, 67% and 50%, respectively. **e-h**) Corresponding image histograms showing the distributions of the values of the ZZ directions and the Gaussian fit (red line). The fitted parameters of the Gaussian fit are summarized in **Table 4.2**.

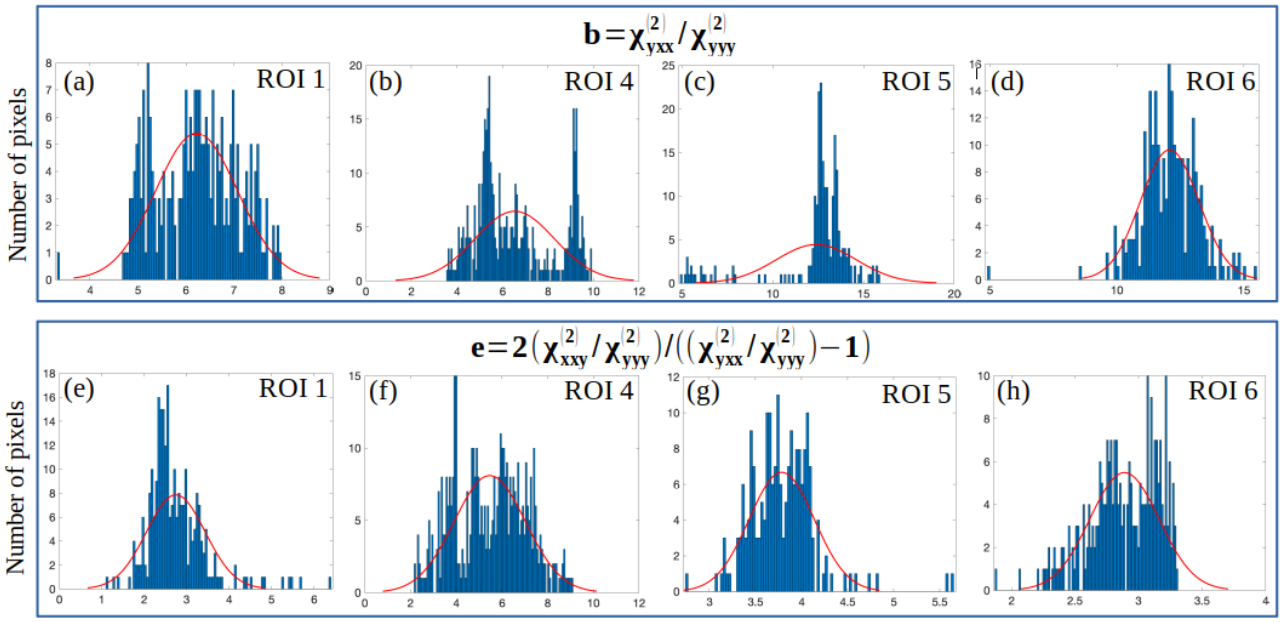


**Figure 4.12. a-d**) Histograms of the fitted $\chi^{(2)}$ parameter b (Eq. 5), and **e-h**) the fitted $\chi^{(2)}$ parameter e (Eq. 7), for the ultrathin SnS crystals which correspond to the ROIs 1, 4-6 depicted in **Fig. 4.8a**. We present pixels that survived quality of fitting larger than 80%, 88%, 67% and 50%, respectively. The fitted parameters of the Gaussian fit (red line) are summarized in **Table 4.2**.

**Table 4.2.** Summary of the fitted parameters θ, b and e (mean and standard deviation), based on the Gaussian fit illustrated in the representative histograms in **Fig. 4.11, 4,12**. The results for all ultrathin SnS crystals which correspond to the ROIs shown in **Fig. 4.8a** are presented. The $\chi^{(2)}$ parameter c is calculated through the mean values of b and e using Eq. 7.

| ROI | Zigzag direction θ (°) | Parameter a (arb. units) | Parameter $b = \chi^{(2)}_{yxx} / \chi^{(2)}_{yyy}$ | Parameter e | Quality of fitting | Parameter $c = \chi^{(2)}_{xxy} / \chi^{(2)}_{yyy}$ |
|---|---|---|---|---|---|---|
| 1 | -33.96 | 2.78 | 5.05 | 7.33 | 85 % | 14.84 |
| 2 | -40.35 | 2.57 | 6.16 | 7.15 | 92 % | 18.45 |
| 3 | 40.76 | 2.29 | 16.34 | 8.55 | 91 % | 65.58 |
| 4 | 23.67 | 2.56 | 9.09 | 3.75 | 91 % | 15.17 |
| 5 | 29.25 | 0.30 | 13.05 | 3.77 | 73 % | 22.71 |
| 6 | 29.36 | 0.91 | 12.59 | 3.07 | 56 % | 17.79 |

We have also investigated the reason behind the considerably higher SHG intensity exhibited by one SnS flake (ROI 3) compared to its neighboring ones, as illustrated in **Fig. 4.7 and 4.8a**. We note that the integrated SHG intensity from each SnS flake shown in **Fig. 4.8a** (sum of all SHG

intensities acquired for all the different excitation polarizations ($\varphi \in [0^\circ, 360^\circ)$ with step $2^\circ$) is not polarization dependent anymore, and thus differences in the SHG intensities between the different flakes in the same image could solely be attributed to differences in their number of layers. In order to quantify these differences, **Table 4.3** summarizes the maximum SHG intensities detected in each ROI. We characterized as monolayer the flake with the minimum intensity, i.e., ROI 1. The number of layers *N* for the other flakes is then determined using Eq. 12 ($N = \sqrt{I / I_{ML}}$). We note that ROIs 2, 4-6 could also be characterized as monolayers. Interestingly, the intensity in these ROIs exhibits a variation. This variation may be attributed to the solvent overlayer, which could change the z-positions of the SnS crystals and place them slightly out of focus. This solvent residual is known to affect the measurement of the thickness of liquid phase exfoliated SnS flakes [13]. On the other hand, ROI 3 produces SHG signal approximately nine times higher than its surrounding crystals, as also shown in **Fig. 4.13**, which presents the SHG intensity along the dashed line i shown in **Fig. 4.8a**. The shape and magnitude of the polar diagram of ROI 3 (**Fig. 5d**) fits well to the theoretical predictions of our constructive interference model (Eq. 12). This behavior (the $N^2$ times SHG signal dependency) that appeared in our experimental data, could occur from a non-centrosymmetric, three-layer SnS crystal with AA stacking sequence.

Here we try to address the thickness dependent SHG intensity in the few-layer 2D SnS crystals of our study by introducing a constructive interference model that describes the non-centrosymmetric AA stacking sequence of layered group IV MX crystals (Eq. 12). According to this model each layer contributes constructively in the detected SHG and the total SHG is analogous to $N^2$, where N is the number of layers. However, like other group IV MX compounds (GeS, GeSe, SnSe), a few-layer SnS crystal might also possess antiferroelectric order with alternating left and right polarization in the adjacent layers (i.e. the case of AB stacking sequence). In that case, the odd-layered crystals are non-centrosymmetric and provide SHG, while the even-layered crystals are centrosymmetric and should in principle not produce SHG signals. In our experiments we found a SHG crystal that produces 9 times higher SHG signal than its surrounding crystals and the shape and magnitude of its polar diagram fits well to the theoretical predictions of our constructive interference model (Eq. 12). This behavior (the $N^2$ times SHG signal dependency) that appeared in our experimental data, could occur from a non-centrosymmetric, three-layer SnS crystal with AA stacking sequence.

**Table 4.3.** Summary of the maximum SHG intensity detected for the ultrathin SnS crystals which correspond to the ROIs shown in **Fig. 5a**. As monolayer is characterized the flake with the minimum intensity, i.e., ROI 1, while the number of layers *N* for the other flakes is determined using Eq. 12.

| ROI | Max. SHG intensity (x $10^5$) (arb. units) | Number of layers N |
|---|---|---|
| 1 | 4.7 | 1 |
| 2 | 5.4 | 1.1 |
| 3 | 49 | 3.2 |
| 4 | 5.6 | 1.1 |
| 5 | 8.3 | 1.3 |
| 6 | 5.9 | 1.1 |

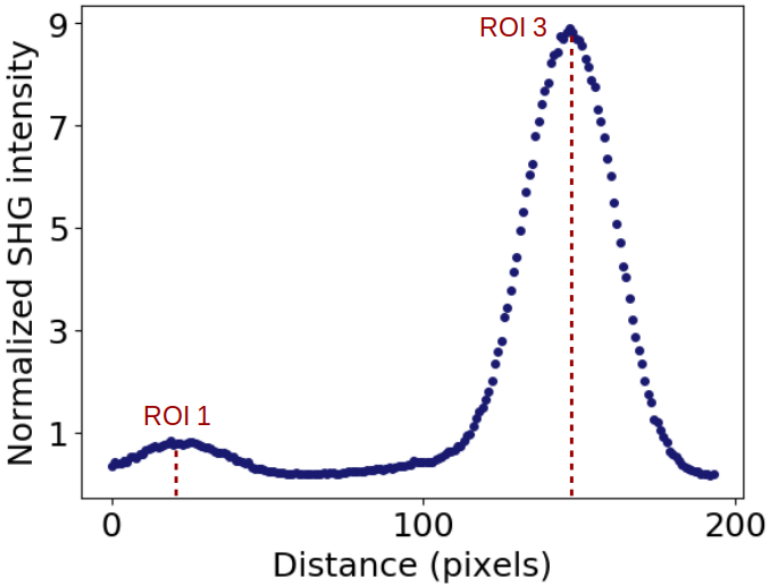


**Figure 4.13.** SHG intensity along the dashed line i shown in **Fig. 4.8a**, normalized to the maximum intensity in ROI 1. The intensity in ROI 3 is found to be nine times higher than that of ROI 1, implying that ROI 3 could be a SnS trilayer.

## 4.3 Methods

### 4.3.1 Nonlinear microscope

Our experimental setup is based on an inverted microscope (Axio Observer Z1, Carl Zeiss), which uses a fs laser (FLINT FL1 Yb Oscillator, ~6 W, 1028 nm, ~76 MHz, 30 fs, Light Conversion) to pump nonlinear optical processes (**Fig. 4.5**). A pair of silver-coated galvanometric (galvo) mirrors

(6215H, Cambridge Technology) guides the laser beam into the microscope, allowing to raster-scan stationary samples. The beam passes through a zero-order half-wave retardation plate (QWPO-1030-10-2, CVI Laser), which is placed in a motorized rotation stage (M-060.DG, Physik Instrumente), with which we can rotate the linear polarization of the excitation field with accuracy of 0.1°. A pair of achromatic lenses suitably expands the beam diameter to fill the back aperture of the objective lens (Plan-Apochromat × 40/1.3 NA, Carl Zeiss).

At the motorized turret box of the microscope, we have the option of using either a silver mirror or a dichroic mirror, both at 45° just below the objective, depending on whether we wish to collect the produced signal in the forward or backwards (epi) detection geometry, respectively. In this work, we collect the signal in the forward direction, using the silver mirror which is insensitive to the laser beam polarization. The objective lens tightly focuses the beam onto the stationary sample that produces SHG, which is collected by a condenser lens (achromatic-aplanatic, 1.4 NA, Carl Zeiss). We then use suitable short-pass (FF01-680/SP, Semrock) and narrow bandpass (FF01-514/3, Semrock) filters to cut off residual laser light and any other unwanted signal. Finally, a linear polarizer (LPVIS100-MP, ThorLabs) is placed before the detector which is based on a photomultiplier tube module (H9305-04, Hamamatsu), in order to select the detected SHG polarization.

The galvanometric mirrors and the photomultiplier tubes are connected to a connector block (BNC-2110, National Instruments Austin), which is interfaced to a PC through a DAQ (PCI 6259, National Instruments). The coordination of the detector recordings with the galvanometric mirrors for the image formation, as well as the movement of the motors, is carried out using LabView (National Instruments).

This setup allows us to record spatially resolved SHG intensity images from a sample region, while rotating the linear polarization of the excitation field, performing P-SHG imaging. Each image (of 500x500 pixels in this work), corresponds to a sample area of size from a few μm to hundreds of μm, depending on how we have set the movement of the galvo mirrors. We also note that our diffraction-limited spatial resolution is approximately 500 nm ($0.61\lambda_{exc}$/NA, with NA=1.3, $\lambda_{exc}$=1028nm). For the data analysis, we used the MATLAB (The Mathworks, Inc) programming language [14], the open-source Python programming language [15], and the open-source ImageJ image analysis software [16].

### 4.3.2 Sample preparation and characterization

The LPE method is employed to isolate an ultrathin layer of SnS sheets. The isolated ultrathin SnS sheets are characterized with UV-Vis spectroscopy, and atomic force microscopy (AFM), and are identified to consist of monolayer and bilayer crystals. Details regarding the sample preparation and characterization can be found in the original publication [17].

## References


[1] S. Psilodimitrakopoulos, L. Mouchliadis, I. Paradisanos, A. Lemonis, G. Kioseoglou, E. Stratakis, *Light Sci. Appl.* **2018**, 7, 18005.

[2] G. M. Maragkakis, S. Psilodimitrakopoulos S, L. Mouchliadis, I. Paradisanos, A. Lemonis, G. Kioseoglou, E. Stratakis, *Opto-Electron Adv* **2019**, 2, 190026.

[3] S. Psilodimitrakopoulos, L. Mouchliadis, I. Paradisanos, G. Kourmoulakis, A. Lemonis, G. Kioseoglou, E. Stratakis, *Sci. Rep.* **2019**, 9, 14285.

[4] S. Psilodimitrakopoulos, A. Orekhov, L. Mouchliadis, D. Jannis, G. M. Maragkakis, G. Kourmoulakis, N. Gauquelin, G. Kioseoglou, J. Verbeeck, E. Stratakis, *npj 2D Mater. Appl.* **2021**, 5, 77.

[5] S. Psilodimitrakopoulos, L. Mouchliadis, G. M. Maragkakis, G. Kourmoulakis, A. Lemonis, G. Kioseoglou, E. Stratakis, *2D Mater.* **2021**, 8, 015015.

[6] L. Mouchliadis, S. Psilodimitrakopoulos, G. M. Maragkakis, I. Demeridou, G. Kourmoulakis, A. Lemonis, G. Kioseoglou, E. Stratakis, *npj 2D Mater. Appl.* **2021**, 5, 6.

[7] E. Hecht, *Optics*, Pearson Education Limited **2017**.

[8] H. Wang and X. Qian, *Nano Lett.* 2017, 17, 5027.

[9] R. W. Boyd, *Nonlinear Optics*, Academic Press, Elsevier **2020**.

[10] W.-T. Hsu, Z.-A. Zhao, L.-J. Li, C.-H. Chen, M.-H. Chiu, P.-S. Chang, Y.-C. Chou, W.-H. Chang, *ACS Nano* **2014**, 8, 2951-2958.

[11] A. Dasgupta, J. Gao, X. Yang, *Laser Photonics Rev.* **2020**, 1900416.

[12] A. Autere, C. R. Ryder, A. Säynätjoki, L. Karvonen, B. Amirsolaimani, R. A. Norwood, N. Peyghambarian, K. Kieu, H. Lipsanen, M. C. Hersam, Z. J. Sun, J. Phys. Chem. Lett. **2017**, 8, 1343.

[13] J. R. Brent, D. J. Lewis, T. Lorenz, E. A. Lewis, N. Savjani, S. J. Haigh, G. Seifert, B. Derby, P. O'Brien, *J. Am. Chem.* Soc. **2015**, 137, 12689–12696.

[14] D. J. Higham, N. J. Higham, *MATLAB guide*, Siam **2016**.

[15] G. van Rossum, Python tutorial, Technical Report CS-R9526, Centrum voor Wiskunde en Informatica (CWI), Amsterdam, May **1995**.

[16] C. A. Schneider, W. S. Rasband, K. W. Eliceiri, *Nature Methods* **2012**, 9, 671-675.

[17] G. M. Maragkakis, S. Psilodimitrakopoulos, L. Mouchliadis, A. S. Sarkar, A. Lemonis, G. Kioseoglou and E. Stratakis, *Adv. Optical Mater.* **2022** 10:2270038.

# Chapter 5 – Anisotropic third harmonic generation in two-dimensional tin sulfide


## Abstract

The in-plane anisotropic properties of 2D group IV monochalcogenides provide an additional degree of freedom which can be useful in future optoelectronic devices. Here, it is shown that the THG signal produced by ultrathin tin (II) sulfide (SnS) is in-plane anisotropic with respect to the incident linear polarization of the laser field. We fit the experimental P-THG measurements with a nonlinear optics model, which accounts for the orthorhombic crystal structure of 2D SnS. Given that the theoretical model consists of five free parameters, we experimentally show that recording and simultaneously fitting both orthogonal components of the P-THG intensity provides better precision in the calculation of the relative magnitudes of the $\chi^{(3)}$ tensor components. Furthermore, we introduce a THG anisotropy ratio, whose calculated values compare the total THG intensity when the excitation linear polarization is along the armchair crystallographic direction with the case when it is along the zigzag direction. Our results provide quantitative information on the anisotropic nature of the THG process in SnS, paving the way to a better understanding of anisotropic nonlinear light-matter interactions, and the development of polarization-sensitive third-order nonlinear optical devices.


## 5.1 Beyond state of the art

In this work, we investigate the P-THG process in ultrathin SnS, produced via liquid phase exfoliation (LPE) [1-6], and characterized with various techniques to contain monolayer and bilayer crystals (see Methods and Materials). Our methodology is based on nonlinear optical imaging, which has been recently demonstrated as a powerful tool to explore the properties of 2D materials [1, 7-12]. With respect to the rotating orientation of the excitation linear polarization, the THG signal is found to be in-plane anisotropic. By using a polarizing beam splitter in front of two orthogonally placed detectors, we simultaneously record the intensity of the parallel and perpendicular polarization components of the THG signal. We then simultaneously fit these two sets

of experimental P-THG measurements to the theoretical model, obtaining a single set of parameter values, allowing us to calculate the relative magnitudes of the $\chi^{(3)}$ tensor components. As we demonstrate, this approach provides increased precision and decreased ambiguity in the above calculation [13], given the fact that the theoretical model contains five free parameters, and thus, several combinations of values could fit into the model. Indeed, the extraction of the third-order coefficients has been reported in literature as a challenging endeavour, in both 2D materials [14] and bio-tissues [15]. We also introduce and calculate a THG anisotropy ratio, which compares the total THG intensity when the excitation linear polarization is along the AC direction, to the THG intensity when the polarization is along the ZZ direction. All the above analysis is performed for different 2D SnS crystals belonging in the same field of view. By using laser raster-scanning and the acquisition of spatially resolved THG intensities, forming images, we obtain the means of direct comparison regarding the anisotropic nonlinear optical response between different SnS crystals. The demonstrated technique is all-optical, minimally invasive and rapid, and can become a useful tool towards fundamental studies and optoelectronic applications of 2D materials with in-plane anisotropy.

## 5.2 Results and discussion

### 5.2.1 Theoretical formulation of P-THG in 2D SnS

The crystal structure of 2D SnS is schematically illustrated in **Fig. 5.1a** [16]. In order to describe the interaction of the laser excitation field with an orthorhombic MX crystal, and the generation of the third harmonic field, we employ the Jones formalism [1, 7-12, 17]. We particularly consider two coordinate systems: the laboratory frame $(X, Y, Z)$, and that defined by the crystal plane $(x, y, z)$, where $z \parallel Z$ (**Fig. 5.1b**). The laser beam propagates along $Z$-axis, normally incident to the crystal, and is linearly polarized along the sample plane, oriented at an angle $\varphi$ with respect to $X$-axis. In the experiment, the angle $\varphi$ is controlled via a rotating half-waveplate. The $x$-axis is considered to be parallel to the AC crystallographic direction and oriented at angle $\theta$ with respect to $X$-axis (**Fig. 5.1b**).

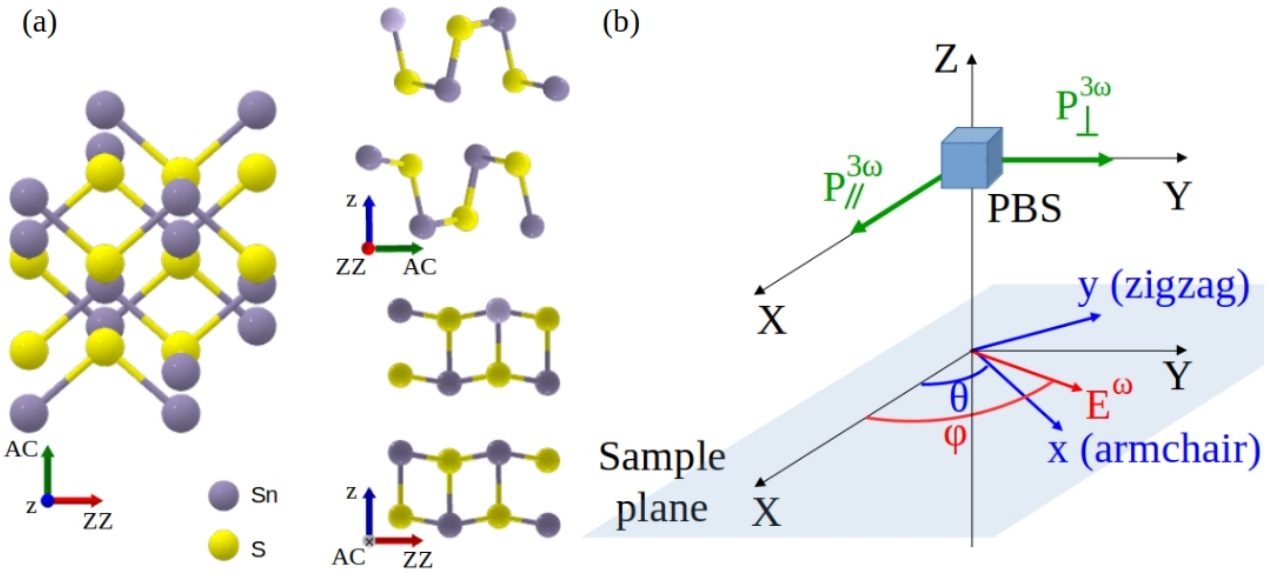


**Figure 5.1.** a) Schematic illustration of the crystal structure of orthorhombic 2D SnS [16]. b) Schematic illustration of the two coordinate systems adopted in our experimental configuration: the laboratory one $(X, Y, Z)$ and the crystal one $(x, y, z)$, where $z$ and $Z$ coincide. The angles $\varphi$ and $\theta$ describe the orientation of the laser field, and the AC crystallographic direction, relative to $X$ laboratory axis, respectively. In the detection path, a polarizing beam splitter (PBS) analyzes the generated THG field into its two orthogonal components, $P_{\parallel}^{3\omega}$ and $P_{\perp}^{3\omega}$.

In our system, the excitation field past the half-wave retardation plate can be expressed in laboratory coordinates by the Jones vector $\begin{pmatrix} E_0 \cos\varphi \\ E_0 \sin\varphi \end{pmatrix}$, where $E_0$ is the amplitude of the electric field. The expression of this vector in crystal coordinates can be derived by multiplying the excitation field with the rotation matrix $\begin{pmatrix} \cos\theta & \sin\theta \\ -\sin\theta & \cos\theta \end{pmatrix}$, giving $E^{\omega} = \begin{pmatrix} E_0 \cos(\varphi-\theta) \\ E_0 \sin(\varphi-\theta) \end{pmatrix}$.

The 2D MXs belong to the orthorhombic point group $C_{2v}$ (mm2), and their contracted third-order nonlinear susceptibility tensor, $\chi^{(3)}$, features the following non-zero elements: $\chi_{11}, \chi_{16}, \chi_{18}, \chi_{22}, \chi_{24}, \chi_{29}, \chi_{33}, \chi_{35}, \chi_{37}$ [18-20]. In this notation, the first subscript refers to: 1: *x*, 2: *y*, 3: *z*, and the second to: 1: *xxx*, 2: *yyy*, 3: *zzz*, 4:*yzz*, 5: *yyz*, 6: *xzz*, 7: *xxz*, 8: *xyy*, 9: *xxy*, 0: *xyz*. As a result, the THG equation is expressed as [18-20]:

$$\begin{pmatrix} P_x^{3\omega} \\ P_y^{3\omega} \\ P_z^{3\omega} \end{pmatrix} = \varepsilon_0 \begin{pmatrix} \chi_{11} & 0 & 0 & 0 & 0 & \chi_{16} & 0 & \chi_{18} & 0 & 0 \\ 0 & \chi_{22} & 0 & \chi_{24} & 0 & 0 & 0 & 0 & \chi_{29} & 0 \\ 0 & 0 & \chi_{33} & 0 & \chi_{35} & 0 & \chi_{37} & 0 & 0 & 0 \end{pmatrix} \begin{pmatrix} E_x^\omega E_x^\omega E_x^\omega \\ E_y^\omega E_y^\omega E_y^\omega \\ E_z^\omega E_z^\omega E_z^\omega \\ 3E_y^\omega E_z^\omega E_z^\omega \\ 3E_y^\omega E_y^\omega E_z^\omega \\ 3E_z^\omega E_z^\omega E_x^\omega \\ 3E_x^\omega E_x^\omega E_z^\omega \\ 3E_y^\omega E_y^\omega E_x^\omega \\ 3E_x^\omega E_x^\omega E_y^\omega \\ 6E_x^\omega E_y^\omega E_z^\omega \end{pmatrix} \quad (1)$$

Considering that the pump laser beam is polarized along the sample plane, i.e., $E_z^\omega = 0$, Eq. 1 is reduced to:

$$\begin{pmatrix} P_x^{3\omega} \\ P_y^{3\omega} \end{pmatrix} = \varepsilon_0 \begin{pmatrix} \chi_{11}\left(E_x^\omega\right)^3 + 3\chi_{18}E_x^\omega\left(E_y^\omega\right)^2 \\ \chi_{22}\left(E_y^\omega\right)^3 + 3\chi_{29}E_y^\omega\left(E_x^\omega\right)^2 \end{pmatrix} \quad (2)$$

and therefore, only terms including four independent $\chi^{(3)}$ elements survive. $\chi_{11}$ and $\chi_{22}$ are known as the on-axis $\chi^{(3)}$ elements [21], where the row number equals the column number, and they represent contributions to the THG signal when all three incident fields are parallel to $x$-axis (AC direction) or $y$-axis (ZZ direction), respectively. On the other hand, $\chi_{18}$ and $\chi_{29}$ are known as the off-axis elements [21], where the row number is not equal to the column number, and they represent contributions to the THG signal when the incident fields are not all parallel to each other.

We then transform Eq. 2 back to laboratory coordinates by multiplying with the rotation matrix $\begin{pmatrix} \cos\theta & -\sin\theta \\ \sin\theta & \cos\theta \end{pmatrix}$, obtaining:

$$\begin{pmatrix} P_X^{3\omega} \\ P_Y^{3\omega} \end{pmatrix} \sim \begin{pmatrix} \left(\chi_{11}\cos^2(\varphi-\theta) + 3\chi_{18}\sin^2(\varphi-\theta)\right)\cos\theta\cos(\varphi-\theta) - \left(\chi_{22}\sin^2(\varphi-\theta) + 3\chi_{29}\cos^2(\varphi-\theta)\right)\sin\theta\sin(\varphi-\theta) \\ \left(\chi_{11}\cos^2(\varphi-\theta) + 3\chi_{18}\sin^2(\varphi-\theta)\right)\sin\theta\cos(\varphi-\theta) + \left(\chi_{22}\sin^2(\varphi-\theta) + 3\chi_{29}\cos^2(\varphi-\theta)\right)\cos\theta\sin(\varphi-\theta) \end{pmatrix}$$

(3)

By using a polarizing beam splitter in front of the detector, we collect the two orthogonal components of the THG field. These components, $P_\parallel^{3\omega} = P_X^{3\omega}$ and $P_\perp^{3\omega} = P_Y^{3\omega}$, can be described by multiplying with the Jones matrix $\begin{pmatrix} \cos^2\zeta & \sin\zeta\cos\zeta \\ \sin\zeta\cos\zeta & \sin^2\zeta \end{pmatrix}$ of a linear polarizer. Here, $\zeta$ is the angle of the transmission axis of the polarizer with respect to $X$-axis, and we set $\zeta = 0^o$ for $P_\parallel^{3\omega}$, and

$\zeta = 90^o$ for $P_{\perp}^{3\omega}$, i.e., axis of transmission parallel to $X$ and $Y$-axis, respectively. Then, the intensities of these two orthogonal THG components, $I_{\parallel}^{3\omega} = \left|P_{\parallel}^{3\omega}\right|^2$ and $I_{\perp}^{3\omega} = \left|P_{\perp}^{3\omega}\right|^2$, are calculated to be:

$$I_{\parallel}^{3\omega} \sim \left[\left(\chi_{11}\cos^2(\varphi-\theta)+3\chi_{18}\sin^2(\varphi-\theta)\right)\cos\theta\cos(\varphi-\theta)-\left(\chi_{22}\sin^2(\varphi-\theta)+3\chi_{29}\cos^2(\varphi-\theta)\right)\sin\theta\sin(\varphi-\theta)\right]^2$$

(4)

$$I_{\perp}^{3\omega} \sim \left[\left(\chi_{11}\cos^2(\varphi-\theta)+3\chi_{18}\sin^2(\varphi-\theta)\right)\sin\theta\cos(\varphi-\theta)+\left(\chi_{22}\sin^2(\varphi-\theta)+3\chi_{29}\cos^2(\varphi-\theta)\right)\cos\theta\sin(\varphi-\theta)\right]^2$$

(5)

These relationships are expressed in terms of the absolute values of the $\chi^{(3)}$ tensor elements. Instead, they can be expressed in terms of dimensionless ratios of the $\chi^{(3)}$ tensor elements, namely:

$$I_{\parallel}^{3\omega} = a\left[\left(\cos^2(\varphi-\theta)+3b\sin^2(\varphi-\theta)\right)\cos\theta\cos(\varphi-\theta)-\left(c\sin^2(\varphi-\theta)+3d\cos^2(\varphi-\theta)\right)\sin\theta\sin(\varphi-\theta)\right]^2$$

(6)

$$I_{\perp}^{3\omega} = a\left[\left(\cos^2(\varphi-\theta)+3b\sin^2(\varphi-\theta)\right)\sin\theta\cos(\varphi-\theta)+\left(c\sin^2(\varphi-\theta)+3d\cos^2(\varphi-\theta)\right)\cos\theta\sin(\varphi-\theta)\right]^2 \quad (7)$$

where:

$$b = \chi_{18}/\chi_{11},\ c = \chi_{22}/\chi_{11},\ d = \chi_{29}/\chi_{11} \quad (8)$$

are the relative magnitudes of the $\chi^{(3)}$ tensor components, and $\alpha$ is a multiplication factor that depends on the square of the $\chi^{(3)}$ tensor element $\chi_{11}$, and the amplitude of the electric field.

The total P-THG intensity can then be obtained through:

$$I^{3\omega} = I_{\parallel}^{3\omega} + I_{\perp}^{3\omega} \quad (9)$$

We then present numerical simulations of the theoretical P-THG intensities $I_{\parallel}^{3\omega}$ and $I_{\perp}^{3\omega}$, produced by a 2D MX, described by Eqs. 6 and 7, respectively. In particular, in **Figs. 5.2-5.5**, we plot these P-THG modulations in polar diagrams, as function of the orientation of the linearly polarized excitation angle φ, for different values of the parameters of the model, aiming to, additionally, investigate their effect. Namely, we vary the relative magnitudes of the $\chi^{(3)}$ tensor components b (**Fig. 5.2**), c (**Fig. 5.3**) and d (**Fig. 5.4**), and the AC direction θ (**Fig. 5.5**). In **Figs. 5.2-5.4**, we vary only one ratio of the $\chi^{(3)}$ tensor components as reported in each figure, while keeping the rest ratios fixed to the average values we have eventually, experimentally calculated from our analysis, reported in **Table 5.1**, and while keeping the AC direction θ fixed to 50°. In **Fig. 5.5**, we vary the AC angle θ, while again keeping the $\chi^{(3)}$ tensor components fixed to the average values reported in **Table 5.1**.

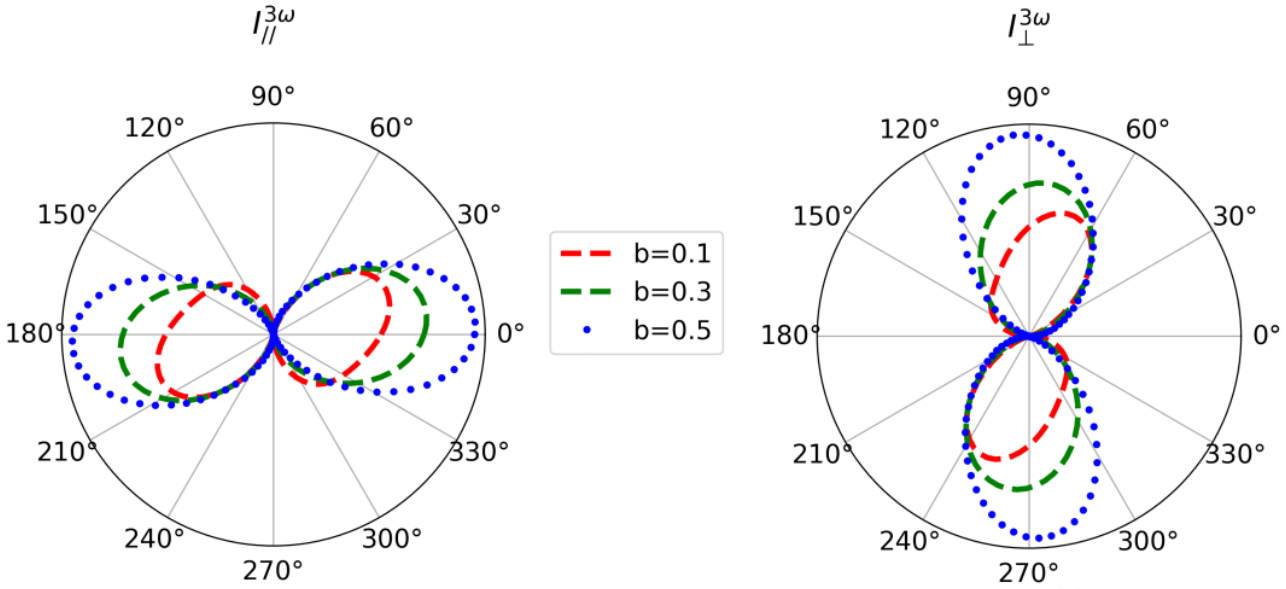


**Figure 5.2.** Numerical simulations on the effect of different values of the $\chi^{(3)}$ tensor ratio b (defined by Eq. 8) on the P-THG intensity components produced by a MX, described by Eqs. 6 and 7. We plot $I_{\parallel}^{3\omega}$ (left) and $I_{\perp}^{3\omega}$ (right), in polar diagrams, as function of the orientation of the linearly polarized excitation angle φ.

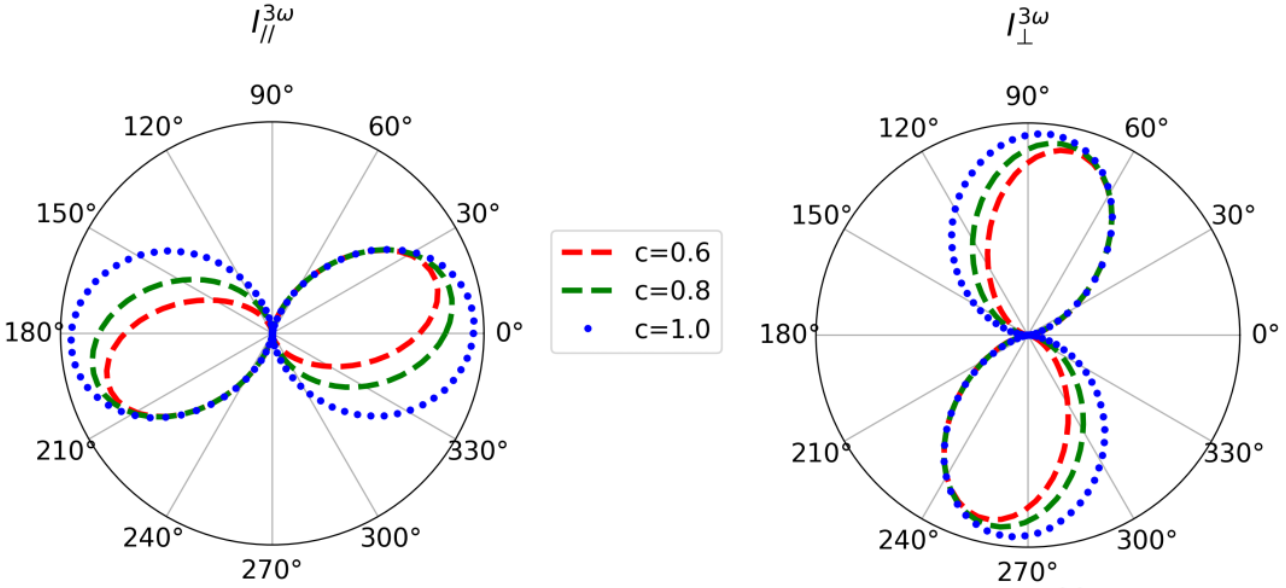


**Figure 5.3.** Numerical simulations on the effect of different values of the $\chi^{(3)}$ tensor ratio c (defined by Eq. 8) on the P-THG intensity components produced by a MX, described by Eqs. 6 and 7. We plot $I_{\parallel}^{3\omega}$ (left) and $I_{\perp}^{3\omega}$ (right), in polar diagrams, as function of the orientation of the linearly polarized excitation angle φ.

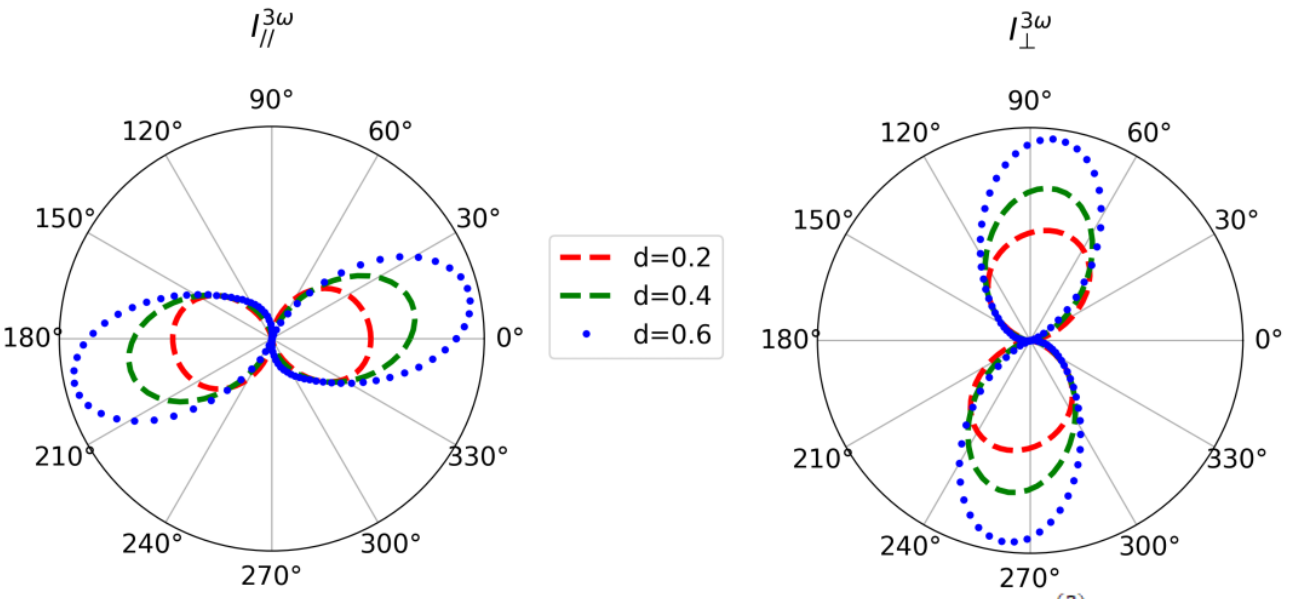


**Figure 5.4.** Numerical simulations on the effect of different values of the $\chi^{(3)}$ tensor ratio d (defined by Eq. 8) on the P-THG intensity components produced by a MX, described by Eqs. 6 and 7. We plot $I_{\parallel}^{3\omega}$ (left) and $I_{\perp}^{3\omega}$ (right), in polar diagrams, as function of the orientation of the linearly polarized excitation angle φ.

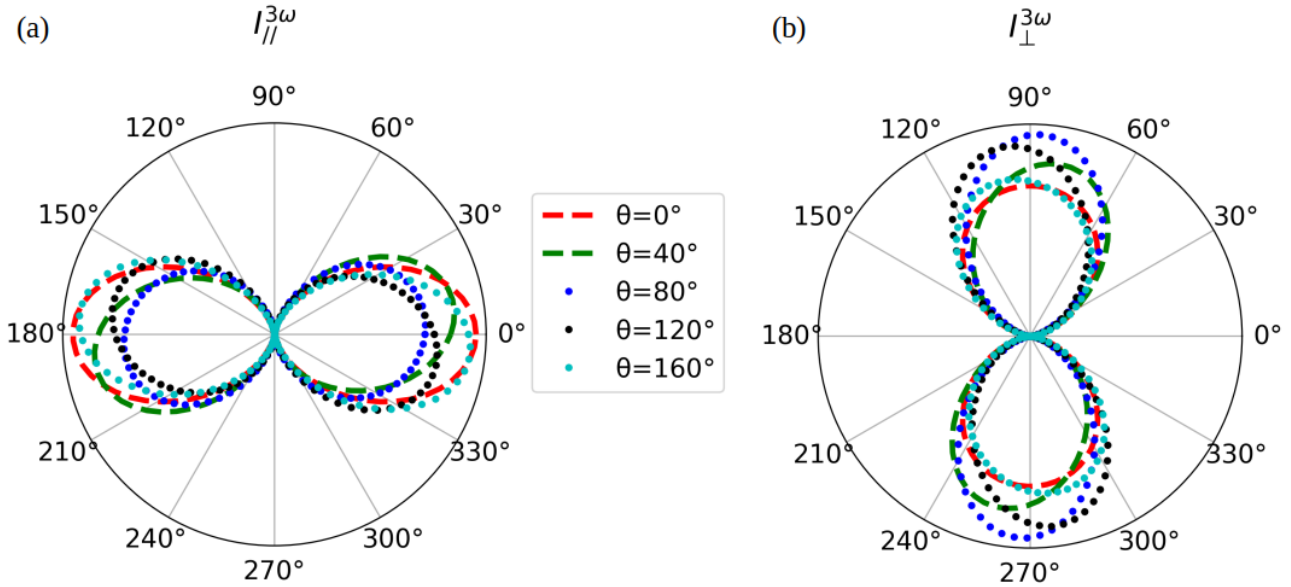


**Figure 5.5.** Numerical simulations on the effect of different values of the AC angle θ on the P-THG intensity components produced by a MX, described by Eqs. 6 and 7. We plot a) $I_{\parallel}^{3\omega}$ and b) $I_{\perp}^{3\omega}$, in polar diagrams, as function of the orientation of the linearly polarized excitation angle φ.

The two P-THG intensity components are predicted to exhibit two-lobe patterns. It is noted that for specific values of these parameters, a change from a two-lobe to a four-lobe pattern could, in principle, be observed (green line in **Fig. 5.10**). Furthermore, we find that for different values of

these parameters, the shapes of the P-THG modulations change. Considering that $I_{\parallel}^{3\omega}$ and $I_{\perp}^{3\omega}$ are found to be sensitive to changes of the values of the relative magnitudes of the $\chi^{(3)}$ tensor components b, c and d, we conclude that we can calculate the values of these quantities, upon measuring the two P-THG intensity components and subsequent fitting to the above nonlinear optics model.

The dependency of the two P-THG intensity components to the parameters of the model, namely θ, b, c and d, constitutes a direct link between the P-THG properties and the in-plane anisotropy of orthorhombic MXs. To account for such anisotropy, we introduce a THG anisotropy ratio (AR), which compares the total THG intensities for incident field polarization along the AC and ZZ crystallographic directions, as:

$$AR=\frac{I_{ZZ}^{3\omega}}{I_{AC}^{3\omega}} \quad (10)$$

For $\varphi=\theta$, i.e., when the linear polarization of the incident field coincides with the AC direction, we obtain $I_{AC}^{3\omega}\sim\chi_{11}^{2}$. On the other hand, for $\varphi=\theta+90^{o}$, i.e., when the linear polarization of the incident field coincides with the ZZ direction, we obtain $I_{ZZ}^{3\omega}\sim\chi_{22}^{2}$. Therefore Eq. 10 gives:

$$AR=\frac{I_{ZZ}^{3\omega}}{I_{AC}^{3\omega}}=\left(\frac{\chi_{22}}{\chi_{11}}\right)^{2}=c^{2} \quad (11)$$

an expression that correlates the AR with the $\chi^{(3)}$ tensor ratio $c$, which is defined in Eq. 8.

We also note that the produced THG field is also linearly polarized at an angle $\theta_{THG}$ given by:

$$\theta_{THG}=\tan^{-1}\left\{\frac{\chi_{22}\tan^{2}(\varphi-\theta)+3\chi_{29}}{\chi_{11}+3\chi_{18}\tan^{2}(\varphi-\theta)}\tan(\varphi-\theta)\right\} \quad (12)$$

which for the special case of $\varphi=\theta+45^{o}$ yields:

$$\theta_{THG}=\tan^{-1}\left\{\frac{\chi_{22}+3\chi_{29}}{\chi_{11}+3\chi_{18}}\right\} \quad (13)$$

Consequently, by using Eq. 12, we could, in principle, calculate the direction $\theta_{THG}$ of the linear polarization of the THG field.

## 5.2.2 Experimental P-THG imaging

In **Fig. 5.6a**, we present a schematic illustration of the experimental setup, used for P-THG imaging of ultrathin SnS (see Methods and Materials for a detailed description of the setup, as well as the

sample preparation and characterization). In particular, a fs laser beam is focused onto the sample under study, while a pair of galvanometric mirrors is used for laser raster-scanning over the sample area. We record spatially resolved THG images while rotating the angle of the linear polarization of the fundamental beam. In the detection path, we have used a polarizing beam splitter cube, coupled with two orthogonally placed detectors (see **Fig. 5.6b** for an actual photograph). Based on this experimental configuration, we simultaneously record the intensity of the two orthogonal THG field components, in a single shot.

In the inset in **Fig. 5.6a**, we present the power-law dependence of the THG intensity produced by an ultrathin SnS crystal, as function of the excitation laser power. The slope 3, in the double log-scale plot, confirms the THG process [14, 19, 21-26].

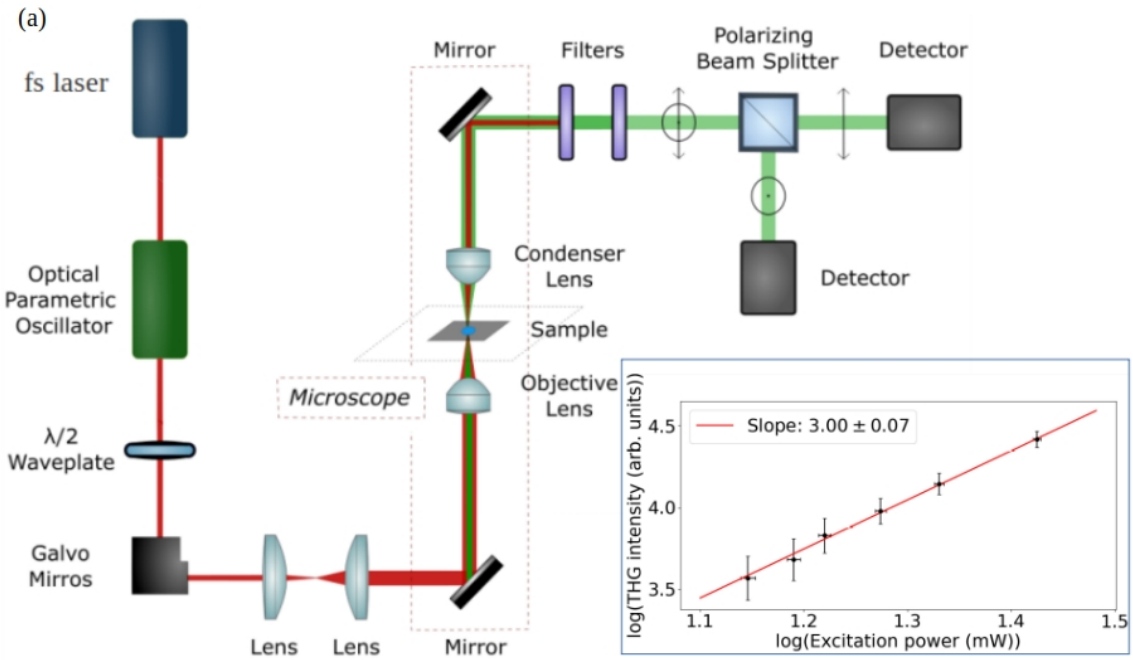


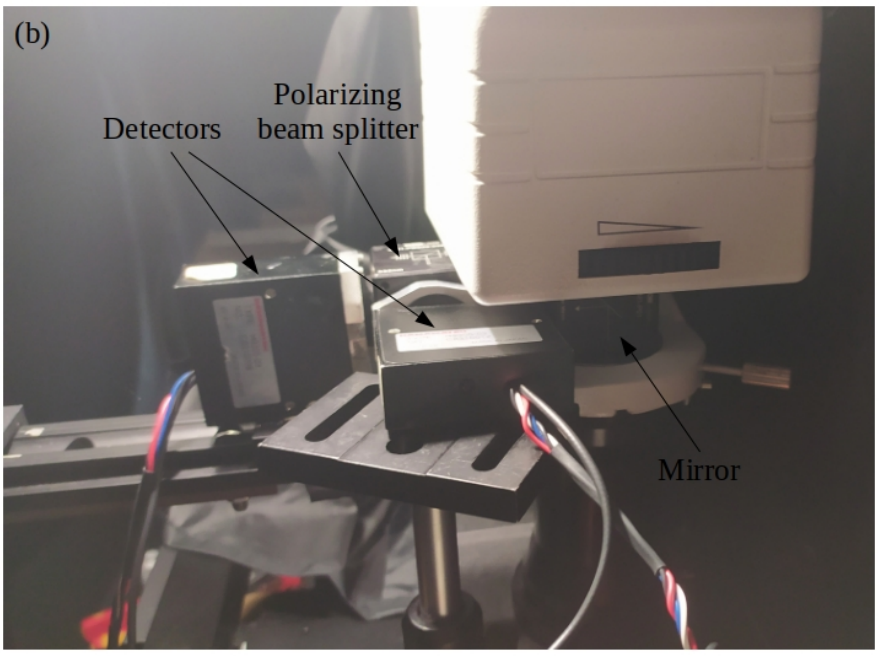

**Figure 5.6.** a) Schematic illustration of the nonlinear optical setup, which is based on a fs laser beam coupled to a microscope. The fundamental, 1028 nm, pulses are converted to 1542 nm, by means of an optical parametric oscillator. 2D SnS crystals, excited by the laser beam, generate third harmonic radiation centered at 514 nm. The THG signal is recorded while changing the angle of the linear polarization of the excitation beam, via a rotating half-wave plate, performing P-THG imaging. A pair of galvanometric mirrors enables raster-scanning of stationary SnS crystals, obtaining THG images of the sample area. The THG signal passes through a polarizing beam splitter, allowing the simultaneous measurement of the intensity of the two orthogonal components of the THG field. Inset: Log-scale plot of the THG intensity, produced by an ultrathin SnS crystal, as function of the incident pump power. Black points with the error bars represent the experimental data, and the red line the linear fitting. b) Actual photograph of part of the nonlinear optical setup.

In **Fig. 5.7**, we present a series of images of the intensity of the parallel THG component, $I_{\parallel}^{3\omega}$, produced by ultrathin SnS crystals in the same field of view, recorded while rotating the pump linear polarization angle $\varphi$, indicated by the orange arrow. As can be observed, the THG signals modulate upon $\varphi$ variation. In the supplementary information of the original publication, there are available two videos (video S1 for $I_{\parallel}^{3\omega}$, and video S2 for $I_{\perp}^{3\omega}$), showing all ninety THG images recorded, with $\varphi \in [0^{\circ}, 360^{\circ})$ with step of $4^{\circ}$. We mark four regions of interest (ROIs) containing ultrathin SnS crystals. Additionally, we have studied two more similar crystals in a different field of view, namely ROIs 5 and 6 shown in **Fig. 5.8**, for a total sample of six ultrathin SnS crystals under study.

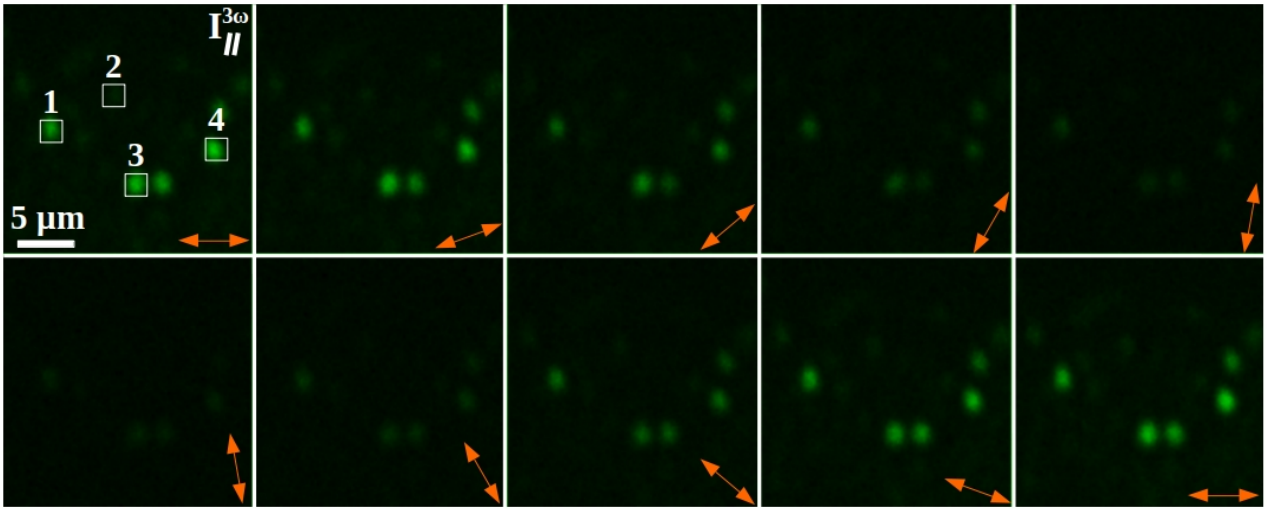

**Figure 5.7.** Experimental P-THG images of ultrathin SnS crystals belonging in the same field of view. Particularly, we present the intensity of the parallel component of the THG field, $I_{\parallel}^{3\omega}$, for different values of the orientation φ of the linearly polarized excitation field, illustrated by the orange arrows. The value of $\varphi$ is varied from 0° to 180° with step of 20°. We mark four ROIs corresponding to ultrathin SnS crystals. Brighter color indicates higher THG intensity.

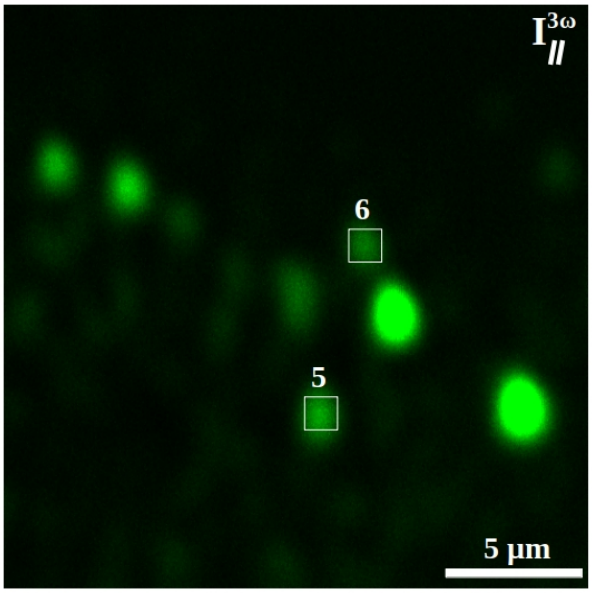


**Figure 5.8.** Sum of all ninety collected P-THG intensity images of $I_{\parallel}^{3\omega}$, for all orientations φ of the excitation linear polarization, corresponding to a field of view containing ultrathin SnS crystals. The two crystals we have focused in our analysis are marked. Brighter color indicates higher THG intensity.

In **Figs. 5.9a, b**, we present, for the field of view shown in **Fig. 5.7**, the sum of all ninety collected THG intensity images of $I_{\parallel}^{3\omega}$ and $I_{\perp}^{3\omega}$, respectively. In **Figs. 5.9c, d**, we plot, in polar diagrams, the modulation of $I_{\parallel}^{3\omega}$ and $I_{\perp}^{3\omega}$, respectively, for the SnS crystals in ROIs 1 and 3, as function of the angle φ of the linear polarization of the excitation beam. The two P-THG intensity components are found to exhibit two-lobe patterns, complying with the theoretical prediction. Furthermore, it is evident that these two SnS crystals produce different P-THG modulations (the one is rotated with respect to the other), in accordance with the theoretical prediction. This difference is the signature of nonlinear optical anisotropy between the two crystals.

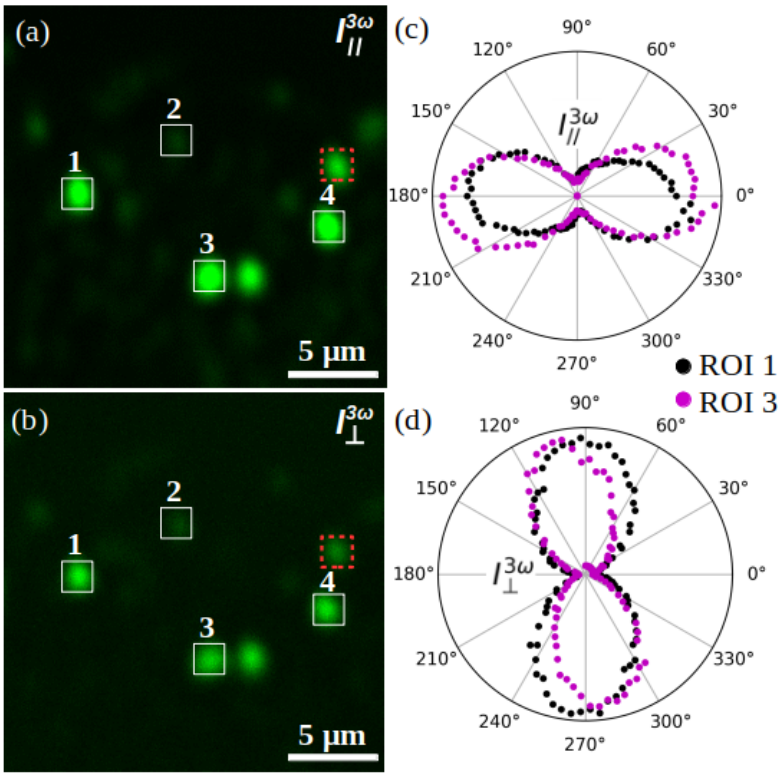


**Figure 5.9.** Sum of a) $I_{\parallel}^{3\omega}$ and b) $I_{\perp}^{3\omega}$ P-THG intensities, for all orientations φ of the excitation linear polarization, corresponding to the field of view shown in **Fig. 5.7**. We mark the four ROIs we have focused in our analysis, corresponding to ultrathin SnS crystals present in the same field of view. Brighter color indicates higher THG intensity. Experimental polar plots of c) $I_{\parallel}^{3\omega}$ and d) $I_{\perp}^{3\omega}$ P-THG intensities as function of the angle $\varphi$, comparing the P-THG modulations in ROI 1 (in black) and ROI 3 (in magenta).

### 5.2.3 Experimental fitting analysis

We then fit the P-THG experimental data with our theoretical model, to extract the relative magnitudes of the $\chi^{(3)}$ tensor components, b, c and d. It is important to note that fitting only one P-THG intensity component (either $I_{\parallel}^{3\omega}$ or $I_{\perp}^{3\omega}$) is not sufficient to obtain reliable fitting results. This is clearly demonstrated in **Fig. 5.10**, where, for ROI 3, we have fitted only one intensity component, namely $I_{\perp}^{3\omega}$ with Eq. 7, and then tested the fitting values to the other component, namely $I_{\parallel}^{3\omega}$ through Eq. 6. It is observed that although there is a set of parameter values that fit very well $I_{\perp}^{3\omega}$ (quality of

fitting 99.3%), the same set does not fit $I_{\parallel}^{3\omega}$ (quality of fitting 32.2%), producing a four-lobe pattern instead of a two-lobe one. It is noted that the white square, shown in the THG images on the left in **Fig. 5.10**, presents a region without SnS crystals, whose intensity has been considered as noise and has been subtracted from our measurements, following the methodology adopted generally here.

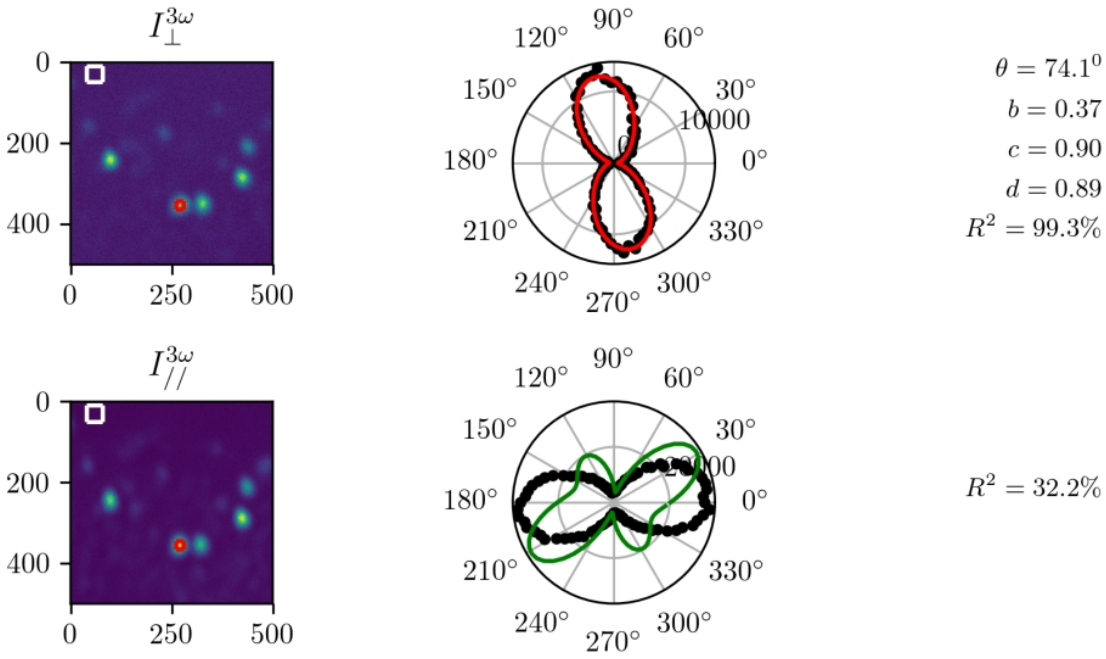


**Figure 5.10.** Example showing experimentally that fitting only one P-THG intensity component (either $I_{\parallel}^{3\omega}$ or $I_{\perp}^{3\omega}$) is not sufficient to obtain reliable fitting results. On the left, we present THG images from the same field of view (the same shown in **Fig. 5.9**), where the THG intensity is integrated for all orientations φ of the excitation linear polarization. In the polar plots (center), black points represent the experimental P-THG data, for the SnS crystal shown with the red square (ROI 3). Here we have fitted $I_{\perp}^{3\omega}$ with Eq. 7 (red curve), and then we have tested the fitting parameter values (reported on the right) on $I_{\parallel}^{3\omega}$, through Eq. 6 (green curve). Although this set of fitting parameter values fits very well the one component (quality of fitting 99.3%), it does not fit the other (quality of fitting 32.2%), producing a four-lobe pattern instead of a two-lobe one.

In this work, we have resolved this issue, by simultaneously fitting both $I_{\parallel}^{3\omega}$ and $I_{\perp}^{3\omega}$, obtaining one set of parameter values, with quality of fitting, $R^2$, equal to the average ($R^2 = \left(R_{\parallel}^2 + R_{\perp}^2\right)/2$. It is noted that all of the experimental fitting results presented here exhibit average quality of fitting larger than 85%. We also note that the whole procedure of loading and simultaneously fitting both experimental datasets, for an individual crystal, requires less than one minute, rendering our methodology a rapid

characterization tool (see also Methods and Materials for the data analysis). Following the above approach, in **Figs. 5.11, 5.12**, we present the simultaneous fitting to both P-THG intensity components, for all six ultrathin SnS crystals under study. The agreement between the experimental data and the theoretical fitting is remarkable.

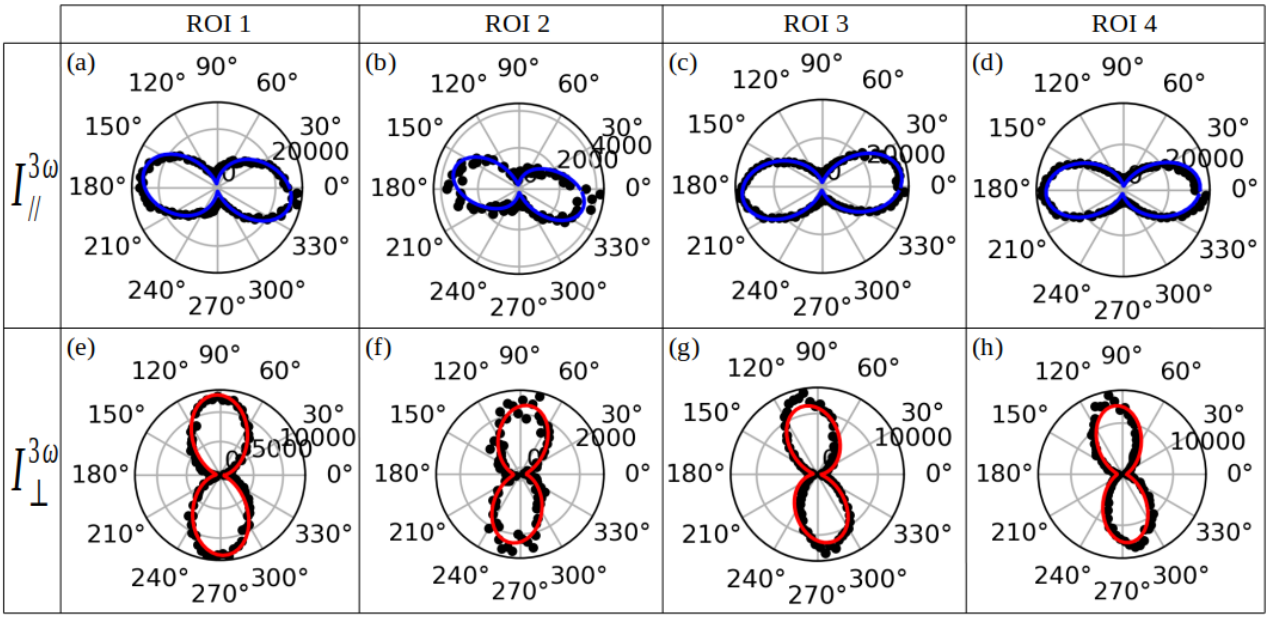


**Figure 5.11**. Experimental P-THG intensity modulations, $I_{\parallel}^{3\omega}$ and $I_{\perp}^{3\omega}$, as function of the linearly polarized excitation angle $\varphi$, presented in polar plots, for the ultrathin SnS crystals 1-4, corresponding to the ROIs marked in **Fig. 5.9**. Black points represent the experimental data, while the blue and red lines represent the simultaneous fitting with Eqs. 6 ($I_{\parallel}^{3\omega}$) and Eq. 7 ($I_{\perp}^{3\omega}$), respectively. Using this fitting process, we are able to calculate the relative magnitudes of the $\chi^{(3)}$ tensor components, for each case, summarized in **Table 5.1**.

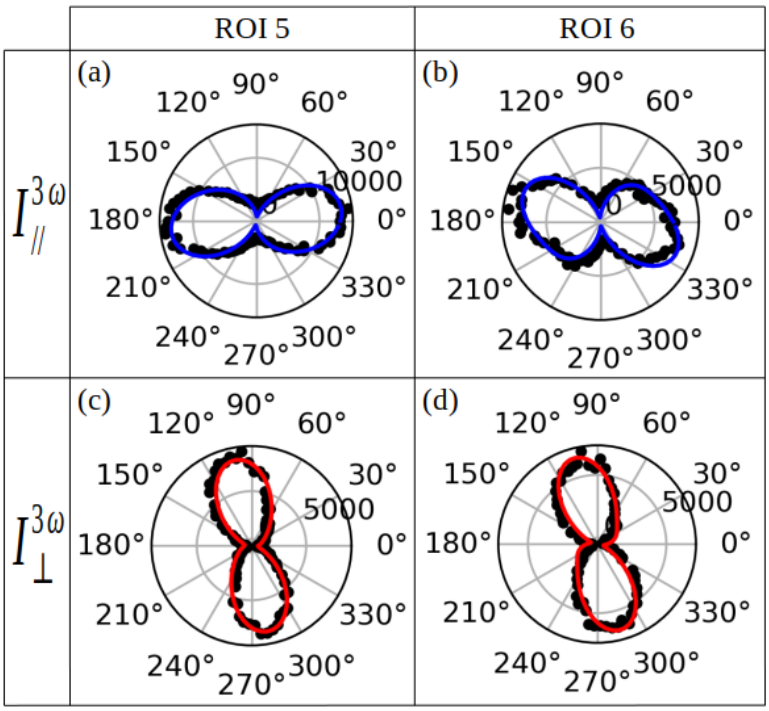

**Figure 5.12.** Experimental P-THG intensity modulations, $I_{\parallel}^{3\omega}$ and $I_{\perp}^{3\omega}$, as function of the linearly polarized excitation angle φ, presented in polar plots, for the ultrathin SnS crystals 5 and 6, corresponding to the ROIs marked in **Fig. 5.8**. Black points represent the experimental data, while the blue and red lines represent the simultaneous fitting with Eq. 6 ($I_{\parallel}^{3\omega}$) and Eq. 7 ($I_{\perp}^{3\omega}$), respectively. With this fitting, we are able to calculate the relative magnitudes of the $\chi^{(3)}$ tensor components, b, c and d, for each case, summarized in **Table 5.1**.

**In Table 5.1**, we summarize the fitting values for the relative magnitudes of the $\chi^{(3)}$ tensor components, for each SnS crystal under study. We also report the average values based on this sample of crystals, along with the standard deviation (std) values, as the errors of the average values. In order to obtain a graphical perspective of these average results, in **Fig. 5.13**, we plot them as Gaussian distributions, with the μ and σ Gaussian parameters equal to the average and std values, respectively.

**Table 5.1.** Summary of the values of the relative magnitudes of the $\chi^{(3)}$ tensor components, b, c and d, which we have experimentally calculated by simultaneously fitting both P-THG intensity components, $I_{\parallel}^{3\omega}$ and $I_{\perp}^{3\omega}$, with Eqs. 6 and 7, respectively. We present results for the ultrathin SnS crystals 1-6, corresponding to the ROIs marked in **Figs. 5.7, 5.8**. The average values, along with the std values, as the errors of the average values, are also reported.

| Crystal | $b = \chi_{18}/\chi_{11}$ | $c = \chi_{22}/\chi_{11}$ | $d = \chi_{29}/\chi_{11}$ |
|---|---|---|---|
| 1 | 0.27 ± 0.02 | 0.99 ± 0.02 | 0.46 ± 0.02 |
| 2 | 0.40 ± 0.02 | 0.93 ± 0.03 | 0.49 ± 0.03 |
| 3 | 0.46 ± 0.02 | 1.00 ± 0.03 | 0.40 ± 0.02 |
| 4 | 0.21 ± 0.02 | 0.65 ± 0.05 | 0.16 ± 0.01 |
| 5 | 0.16 ± 0.02 | 0.74 ± 0.03 | 0.20 ± 0.01 |
| 6 | 0.09 ± 0.01 | 0.82 ± 0.02 | 0.40 ± 0.02 |
| Average | 0.26 ± 0.13 | 0.86 ± 0.13 | 0.35 ± 0.13 |

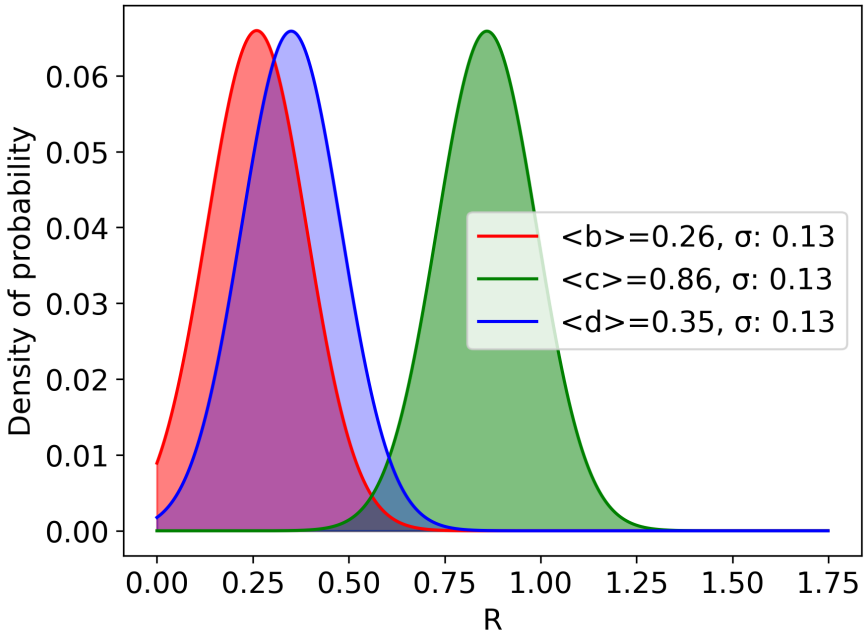


**Figure 5.13.** Graphical representation of the average values we have experimentally calculated for the relative magnitudes of the $\chi^{(3)}$ tensor components, b, c and d, which are here denoted by R. These average values, reported in **Table 5.1**, are plotted here as Gaussian distributions, with the μ and σ Gaussian parameters equal to the average and std values, respectively.

The results of **Table 5.1** indicate the anisotropic nature of the $\chi^{(3)}$ tensor and the THG process in ultrathin SnS crystals. We conclude that the on-axis nonlinear susceptibility tensor elements, $\chi_{11}$ and $\chi_{22}$, are found to be considerably larger with respect to the off-axis elements, $\chi_{18}$ and $\chi_{29}$. These experimental results could be useful in future theoretical studies to evaluate or constrain theoretical models for THG in MXs.

It is noted that the values of the relative magnitudes of the $\chi^{(3)}$ tensor components exhibit variations among different crystals. Such variations have also been observed in other 2D materials, and have been attributed to deformation or defects in the crystal lattice, introduced during the exfoliation process [19, 21, 25].

For reference, in **Table 5.2**, we present a summary of literature reports, to our knowledge, with experimental results on the relative magnitudes of the $\chi^{(3)}$ tensor components, for other 2D

materials. We observe that our conclusions are in qualitative agreement with most literature findings.

**Table 5.2.** Summary of literature reports, to our knowledge, with experimental results on the relative magnitudes of the $\chi^{(3)}$ tensor components, for other 2D materials [14, 19, 21, 22, 24, 25]. [*] For GeSe and GeAs, the values we present here are the average values we have calculated based on a sample of two [19] and seven [25] crystals, respectively, which are reported in the corresponding studies (along with the std values as the errors of the average values).

| Crystal | Crystal structure | $b = \chi_{18}/\chi_{11}$ | $c = \chi_{22}/\chi_{11}$ | $d = \chi_{29}/\chi_{11}$ |
|---|---|---|---|---|
| SnS [This work] | Orthorhombic | 0.26 ± 0.13 | 0.86 ± 0.13 | 0.35 ± 0.13 |
| GeSe [Ref. 19] [*] | Orthorhombic | 0.26 ± 0.01 | 0.54 ± 0.06 | 0.4 ± 0.1 |
| Black phosphorus [Ref. 22] | Orthorhombic | 0.46 | 0.5 | 0.35 |
| Black phosphorus [Ref. 14] | Orthorhombic | Almost zero | Comparable with d | Comparable with c |
| SiP [Ref. 24] | Orthorhombic | - | 0.72 ± 0.08 | - |
| GeAs [Ref. 25] [*] | Monoclinic | 0.21 ± 0.04 | 0.48 ± 0.04 | 0.19 ± 0.01 |
| $As_2S_3$ [Ref. 21] | Monoclinic | 0.29 | 0.60 | 0.29 |

In **Fig. 5.14**, we present both P-THG intensity components, together with the total P-THG intensity, $I^{3\omega}=I_{\parallel}^{3\omega}+I_{\perp}^{3\omega}$, for the ultrathin SnS crystal which corresponds to the red dashed square shown in **Fig. 5.9**. In **Fig. 5.15**, we present the corresponding polar diagram for ROI 4 shown in **Fig. 5.9**. The $I_{\parallel}^{3\omega}$ and $I_{\perp}^{3\omega}$ experimental data are simultaneously fitted with Eqs. 6 and 7, respectively, while the $I^{3\omega}$ data are fitted with Eq. 9. The total P-THG intensity is found to be clearly anisotropic. Specifically, different angles φ of the excitation linear polarization produce different THG intensities. Therefore, the above result confirms the in-plane anisotropic nature of the THG process in ultrathin SnS crystals. Furthermore, it offers the possibility of controlling the emitted THG intensity by tuning the angle φ.

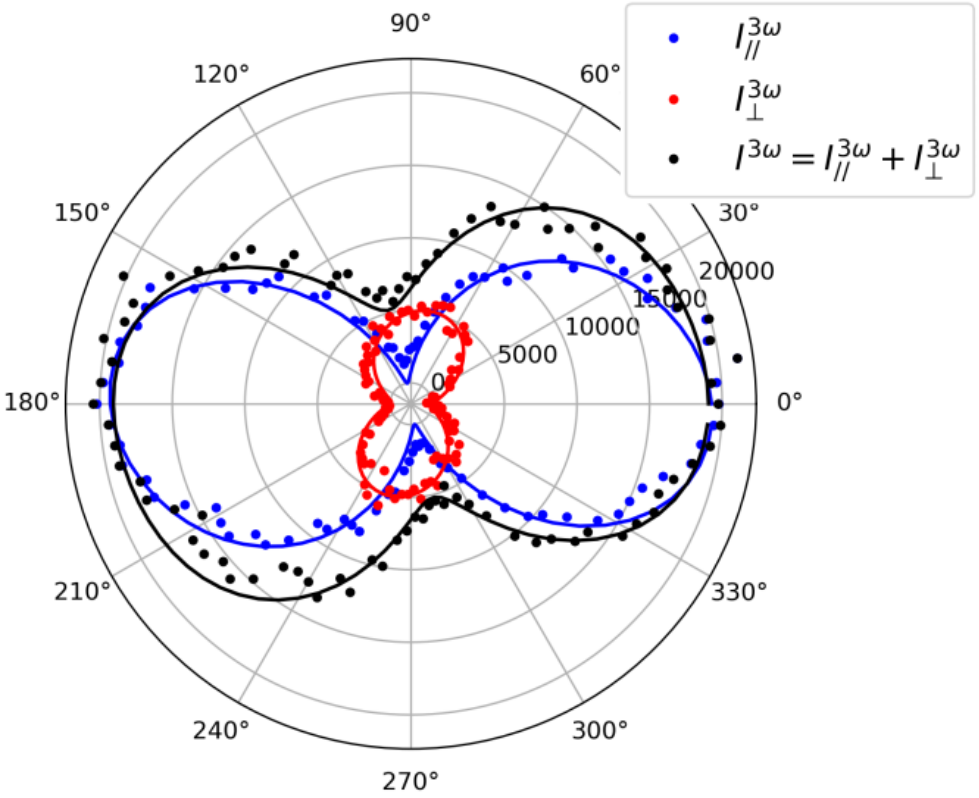


**Figure 5.14**. Experimental P-THG intensity modulations as function of the linearly polarized excitation angle φ, presented in a polar plot, for the ultrathin SnS crystal which corresponds to the red dashed square shown in **Fig. 9**. Blue and red points represent $I_{\parallel}^{3\omega}$ and $I_{\perp}^{3\omega}$, respectively, while the black points represent the total P-THG intensity, $I^{3\omega}=I_{\parallel}^{3\omega}+I_{\perp}^{3\omega}$. The solid curves represent the respective theoretical fittings, with Eqs. 6, 7 and 9.

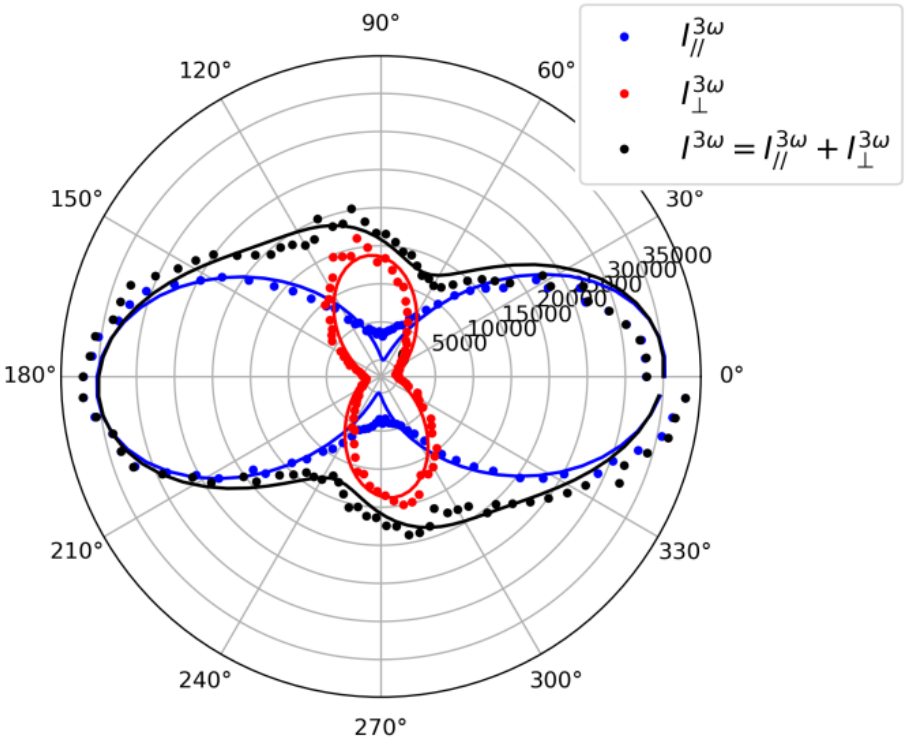


**Figure 5.15**. Experimental P-THG intensity modulations as function of the linearly polarized excitation angle φ, presented in a polar plot, for the ultrathin SnS crystal which corresponds to ROI 4 shown in **Fig. 5.9**. Blue and red points represent $I_{\parallel}^{3\omega}$ and $I_{\perp}^{3\omega}$, respectively, while the black points represent the total P-THG intensity, $I^{3\omega} = I_{\parallel}^{3\omega} + I_{\perp}^{3\omega}$. The solid curves represent the respective theoretical fittings, with Eqs. 6, 7 and 9.

### 5.2.4 THG anisotropy ratio

Furthermore, through Eq. 10, we have introduced a THG AR, which compares the total THG intensities for incident field polarization along the main crystallographic axes AC and ZZ. This AR has been correlated with the $\chi^{(3)}$ tensor ratio c, through Eq. 11, and thus, can be directly calculated using the fitting results of c, reported in **Table 5.1**. The results are summarized in **Table 5.3**, for each ultrathin SnS crystal under study. The AR is found to be, on average, not equal to unity, suggesting that the total THG intensity is not equal when the excitation is along the AC direction compared to the case when it is along the ZZ direction. The above result further confirms the in-plane anisotropic nature of the THG process in ultrathin SnS. Furthermore, this AR allows to compare and classify different orthorhombic 2D materials, based on their degree of nonlinear optical anisotropy.

**Table 5.3.** Summary of the values we have experimentally calculated for the AR, through Eq. 11. We present results for the ultrathin SnS crystals 1-6, corresponding to the ROIs marked in **Figs. 5.7, 5.8**. The average value, along with the std value, as the error of the average value, is also reported.

| Crystal | Anisotropy ratio (AR) |
|---|---|
| 1 | 0.98 ± 0.04 |
| 2 | 0.86 ± 0.06 |
| 3 | 1.00 ± 0.06 |
| 4 | 0.42 ± 0.07 |
| 5 | 0.55 ± 0.04 |
| 6 | 0.67 ± 0.03 |
| Average | 0.75 ± 0.22 |

## 5.3 Methods and materials

### 5.3.1 Nonlinear optical imaging setup and analysis

The nonlinear optical imaging setup is based on a fs laser beam coupled to a microscope (**Fig. 5.6**). The 1028 nm fs laser beam (FLINT FL1 Yb Oscillator, 1028 nm, ≈76 MHz, ≈36 fs, Light Conversion) passes through an optical parametric oscillator (APE Levante IR) which converts it to 1542 nm. The angle of the linear polarization of the excitation field is rotated, performing P-THG imaging, using an achromatic half-wave plate (AHWP10M-1600, Thorlabs), placed in a motorized rotation stage. The beam is guided into an inverted microscope (Axio Observer Z1, Carl Zeiss) by a pair of silver-coated galvanometric (galvo) mirrors (6215H, Cambridge Technology), allowing to raster-scan stationary samples. A pair of achromatic doublet lenses suitably expands the beam diameter to fill the back aperture of the objective lens (Plan-Apochromat 20×/0.8 NA, Carl Zeiss).

At the motorized turret box of the microscope, at 45° just below the objective lens, a silver mirror is used, which is insensitive to the polarization state of the laser beam. The objective lens tightly focuses the beam onto the sample, which, following light-matter interaction, produces THG radiation, which is collected in the forward detection geometry by a condenser lens (achromatic-aplanatic, 1.4 NA, Carl Zeiss). A polarizing beam splitter cube (CCM1-PBS251, Thorlabs) analyzes the THG signal into two orthogonal components, which are filtered by suitable short-pass (FF01-680/SP, Semrock) and narrow bandpass (FF01-514/3, Semrock) filters, placed just in front of the detectors, to cut off residual laser light and any other unwanted signal. The two orthogonally placed

detectors, collecting the THG radiation, are based on photomultiplier tube modules (H9305-04, Hamamatsu). The diffraction-limited spatial resolution is ≈1.176 μm ($0.61\lambda_{exc}$ /NA, with $\lambda_{exc}$ = 1542 nm, NA = 0.8).

The galvanometric mirrors and the photomultiplier tubes are connected to a connector block (BNC-2110, National Instruments Austin), which is interfaced to a PC through a DAQ (PCI 6259, National Instruments). The coordination of the detector recordings with the galvanometric mirrors for the image formation, as well as the movement of the motors, are carried out using LabView (National Instruments).

Each image presented here consists of 500×500 pixels. For the data analysis, the open-source Python programming language [27], and the open-source ImageJ image analysis software [28] are used. We note that in all experimental polar plots presented in this work: i) each ROI of pixels is treated as one pixel with intensity equal to the mean intensity in the ROI, and ii) we have selected a sample region without SnS crystals, whose intensity has been considered as noise and has been subtracted from our measurements. Finally, regarding the adopted fitting procedure, the relative magnitudes of the $\chi^{(3)}$ tensor components are bounded in [0, 1].

### 5.3.2 Sample preparation and characterization

The LPE method is employed to isolate an ultrathin layer of SnS sheets [1-6]. The isolated ultrathin SnS sheets are characterized with UV-Vis spectroscopy, atomic force microscopy (AFM), Raman spectroscopy, and photoluminescence (PL) spectroscopy, and are identified to consist of monolayer and bilayer crystals. Details regarding the sample preparation and characterization can be found in the original publication.

## References

[1] G. M. Maragkakis, S. Psilodimitrakopoulos, L. Mouchliadis, A. S. Sarkar, A. Lemonis, G. Kioseoglou, E. Stratakis, *Adv. Optical Mater.* **2022**, 10, 2270038.

[2] J. R. Brent, D. J. Lewis, T. Lorenz, E. A. Lewis, N. Savjani, S. J. Haigh, G. Seifert, B. Derby, P. O'Brien, *J. Am. Chem. Soc.* **2015**, 137, 12689.

[3] A. S. Sarkar, E. Stratakis, *J. Colloid Interface Sci.* **2021**, 594, 334.

[4] A. S. Sarkar, A. Mushtaq, D. Kushavah, S. K. Pal, *npj 2D Mater. Appl.* **2020**, 4, 1.

[5] A. S. Sarkar, I. Konidakis, E. Gagaoudakis, G. M. Maragkakis, S. Psilodimitrakopoulos, D. Katerinopoulou, L. Sygellou, G. Deligeorgis, V. Binas, I. M. Oikonomou, P. Komninou, G. Kiriakidis, G. Kioseoglou, E. Stratakis, *Adv. Sci.* **2022**, 10, 2201842.

[6] A. S. Sarkar, A. Kumari, Anchala, N. Nakka, R. Ray, E. Stratakis, S. K. Pal, *Appl. Phys. Lett.* **2021**, 119, 241902.

[7] S. Psilodimitrakopoulos, L. Mouchliadis, I. Paradisanos, A. Lemonis, G. Kioseoglou, E. Stratakis, *Light: Sci. Appl.* **2018**, 7, 18005.

[8] G. M. Maragkakis, S. Psilodimitrakopoulos, L. Mouchliadis, I. Paradisanos, A. Lemonis, G. Kioseoglou, E. Stratakis, *Opto-Electron. Adv.* **2019**, 2, 190026.

[9] S. Psilodimitrakopoulos, L. Mouchliadis, I. Paradisanos, G. Kourmoulakis, A. Lemonis, G. Kioseoglou, E. Stratakis, *Sci. Rep.* **2019**, 9, 14285.

[10] S. Psilodimitrakopoulos, A. Orekhov, L. Mouchliadis, D. Jannis, G. M. Maragkakis, G. Kourmoulakis, N. Gauquelin, G. Kioseoglou, J. Verbeeck, E. Stratakis, *npj 2D Mater. Appl.* **2021**, 5, 77.

[11] S. Psilodimitrakopoulos, L. Mouchliadis, G. M. Maragkakis, G. Kourmoulakis, A. Lemonis, G. Kioseoglou, E. Stratakis, *2D Mater.* **2021**, 8, 015015.

[12] L. Mouchliadis, S. Psilodimitrakopoulos, G. M. Maragkakis, I. Demeridou, G. Kourmoulakis, A. Lemonis, G. Kioseoglou, E. Stratakis, *npj 2D Mater. Appl.* **2021**, 5, 6.

[13] P. Réfrégier, M. Roche, J. Duboisset, S. Brasselet, *Opt. Lett.* **2012**, 37, 4173-4175.

[14] A. Autere, C. R. Ryder, A. Säynätjoki, L. Karvonen, B. Amirsolaimani, R. A. Norwood, N. Peyghambarian, K. Kieu, H. Lipsanen, M. C. Hersam, Z. Sun, *J. Phys. Chem. Lett.* **2017**, 8, 1343.

[15] S.-W. Chu, S.-Y. Chen, G.-W. Chern, T.-H. Tsai, Y.-C. Chen, B.-L. Lin, C.-K. Sun, *Biophysical Journal* **2004**, 86, 6, 3914-3922.

[16] A. Jain, S. P. Ong, G. Hautier, W. Chen, W. D. Richards, S. Dacek, S. Cholia, D. Gunter, D. Skinner, G. Ceder, K. A. Persson, *APL Materials* **2013**, 1, 011002.

[17] E. Hecht, *Optics*, Pearson Education Limited, Harlow, United Kingdom **2017**.

[18] R. W. Boyd, *Nonlinear Optics*, Academic Press, Elsevier **2020**.

[19] A. Dasgupta, J. Gao, X. Yang, *Laser Photonics Rev.* **2020**, 14, 1900416.

[20] X. L. Yang, S. W. Xie, *Appl. Opt.* **1995**, 34, 6130.

[21] R. P. N. Tripathi, X. Yang, J. Gao, *Opt. Express* **2022**, 30, 22661-22670.

[22] M. J. L. F. Rodrigues, C. J. S. de Matos, Y. W. Ho, H. Peixoto, R. E. P. de Oliveira, H.-Y. Wu, A. H. C. Neto, J. Viana-Gomes, *Adv. Mater.* **2016**, 28, 10693-10700.

[23] N. Youngblood, R. Peng, A. Nemilentsau, T. Low, M. Li, *ACS Photonics* **2017**, 4, 1, 8–14.

[24] H. Sar, J. Gao, X. Yang, *Sci Rep* **2021**, 11, 6372.

[25] H. Sar, J. Gao, X. Yang, *Sci Rep* **2020**, 10, 14282.

[26] Q. Cui, R. A. Muniz, J. E. Sipe, H. Zhao, *Phys. Rev. B* **2017**, 95, 165406.

[27] G. van Rossum, *Python tutorial*, Technical Report CS-R9526, Centrum voor Wiskunde en Informatica (CWI), Amsterdam, May **1995**.

[28] C. A. Schneider, W. S. Rasband, K. W. Eliceiri, *Nat. Methods* **2012**, 9, 671.

# Chapter 6 - Conclusions

## 6.1 Imaging the crystal orientation of 2D TMDs using P-SHG

In conclusion, we have demonstrated an all-optical, fast and minimally-invasive method to accurately image the armchair orientation in atomically thin 2D crystals, via probing of their P-SHG properties. It is shown that different crystal orientations provide different P-SHG modulations and subsequent contrast in the images obtained. The presented method comprises the measurement of the P-SHG signal anisotropy, produced by a stationary raster-scanned 2D crystal, as a response to the rotating linear polarization of the fs excitation field. By fitting, pixel-by-pixel, this polarization-dependent modulation into a generalized nonlinear model, we are able to extract and map, with high resolution, the distribution of armchair crystal orientations over large areas of the 2D lattice. This approach allows us to obtain valuable information of crystal homogeneity, and therefore can provide a unique tool for the evaluation of crystal quality, for emerging 2D material applications. Given that such capabilities cannot be attained via traditional, intensity-only SHG imaging, we envisage that this work can establish P-SHG as a modern, state-of-the-art 2D material characterization tool.

## 6.2 Real-time spatially resolved determination of twist angle in TMD heterobilayers

In conclusion, we have presented an all-optical and minimally invasive methodology, based on SHG microscopy, for the spatially resolved calculation of twist angles in 2D TMD heterobilayers. In particular, the detected SHG intensity images produced by a $WS_2/MoS_2$ heterostructure are instantaneously used as input to a theoretical model that accounts for the SHG interference from the two different constituent TMD monolayers. The novelty of our method lies in performing measurements directly in the overlapping region, where we can reliably determine a twist angle. In addition, by using simultaneous measurements of two orthogonal SHG polarization components, as well as laser raster-scanning, the twist angle is mapped in real time and large crystal areas, enabling the detection of possible spatial variations in its distribution. We envisage our technique as a

powerful tool for the characterization of 2D TMD heterostructures and the engineering of their physical properties for emerging applications.

## 6.3 Nonlinear optical imaging of in-plane anisotropy in 2D SnS

In summary, taking advantage of the orthorhombic crystal structure of 2D SnS crystals that induces SHG conversion, we have optically mapped the in-plane optical anisotropy of 2D SnS flakes with high resolution. By performing P-SHG imaging microscopy, we found that the P-SHG polar plot changes shapes among different flakes. This finding reflects the effect of the in-plane anisotropy of the orthorhombic MXs on their nonlinear optical properties. This is demonstrated for different 2D SnS flakes belonging to the same field of view. Our approach provides new means of contrast that discriminates 2D SnS flakes in the same image based on their in-plane anisotropy. By fitting the experimental data with a nonlinear optics model, that accounts for the material crystal structure, we were able to calculate and map with high resolution the AC/ZZ crystallographic orientation of each flake, and to estimate two second-order nonlinear optical susceptibility tensor element ratios for every sample point. This methodology can be used to spatially determine in large crystal areas the optical in-plane anisotropy in different orthorhombic MXs crystals. Our results provide a novel, all-optical probe of the in-plane anisotropic properties of orthorhombic MXs based on nonlinear optics, that is useful for emerging fundamental studies and optoelectronic applications of these materials.

## 6.4 Anisotropic THG in 2D tin sulfide

In conclusion, we have presented an all-optical, minimally invasive and rapid methodology, based on P-THG nonlinear optical imaging, to characterize the anisotropic properties of ultrathin SnS crystals, produced via LPE. We observe a variation of THG emission intensities for different polarization angles of the excitation field, demonstrating the in-plane anisotropic nature of the THG process. By using a polarizing beam splitter and two orthogonally placed detectors, we simultaneously record the intensity of the two orthogonal components of the THG field, while rotating the direction of the linear polarization of the excitation beam, enabling P-THG imaging. We then simultaneously fit the intensities of the two orthogonal components with a nonlinear optics model, which accounts for the orthorhombic crystal structure of 2D SnS. This approach enables the calculation of the relative magnitudes of the $\chi^{(3)}$ tensor components, with increased precision and decreased ambiguity. Our results indicate that the on-axis nonlinear susceptibility tensor elements,

$\chi_{11}$ and $\chi_{22}$, are considerably larger than the off-axis elements, $\chi_{18}$ and $\chi_{29}$. We have also introduced and calculated a THG AR, which compares the total THG intensity upon excitation parallel to the AC direction compared to the case where it is parallel to the ZZ. Our results provide quantitative information on the effect of the in-plane anisotropy of ultrathin SnS on its nonlinear optical properties. Besides this, in case of 2D MXs crystals of larger size, this technique can additionally offer large-area information on the presence of grain boundaries and defects [1-3]. We envisage that this work can introduce a useful method for studying the THG response of in-plane anisotropic 2D materials, towards fundamental studies, as well as the realization of polarization-sensitive nonlinear optical devices.

## References

[1] L. Karvonen, A. Säynätjoki, M. J Huttunen, A. Autere, B. Amirsolaimani, R. A. Norwood, N. Peyghambarian, H. Lipsanen, G. Eda, K. Kieu, Z. Sun, *Nat. Commun.* **2017**, 8, 15714.

[2] S. Psilodimitrakopoulos, L. Mouchliadis, I. Paradisanos, A. Lemonis, G. Kioseoglou, E. Stratakis, *Light: Sci. Appl.* **2018**, 7, 18005.

[3] G. M. Maragkakis, S. Psilodimitrakopoulos, L. Mouchliadis, I. Paradisanos, A. Lemonis, G. Kioseoglou, E. Stratakis, *Opto-Electron. Adv.* **2019**, 2, 190026.